Technische Universität Ilmenau
Fakultät für Mathematik und Naturwissenschaften
Institut für Physik
Fachgebiet Technische Physik II

Structure and Molecular Dynamics of Liquid Crystalline / Isotropic Block Copolymers

Dissertation zur Erlangung des akademischen Grades

Dr. rer. nat.

vorgelegt von
MSc Rosina Staneva
geboren am 20.04.1973 in Ruse / Bulgarien

Gutachter:

Prof. Dr. rer. nat. habil. Bernd Stühn (Betreuer)
Priv.-Doz. Dr. rer. nat. habil. Paul Denner
Prof. Dr. rer. nat. habil. Thomas Thurn-Albrecht

Eingereicht am: 20.06.2006
Verteidigt am: 13.10.2006

urn:nbn:de:gbv:ilm1-2006000135

Content

Abstract

Microphase separated block copolymers are an important part of modern nanotechnology. These block copolymers combine two polymers with different physical properties, which are separated by nanoscale domains.

This dissertation investigated the morphology, molecular dynamics and phase transitions of novel side-chain liquid crystalline / polystyrene (PSLC) block copolymers with well defined chemical structure, broad composition range and narrow molecular weight distributions.

The domain structure of the microphase separated block copolymers was determined by small angle X-ray scattering (SAXS). Four types of structures were found to occur: polystyrene (PS) cylinders in liquide crystalline (LC) matrix, alternating lamellae, LC cylinders in PS matrix and LC spheres in PS matrix. The domain dimensions vary between 9 and 26 nm and the lattice constants between 27 and 47 nm. The phase diagram remains stable in a temperature range of 25°C-170°C, i.e. the morphology of the samples does not change. However, it differs strongly from the phase diagram of isotropic / isotropic (I/I) block copolymers; due to the influence of the nematic LC phase it is strongly asymmetric.

The molecular dynamics, studied by dielectric spectroscopy (DS), detected four relaxation processes: two segmental (α- relaxation and δ-relaxation) and two local (β-relaxation and γ-relaxation) relaxations. They correspond to the segmental motion of the main chain together with the side chain (α), to the motion of the side-chain as a whole (δ), to the rotation of the biphenyl mesogen around its long axis (β) and to the motion of the alkyl spacer in the side-chain of the LC block (γ). While the α- and δ-relaxations show cooperative character, β-relaxation behaves as partially cooperative and γ-relaxation shows purely local behaviour. The PSLC with a LC phase, confined in domains exhibit an additional relaxation process at low frequencies, namely the Maxwell-Wagner (MW) polarization, which appears due to polarization at the interface between the LC and PS block

The spatial confinement of the LC block in 1D- (lamellae) and 2D- (cylindrical) domains has an influence on the dielectric parameters of the α-, δ-, β- and γ- relaxations, depending on the cooperativity length for each process. It was found that the relaxation time for δ- and α- relaxation processes decreases significantly in a restricted geometry. The decrease of relaxation time is more pronounced for the 2D confinement (cylindrical LC domains). The dependence of the relaxation time of the β- process on the constraint is similar to that of α- and δ- relaxations, although the variation is less pronounced. The relaxation time of the γ- relaxation is not influenced by the domain shape and dimensions.

The results in this dissertation contribute to a better understanding of the morphlogy and molecular dynamic of side-chain liquid crystal / isotropic (SCLC/I) block copolymers as well as of the molecular dynamics in a confined geometry. This work forms a basis for further development in polymer-LC design leading to the improvement of up to date existing theories for SCLC/I block copolymers as well as future technological applications.

Zusammenfassung

Mikrophasen separierte Blockcopolymere stellen einen wichtigen Bestandteil der modernen Nanotechnologie dar. Sie kombinieren zwei Polymere mit unterschiedlichen physikalischen Eigenschaften und zeigen eine Domänenbildung im Nanobereich.

In dieser Dissertation wurden Morphologie, Molekulardynamik und Phasenübergänge von neuartigen seitenketten-flüssigkristallinen / Polystyren (PSLC) Diblockcopolymeren mit gut definierter chemischer Struktur, breitem Zusammensetzungsbereich und einer engen Molekulargewichtsverteilung studiert.

Die Morphologie der mikrophasenseparierten Blockcopolymere wurde mittels Röntgenkleinwinkelstreuung (SAXS) untersucht. Es wurden vier Typen von Strukturen gefunden: Polystyren-(PS)-Zylinder in einer flüssigkristallinen (LC)-Matrix, alternierende Lamellen, LC-Zylinder in einer PS-Matrix und LC-Kugeln in einer PS-Matrix. Die Größenordnung der Domänen lag zwischen 9 und 26 nm, die der Gitterkonstanten zwischen 27 und 47 nm. Das Phasendiagramm verhielt sich in einem Temperaturbereich von 25 bis 170 °C stabil, d.h. die Morphologie der Proben änderte sich nicht. Dennoch unterschied es sich auf Grund des Einflusses der nematischen LC Phase sehr stark vom Phasendiagramm der isotrop/isotropen (I/I) Blockcopolymere. Im Gegensatz zum Phasendiagramm der I/I Blockcopolymere, wies das der untersuchten PSLC Proben eine starke Asymmetrie auf.

Die Molekulardynamik wurde mit dielektrischer Spektroskopie (DS) untersucht. Vier Relaxationsprozesse wurden dabei festgestellt – zwei segmentale (α-Relaxation und δ-Relaxation) und zwei lokale (β-Relaxation und γ-Relaxation). Die α-Relaxation bezieht sich auf die segmentale Bewegung der Hauptkette zusammen mit der Seitenkette. Die δ-Relaxation korrespondiert mit der Bewegung der Seitenkette als ganze. Die β-Relaxation der Rotation der Biphenyl Mesogene um ihre Längsachse. Die γ-Relaxation entspricht der Bewegung der Alkylspacer in der Seitenkette des LC Blocks. Während α und δ Relaxationen kooperativen Charakter aufweisen, verhält sich die β-Relaxation teilweise kooperativ und γ-Relaxation rein local. PSLC mit eine LC Phase, die eine eingeschränkte Geometrie aufweisen, zeigen einen zusätzlichen Relaxationsprozess bei niedrigen Frequenzen: die sogenannte Maxwell-Wagner (MW) Polarisation. Diese zeigt sich aufgrund der Polarisation am Interface zwischen dem LC und PS Block.

Die räumliche Einschränkung des LC Blocks in 1D (Lamellen) und 2D (Zylinder) Domänen hat unterschiedlichen Einfluss auf die dielektrischen Parameter der α, δ, β und γ –Relaxationen, abhängig von der Kooperationslänge für den jeweiligen Prozess. Es wurde festgestellt, dass die Relaxationszeit τ für δ- und α-Relaxationensprozesse in eingeschränkter Geometrie signifikant abnimmt. Die Abnahme in τ ist bei 2D Begrenzung (zylindrische LC Domänen) stärker ausgeprägt. Die Abhängigkeit der Ralaxationszeit des β-Prozesses von der Einschränkung ist ähnlich der der α- und δ-Relaxationen, wenn auch weniger stark ausgeprägt. Die Relaxationszeit der γ-Relaxation wird nicht durch die Domänenform oder Dimension beeinflusst.

Die Ergebnisse dieser Dissertation tragen zu einem besseren Verständnis der Morphologie und Molekulardynamik von seitenketten-flüssigkristallinen / isotropen (SCLC/I) Blockcopolymeren bei. Sie geben auch Aufschluss über die Molekulardynamik in eingeschränkter Geometrie. Die hier präsentierten Ergebnisse bilden damit eine Basis für einerseits weiterführende Entwicklungen im Polymer-LC Design für technische Anwendungen und andererseits für Verbesserungen der aktuell existierenden Theorien über SCLC/I Blockcopolymere.

1. Introduction

In recent years, the field of nanotechnology has extended into the area of soft matter [1-8]. In this extension, known as “soft nanotechnology” [1], one of the most discussed topics is the self-assembly of block copolymers [2, 3]. Block copolymers consist of two or more chemically distinct polymer blocks coupled together by chemical bonds. Figure 1.1 shows a sketch of a side-chain liquid crystal / isotropic (SCLC/I) block copolymer, which will be considered in the present work.

The self-assembly of block copolymers is a result of the microphase separation of different polymer blocks in distinct domains. The driving force of this separation process is the enhanced repulsion existing between two different polymer species. This repulsion occurs with increasing the number of monomers (or stiff segments) per chain or decreasing the temperature.

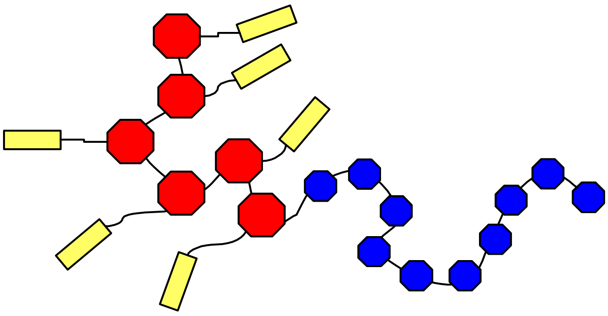

Figure 1.1. Schematic picture of side-chain liquid crystal / isotropic (SCLC/I) diblock copolymer.

By choosing the proper polymers, volume fractions and molecular weights, one can govern the self-assembly of the block copolymer system by tuning the size, shape and periodicity of domains on the nanoscale. The combination of two or more different species separated in regularly ordered domains leads to novel materials with improved physical properties, such as a combination of anisotropic optical, electrical or mechanical properties with good thermal and physical resistance as well as durability. Such materials show potential for a broad spectrum of practical applications in nanotechnology where various precisely ordered structures are desired [1, 4-7].

Block copolymers can be divided to two groups: an isotropic / isotropic (I/I) group and one containing at least one block with internal structure (structure-within-structure morphologies [8]).

The morphology of the I/I block copolymers has been extensively investigated by various groups both, theoretically and experimentally [9-31]. In such studies, the experimentally obtained phase diagrams correspond very well to those predicted theoretically.

Studies on block copolymer materials possessing structure-within-structure morphologies are still in their infancy. A key feature of such polymers is that one or more blocks exhibit liquid crystalline (LC) (Figure 1.1) or crystalline order, i.e. the domain periodicity is combined with the periodicity within the domain itself. Presently, the morphology of liquid crystalline / isotropic (LC/I) block copolymers is not well understood [32, 33]. For instance, it is not known how the domain periodicity and the LC order within the domain influence each other, or if there exists a connection between the LC order and the domain shape. Answers to these and other questions can only be obtained by spending a considerable amount of effort on both theoretical and experimental levels.

This thesis is focussed on a special type of block copolymers that possess structure within structure type of morphology. These block copolymers are side-chain liquid crystal / isotropic (SCLC/I) block copolymers. Liquid crystal/isotropic (LC/I) block copolymers are interesting from a fundamental as well as technological viewpoint due to the combination of thermotropic LC behaviour and mesomorphic domain morphologies. By combination of a rigid, glassy block and a LC block with a lower glass transition temperature [34] one can synthesize materials with unique mechano-optic and electro-optic properties [35]. Thus, such materials can find applications in the field of non-linear optics. There are several experimental reports in literature about the morphology of (LC/I) block copolymers [36-42]. The first theoretically calculated phase diagrams SCLC/I block copolymers have also been reported recently [35]. The theory for example, describes well the experimental data obtained by several groups, but there are still some exceptions [35]. The theory predicts order-to-order transition from low-curvature microstructures to higher curvature microstructures at the isotropisation temperature of the LC block that has indeed been experimentally detected [41, 42]. However, it cannot clarify the reverse type of order-to-order transition observed by Hammond et al. [36]. This is due to the fact that the attained experimental phase diagrams depend on the type of the LC block, which is why it is hard to find a unique theory, describing all of the transitions.

In addition to the influence of the composition and temperature, which govern the phase diagram of the I/I block copolymers, the architectural, conformational and configuration asymmetry also influence the phase diagram. Thus, a lot of new experiments have to be done in order to extract a common picture for all these parameters.

One of the most important questions in the field of soft nanoscience, that has recently attracted much attention, is how the molecular dynamics change in restricted geometries. In reply to this question, one can estimate the length scale of the relaxation processes. One of the most technologically relevant relaxation processes is the glass transition or the so called α- relaxation. The α- relaxation in polymers is related to the main chain relaxation. If the system size is comparable to the characteristic length scale of the glass transition, deviations from bulk (unconfined) properties are expected to appear. Several studies have demonstrated that the α-process speeds up and the relaxation time distribution broadens for a confined state [43-51, 65]. However, there are systems which show an opposite behaviour [52-55]. These contradictory results are not fully explained to date. In order to understand the glass transition in restricted geometry, extensive amount of experimental work needs to be performed on various model systems. Most studies in this area are carried out on materials confined to nanopores [43-49, 52-54, 56, 57] and ultrathin polymer films [50, 51, 55, 58-65]. Block copolymers are also an attractive model system for studying the molecular dynamics of polymers in restricted geometries. This is because the type and the dimensions of block copolymer domains can be controlled during synthesis and domain sizes down to several nanometers can be achieved. The usual type of domains – lamellae, cylinders and spheres, can be regarded as one- (1D), two- (2D) and three-dimensional (3D) confinements, respectively. Decreasing the domain size, one can follow the variation of relaxation parameters for local and segmental modes. This idea has been exploited in only few studies – for I/I block copolymers [66-68] and for in LC/I block copolymers [69-71].

The aim of this thesis is to study the morphology and molecular dynamics of a series of polystyrene- block- side-chain liquid crystal (PSLC) block copolymers. The samples possess well-defined structure and narrow molecular weight distributions. Block volume fractions were varied systematically. Polystyrene was chosen as an isotropic block due to its easy synthesis and high glass transition temperature [34]. The side-chain LC block was synthesized with cyanobiphenyl mesogens because of their strong polarizability and the large electrical field susceptibility [72]. Such a combination between the two blocks makes the present polymers a good model system for dielectric studies in a confined geometry.

The morphology of PSLC block copolymer system was investigated by means of small angle X-ray scattering (SAXS). In addition, the LC order was examined using polarized optical microscopy (POM), differential scanning calorimetry (DSC) wide angle X-ray diffraction (WAXD) and dielectric spectroscopy (DS). The molecular dynamics of LC blocks in matrix (unconfined geometry) and of confined domains in 1D, 2D and 3D was probed by dielectric spectroscopy (DS).

This thesis uses a special model system and combines structural and dynamic characterisation methods in order to study the above mentioned questions. The results complement the studies on the structure of LC/I block copolymers and could help in developing more accurate theoretical models. This is crucial for future application of SCLC/I block copolymers in the field of soft nanotechnology.

2. Liquid crystals

The *mesomorphic state* is a state of matter in which the molecular order is intermediate between the perfect three-dimensional long-range crystal order and the complete absence of long-range order found in isotropic liquids [73]. It occurs when the melting (freezing) of the rotational and translational degrees of freedom of the molecules does not happen simultaneously. The *mesophase* is a thermodynamical phase within the mesomorphic state with specific order. One material can undergo several mesophases with the variation of temperature, pressure, or concentration.

The *mesophase* can be plastic crystalline and liquid crystalline.

- It is *plastic crystalline* (called also rotator) when the rotational degree of freedom of the molecules is melted, but their centres of mass remain frozen. Materials, which show plastic crystalline behaviour, are referred to as *plastic crystals*.
- It is *liquid crystalline* when the translational degrees of freedom are melted but the rotational ones remain frozen. Materials in liquid crystalline phase are, thereby, said to be *liquid crystals* (LC) [74]. The substances in a liquid-crystalline state have a long-range orientational order and either a partial or complete positional disorder. In the classical sense, the liquid crystalline state is characteristic for materials made up of strongly asymmetric molecules that have a rod-like or disk-like shape.

The liquid-crystalline mesophase possess any of the following qualities:

- *Thermotropic*: when the liquid-crystalline mesophase is formed by heating a solid or cooling an isotropic liquid, or by heating or cooling a thermodynamically stable mesophase
- *Barotropic*: when the liquid-crystalline mesophase it is formed due to pressure variations in the solid, liquid or thermodynamically stable mesophase
- *Lyotropic*: when the liquid-crystalline mesophase is formed by dissolving an amphiphilic mesogen in a suitable solvent under appropriate conditions of concentration, temperature and pressure

In this work, the thermotropic liquid crystalline systems of rod-like shaped molecules are examined.

When a system of rod-like shaped molecules is in the liquid crystalline state, the rods are oriented towards one preferred direction $\vec{n}$ called director. The degree of alignment is defined by the *order parameter* or *anisotropy factor (S)*:

$$S = \frac{1}{2}\left\langle 3\cos^2\beta - 1 \right\rangle \tag{2.1}$$

where β is the angle between the molecular long axis and the director and the brackets denote an ensemble average. The order parameter varies from 0 to 1. It is equal to zero for completely isotropic systems and equal to one for perfectly aligned samples. Values of S of about 0.3-0.4 correspond to the average inclination of the long molecular axes from $\vec{n}$ by approximately 20°. When the average inclination of the long molecular axes from $\vec{n}$ is close to 90°, i.e. the majority of the rods have β~90°, equation 2.1 gives negative values. However, the director $\vec{n}$ is not a random chosen axis, but is defined as the preferred direction of orientation of the rods. Therefore, it is not possible that the majority of the rods are oriented perpendicular to $\vec{n}$. Hence, for the present definition of β, the order parameter S can have only positive values.

A compound (a molecule or a part of molecule), that under suitable conditions of temperature, pressure, and concentration can exist as a mesophase (or in particular as an LC phase) is called a *mesogen.* Thermotropic LC form several characteristic phases depending on the positional order of the mesogens.

In the *nematic* liquid crystalline phase the mesogens have a long range orientational order, but do not possess a long range translational order. The nematic phase can be considered as an anisotropic liquid [2]. The nematic phase is denoted by N (Figure 2.1).

The *chiral nematic* liquid crystalline phase occurs when the nematic phase is formed by chiral molecules. This phase is denoted by N* (Figure 2.1). A characteristic feature of this phase is that the director $\vec{n}$ twists around to form a helix. The pitch of the helix is in the range of ~100 nm to near infinity [2].

In the *smectic* phases the mesogens are ordered in layers (Figure 2.2). There are several types of smectic phases including the following:

1) *Smectic A* (SmA) phase: In which the director $\vec{n}$ is normal to the layers and the mesogens have liquid-like order within the layer
2) *Smectic C* (SmC) phase: In which the director is tilted with respect to the layers and there is a liquid-like order of the mesogens within the layer.
3) *Smectic B* (SmB), *smectic I* (SmI) and *smectic F* (SmF) phases: These phases possess six-fold bond-orientational order. This means, that the lattice orientation is retained in the layers but the translational order is lost within a few intermolecular distances. The director of the SmB phase is perpendicular to the

layer. The molecules in the SmI phase are tilted towards the nearest neighbour where in the SmF phases they are tilted towards an edge of the hexagonal net.

The temperature at which the transition between the mesophase with the highest temperature range and the isotropic phase occurs is denoted as *isotropization temperature* T_{i}. In the next chapters T_{i}. will be used to denote mainly the nematic-to-isotropic transition temperature.

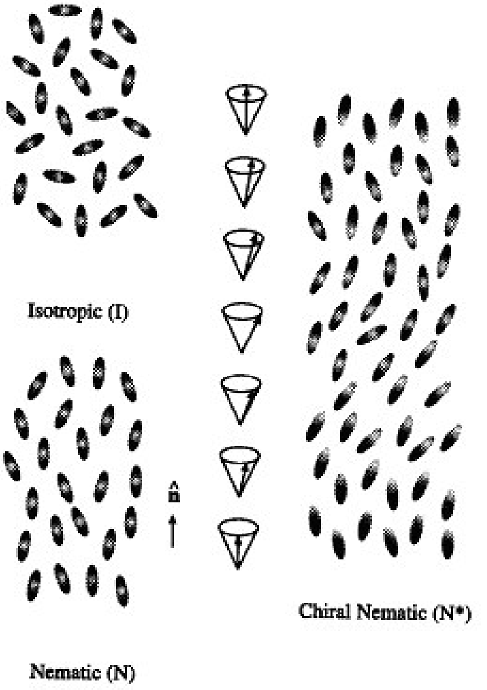

Figure 2.1. Schematic draw of isotropic (I), nematic (N) and chiral nematic phases (N*). Here $\vec{n}$ is the director. This Figure was adopted from Hamley [2].

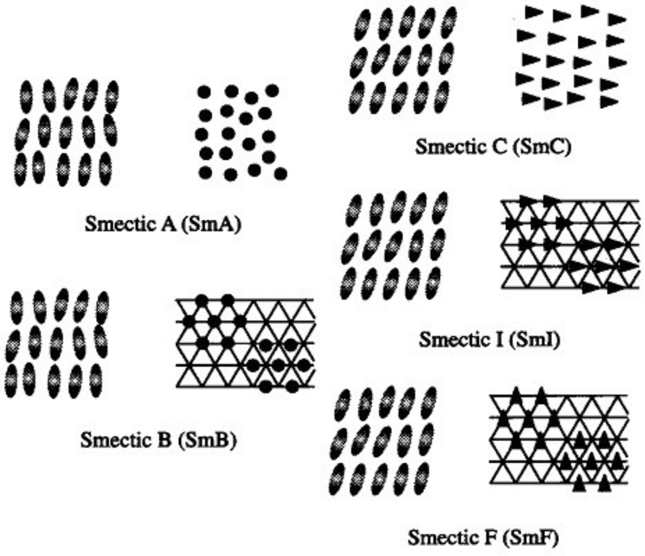

Figure 2.2. Schematic picture of the smectic (Sm) phases. On the left side the layer stacking is shown, on the right side the in-plane ordering is shown. This Figure was adopted from Hamley [2].

3. Block copolymers

3.1. Microphase separation in diblock copolymers

The aim of this chapter is to describe briefly the main principles of microphase separation and to answer questions such as why do the two distinct blocks in the block copolymer tend to separate and what are the driving forces, and so forth. A more comprehensive review on this topic is given in the book of Hamley [3].

The thermodynamics of diblock copolymer melts is governed by two competing factors: entropy, which tries to mix the two blocks homogeneously and enthalpy, which tries to demix them [3]. At high temperatures, in most cases the entropic factor is dominant and the chains are mixed homogeneously. (The investigated diblock copolymers in this thesis are in the strong segregation regime; in other words, they do not mix within the investigated temperature range up to 150-170°C. Higher temperatures were not applied because of the degradation of the polymer). An exception occurs for some polymers which do not mix, because the temperature of mixing is higher than the temperature of polymer degradation). With decreasing the temperature, the entropy decreases and the chain configuration becomes more constrained. In this way, the enthalpic process of demixing is favoured, i.e. the blocks tend to segregate. This process is defined as microphase separation due to the fact that the segregation of the blocks occurs at nanolength-scales. The length-scale for the phase separation is between 1 and 100 nm depending on the radius of gyration of the block [3]. Phase separation on a macroscopical level, defined as macrophase separation (such as in mixtures of two homopolymers), is prevented by the chemical bond existing between blocks. The transition from a homogeneous disordered phase to ordered microphase separated domains is referred to as order-to-disorder transition (ODT). The microphase separated domains may be ordered in a periodic structure known as a macrolattice.

The extent of segregation within the block copolymer can be expressed using the parameter χN. Here N is the degree of polymerisation of the block copolymer i.e. the number of monomers (the smallest repeat unit) in the polymer chain and χ the Flory-Huggins interaction parameter, which contains significant enthalpic contribution and is determined by the incompatibility of the monomers [3]. The increase of N favours microphase separation, because the repulsion between the blocks is proportional to N.

Moreover, the entropy of the polymer chain with degree of polymerisation N is smaller than the entropy of the N separate monomers (in the polymer chain the monomer units are connected with chemical bonds and can not move independently). The Flory-Huggins interaction parameter χ can be defined as

$$\chi \equiv \frac{1}{kT}(\varepsilon_{AB} - \frac{1}{2}(\varepsilon_{AA} + \varepsilon_{BB})), \tag{3.1}$$

where ε_{AA}, ε_{BB} and ε_{AB} are the energies of interaction between A-A, B-B and A-B monomer pairs. χ is dimensionless and is a measure of the change in the local free energy per reference unit. For most block copolymers, χ depends inversely on the temperature as defined in $\chi = C_1 + \frac{C_2}{T}$, where C_1 and C_2 are constants specific to each polymer [3].

Three regimes of phase separation, dependant on the extent of the block segregation are defined as: weak ($\chi N \approx 10$), intermediate ($\chi N \approx 10 - 100$), and strong segregation ($\chi N \geq 100$) regimes [3].

The phase diagram for diblock copolymers in the weak segregation regime was first computed within the *Landau mean field theory* by Leibler [9]. In order to simplify the calculations of the partition function, the *mean field theory* regards a system as consisting of non-interacting polymer chains in an *effective external field,* instead of an ensemble of interacting polymer chains. Leibler studied the density correlation functions of the monomer A in disordered phase using a generalization of the *random-phase approximation* (RPA) method of de Gennes [75, 76]. The RPA method uses the assumption that in the melt the polymer chains are nearly ideal on the length-scale of one coil. When the monomers do not interact with each other, the monomer density correlation functions should be equal to those of the ideal (Gaussian) independent copolymer chains. In RPA, one calculates the response of the system to the external potentials U_i as if the response function were those of the ideal chains; however the potentials acting on monomers U_i^{eff} (different from the external potentials U_i) were corrected to take the monomer interactions into account. Leibler assumes in his model that all block copolymer chains have the same degree of polymerization N and the same composition $\phi_N = N_A / N$ (N_A, $N_B >> 1$ are the numbers of monomers of type A and B, respectively; $N = N_A + N_B$); i.e., the polydispersity of the chains is neglected. Other assumptions include that both blocks have the same segment length a and the system has zero compressibility. As a result, at any point of the copolymer melt

$$\rho_A(\vec{r}) + \rho_B(\vec{r}) = 1 \qquad (3.2)$$

where $\rho_A(\vec{r})$ and $\rho_B(\vec{r})$ are the reduced number densities defined as the ratios of the local densities of the monomers A and B at the point $\vec{r}$ to the overall monomer densities averaged over the sample. The species A and B tend to realize an equilibrium density profile $\rho_A(\vec{r})$ and $\rho_B(\vec{r})$, which minimizes the free energy *F* of the system. The energy of interaction of different chemical species (per monomer) may be written as

$$E_{AB} \equiv kT \chi \rho_A \rho_B \qquad (3.3)$$

If the Flory-Huggins parameter χ is positive (which corresponds to repulsion between different type of monomers), then there is a tendency of decreasing the number of contacts between monomers A and B in order to lower the contribution of the interaction energy to the free energy. The decrease in the number of contacts A-B leads to a decrease of the entropy of the system and consequently to an increase of the free energy. Hence, $\rho_A(\vec{r})$ and $\rho_B(\vec{r})$ profiles are a result of the "competition" between these two opposing trends. If χ = 0 or is finite but sufficiently small, the entropy effects are dominant, and they favour mixing; the system exhibits an isotropic phase with sequences A and B of the chains interpenetrating each other so that at all points

$$\langle \rho_A(\vec{r}) \rangle = \phi_N \quad \text{and} \quad \langle \rho_B(\vec{r}) \rangle = 1 - \phi_N \qquad (3.4)$$

($\langle \; \rangle$ denotes the thermal average). This phase is called the disordered phase. On the other hand, when the temperature decreases or *N* increases, so that χN is larger than a certain value $(\chi N)_t$, then the enthalpic term in the free energy dominates and the system exhibits a microphase separation, i.e. $\rho_A(\vec{r})$ and $\rho_B(\vec{r})$ are not uniform, there are domains (A rich) where $\langle \rho_B(\vec{r}) \rangle$ is smaller than 1-ϕ_N and others (B rich) where $\langle \rho_A(\vec{r}) \rangle$ is smaller than ϕ_N. Then at all points the product $\rho_A \rho_B$ is small and the enthalpic term is low.

Leibler introduces an order parameter field $\psi(\vec{r})$:

$$\psi(\vec{r}) = \langle (1 - \phi_N) \rho_A(\vec{r}) - \phi_N \rho_B(\vec{r}) \rangle \qquad (3.5)$$

or, using Eq. 3.2 and 3.4

$$\psi(\vec{r}) = \langle \rho_A(\vec{r}) - \phi_N \rangle \equiv \langle \delta \rho_A(\vec{r}) \rangle \qquad (3.6)$$

$\psi(\vec{r})$ describes the average deviation from the uniform distribution of the monomers A and B. In the disordered state (small χN), $\psi(\vec{r})$ (or the average value of $\delta \rho_A$) vanishes at all points whereas for the different ordered phases $\psi(\vec{r})$ it is described with periodic functions.

When χN approaches $(\chi N)_t$, the local value of $\delta\rho_A$ has larger fluctuations. The fluctuations may be characterized by the following density-density correlation function

$$\tilde{S}(\vec{r}-\vec{r}\,')=\frac{1}{kT}\left\langle \delta\rho_A(\vec{r})\,\delta\rho_A(\vec{r}\,')\right\rangle \tag{3.7}$$

The free energy density of the ordered state can be expanded in terms of the order parameter ψ as [3, 9]:

$$F_D[\psi(\vec{q})]=\frac{1}{2!}\int \tilde{S}^{-1}(\vec{q})\psi(\vec{q})\psi(-\vec{q})d\vec{q}+\frac{1}{3!}\iint \mu(\vec{q},\vec{q}\,',-\vec{q}-\vec{q}\,')\psi(\vec{q})\psi(\vec{q}\,')\psi(-\vec{q}-\vec{q}\,')d\vec{q}d\vec{q}\,'$$

$$+\ \frac{1}{4!}\iiint \lambda(\vec{q},\vec{q}\,',\vec{q}\,'',-\vec{q}-\vec{q}\,'-\vec{q}\,'')\psi(\vec{q})\psi(\vec{q}\,')\psi(\vec{q}\,'')\psi(-\vec{q}-\vec{q}\,'-\vec{q}\,'')d\vec{q}d\vec{q}\,'d\vec{q}\,''. \tag{3.8}$$

Here $\vec{q}$ is the scattering vector (see chapter 4.1), $\psi(\vec{q})$ is the Fourier transformation of $\psi(\vec{r})$ and $\tilde{S}(\vec{q})$ is the Fourier transformation of the above mentioned density-density correlation function $\tilde{S}(\vec{r}-\vec{r}\,')$ (Eq. 3.7). The cubic term μ is zero for a symmetric system and otherwise may be chosen to be positive. The quartic term λ, is positive in order to ensure stability. Using RPA, Leibler obtained the following expression for the intensity (the Fourier transformation of the density-density correlation function):

$$\tilde{S}(\vec{q})=W(\vec{q})/[\Sigma(\vec{q})-2\chi W(\vec{q})], \tag{3.9}$$

where Σ and W are the sum of all elements and the determinant of the matrix composed of the correlation functions of the ideal independent copolymer chains $\left\|S_{ij}\right\|$, respectively. The calculation of the matrix elements S_{ij} is straightforward within the RPA and the following expressions are obtained for the diblock copolymer:

$$\begin{aligned} S_{11}(\vec{q})&=Ng(\phi_N,x)\\ S_{22}(\vec{q})&=Ng(1-\phi_N,x)\\ S_{12}(\vec{q})=S_{21}(\vec{q})&=\frac{1}{2}N\left[g(1,x)-g(\phi_N,x)-g(1-\phi_N,x)\right]\end{aligned} \tag{3.10}$$

Here $g(\phi_N,x)$ is called a Debye function and defined as

$$g(\phi_N,x)=2\left[\phi_N x-\exp(-\phi_N x)-1\right]/x^2 \tag{3.11}$$

and

$$x=q^2Na^2/6=q^2R_g^2 \tag{3.12}$$

with R_g denoting the radius of gyration of a Gaussian chain.

The final expression for $\tilde{S}(\vec{q})$ can be written as:

$$\tilde{S}(\vec{q}) = \frac{N}{F(x) - 2\chi N}, \tag{3.13}$$

where

$$F(x) = \frac{g(1,x)}{g(\phi_N, x)\; g(1-\phi_N, x) - \frac{1}{4}\left[g(1,x) - g(\phi_N, x) - g(1-\phi_N, x)\right]^2}. \tag{3.14}$$

There is a critical value of χN $(\chi N)_s$, for which $\tilde{S}(\vec{q})$ diverges at $|\vec{q}| = q^*$; this is called a spinodal point. The value of q^* is of the order of the reciprocal radius of gyration of the copolymer molecule. It defines the stability limit of the disordered phase. The spinodal point of block copolymers is not equal to the $(\chi N)_t$ at which the ODT occurs, except for symmetric block copolymers in mean field theory. $(\chi N)_s$ is larger than $(\chi N)_t$. Leibler found that the transition to the microphase separated state is a process of first order (except in a small interval around the point $\phi_N = 1\text{-}\phi_N = 0.5$), similar to the solidification of a liquid. The phase diagram is calculated by comparing the free energy of the various ordered phases and of the ordered phases with respect to the disordered phase [9].

$\tilde{S}(\vec{q})$ can be studied by elastic scattering experiments such as SAXS, small angle neutron scattering (SANS), and light scattering (LS). It is proportional to the scattering intensity (see chapter 4.1.1). In this study the method of SAXS is used. A theoretical calculation of the scattering intensity $\tilde{S}(\vec{q})$ of a molten block copolymer with composition ϕ_N=0.25 is shown on Figure 3.1.

Figure 3.2 shows the SAXS profiles for a nearly symmetric diblock copolymer below and above the order-to-disorder transition [26]. The authors fit the data above the order-to-disorder transition with the RPA structure factor.

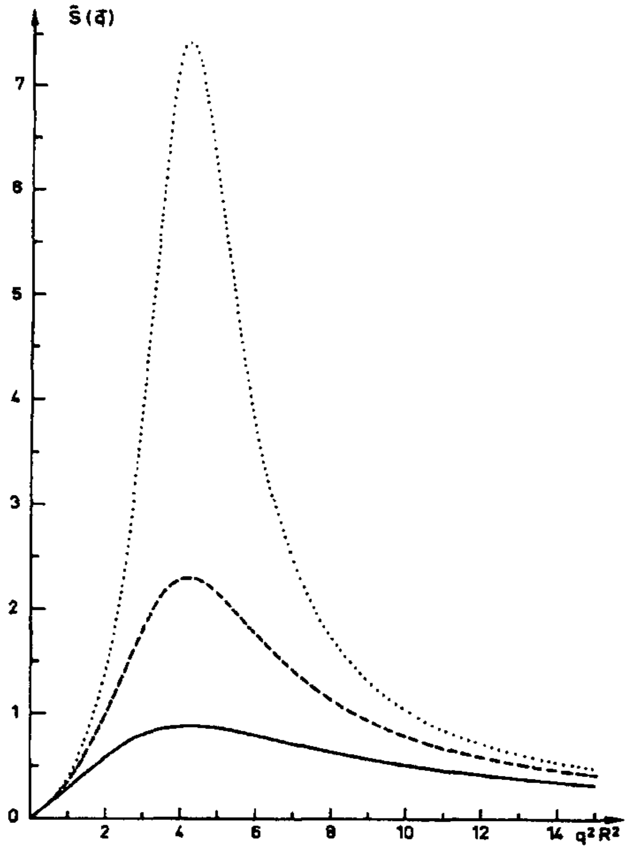

Figure 3.1. Theoretical calculations of the scattering intensity (in arbitrary units) of a molten diblock copolymer with composition ϕ_N=0.25 as a function of $x=(qR)^2$ ($q=4\pi[\sin(\theta/2)]/\lambda$) for three values of the interaction parameter: (····) χN=17.5; (---) χN=16.0; (-) χN=12.5. The interaction parameter for which $\tilde{S}(q^*)$ diverges (spinoidal point) is at χN=18.2. The MST is expected to occur for χN=17.6. The figure is adapted from [9].

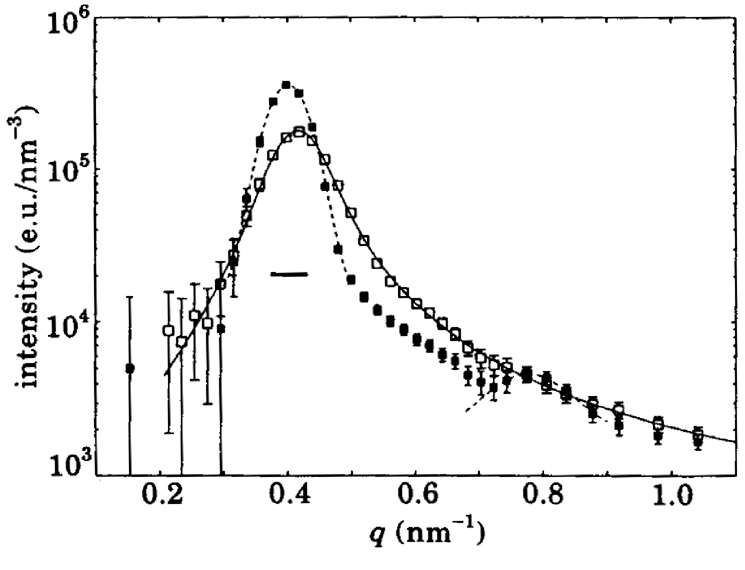

Figure 3.2. The SAXS profiles for nearly symmetric polystyrene/poly(cis-1,4)isoprene block copolymers above the order-to-disorder transition (T=100°C) (opened symbols) and in a microphase separated state (T=80°C) (filled symbols) [26].

The self consistent mean field theory (SCMFT) was used by Helfand and co-workers for calculating of phase diagram in the strong segregation regime. The external mean fields acting on a polymer chain are calculated self-consistently with the composition profile. The authors used the narrow interface approximation which assumes that the boundary between A and B domains is narrow compared to the domain width [10]. The phase boundaries were predicted to depend only on the copolymer composition ϕ [11]. This theory regards only the strong segregation regime, therefore the calculation of the phase boundaries is restricted to χN~100 and the ODT line can not be correctly calculated. The application of the Helfand's theory was limited due to the need for numerical analysis. The theory of the strong segregation regime was further developed by Semenov [12], who developed the *seminal analytical strong segregation limit theory*. The new point in Semenov's theory is that he analysed the interaction between isolated spherical microdomains using electrostatic analogy, i.e. every two domains interact according to Coulomb law.

Matsen and co-workers [14, 17] unified the weak and the strong segregation regime theories for block copolymer melts. They calculated a phase diagram based on the self-consistent mean field theory without using approximations such as the narrow interface approximation. At that time, progress in computational technique enabled the use of more Fourier terms for representing the segment profiles. The phase diagram presented on Figure 3.3 was obtained by comparing the free energies of the various phases.

The most common structures created by microphase separated diblock copolymers are: lamellae (L), hexagonally packed cylinders (H) and a body-centered cubic (BCC) array of spheres. In some systems, bicontinuous cubic structure ($Q_{Ia\bar{3}d}$) is observed, also known as the gyroid phase [18, 19, 22]. Some groups have experimentally demonstrated the existence of a hexagonally perforated lamellar (HPL) phase, sometimes called a catenoid lamellar. The thinner lamellar layer made of one of the blocks is perforated with cylinders made up of the second block arranged in hexagonal lattice [20-22, 36] (Figure 3.4).

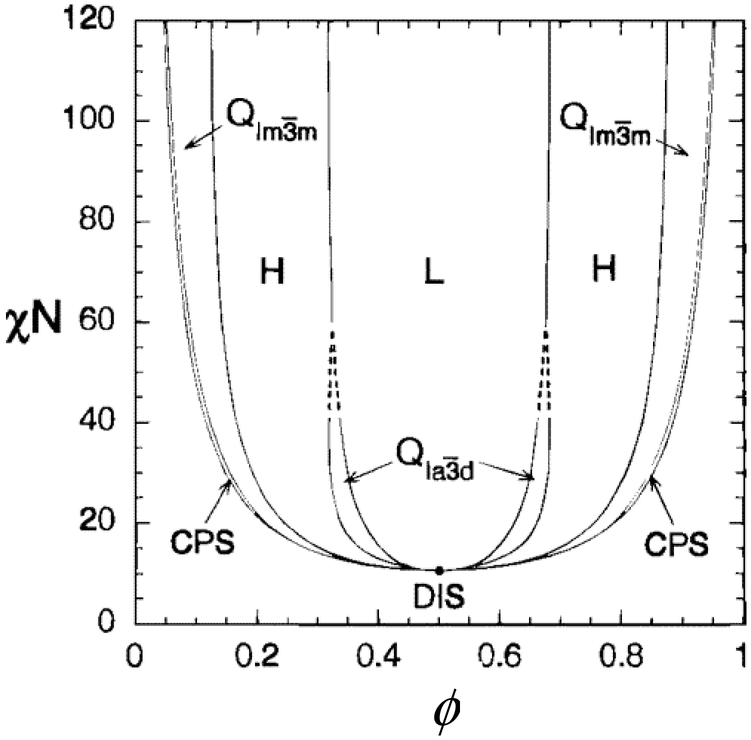

Figure 3.3. The mean field phase diagram for conformationally symmetric diblock melts. The phases are labelled L (lamellar), H (cylinders arranged in a hexagonal lattice), $Q_{Ia\bar{3}d}$ (bicontinuous $Ia\bar{3}d$ cubic), $Q_{\mathrm{Im}\bar{3}m}$ (BCC spheres), CPS (close- packed spheres), and DIS (disordered). Dashed lines denote extrapolated phase boundaries, and the dot denotes the mean field critical point. ϕ denotes the volume fraction of the one of the blocks, χ is the Flory-Huggins parameter and N is the degree of polymerisation. This figure is adapted from the work by Matsen and Bates [14].

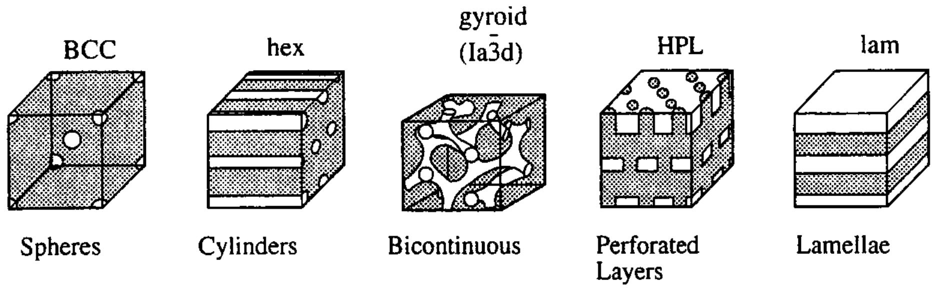

Figure 3.4. Block copolymer structures. This figure is adapted from Hamley [3].

3.2. Phase behaviour of Liquid Crystal / Isotropic block copolymers

Recently, M. Anthamatten and P. Hammond have developed a *free energy model of asymmetry in side-chain liquid crystalline diblock copolymers* [35]. They constructed several theoretical phase diagrams describing the domain structure of side-chain liquid crystal-amorphous diblock copolymers as a function of temperature and composition. The authors regarded two different cases of mesogen anchoring to the interface separating the two blocks, i.e. planar (parallel to the interface) or homeotropic (normal to the interface). The LC block was modelled using the Wang and Warner's theory for nematic comb-like polymers [77]. Wang and Warner assumed that mesogens interact through mean field potentials. The LC backbone was modelled as a worm-like chain. A worm-like chain is a hypothetical linear macromolecule with continuous curvature in which the direction of curvature at any point is random. The amorphous block was modelled as a freely rotated chain that can be described by Gaussian statistics.

The basic assumptions of the model are:

1) Each polymer molecule consists of two blocks connected through a covalent bond; one is an amorphous chain of N_A segments and the second one is the LC block with N_{LC} segments. The LC block consists of a backbone and side-chains attached to it at regular intervals.
2) The LC order is nematic.
3) The nematic side-chain has the same cross-sectional dimension as both backbones.
4) Both the amorphous and LC backbone are assumed to be long enough (N_A, $N_{LC} >> 1$) so that the homopolymer trajectories would form true random coils.
5) Both of the backbones are assumed to have identical segment lengths l.
6) The diblock copolymer melt is assumed to be incompressible with a constant and uniform density.
7) The amorphous block has the same elastic properties as the LC backbone.

According to the Wang and Warner theory, there are three possible nematic phases depending on the sign of the order parameter of the backbone S_{B} and the side-chains S_{M} (Figure 3.5). S_{M} is calculated using Eq. 2.1, however here the angle β_0 is not between the side-chain and the director $\vec{n}$, but between the side-chain and the z axis. Therefore, the values of β_0 are independent of $\vec{n}$ and the S_M value can be negative (when the side chains tend to orient to a position that is nearly perpendicular to the z direction). If $\vec{u}(s)$ is an unit vector, parallel to the tangent to the backbone at position s, then the backbone order parameter can be calculated analogical to the Eq. 2.1:

$$S_B = \left\langle \frac{1}{2L_{LC}} \int_0^{L_{LC}} (3[\hat{u}_z(s)]^2 - 1)ds \right\rangle,$$

where L_{LC} is the length of the LC backbone, s is a coordinate along the backbone and $\hat{u}_z(s)$ is the component of $\vec{u}(s)$, which is parallel to the z axis. In this way the direction of $\hat{u}_z(s)$ is regarded to be relative to the z axis, and not to the director $\vec{n}$ and the backbone order parameter S_B can be positive or negative.

One should distinguish between the order parameter of mesogens S, regarded relative to the internal, connected with the mesogens axis (the director $\vec{n}$) and the order parameters S_B and S_M, which are regarded relative to a external axis, independent on the mesogen orientation. In the first case the values of β_0 are restricted and the order parameter can vary in the interval of 0 to 1. In the second case the values of β_0 are arbitrary, so that S_B and S_M can vary in the interval from -0.5 to 1.

The authors use five parameters to describe the various types of interactions in the block copolymer system:

1) v_a – the coupling parameter, which accounts for the degree of parallel ordering of the mesogenic side-chains
2) v_b – the coupling parameter, which accounts for the degree of parallel ordering of the LC backbone units
3) v_c – the coupling between the mesogenic side chains and the LC backbone
4) v_f – the tendency of the side-chains to orient perpendicular to the backbone
5) ε_{BE} – the bending energy coefficient of the LC backbone

These interactions are weighted in a mean-field sense according to the volume fractions of the LC backbone and the nematic side-chains.

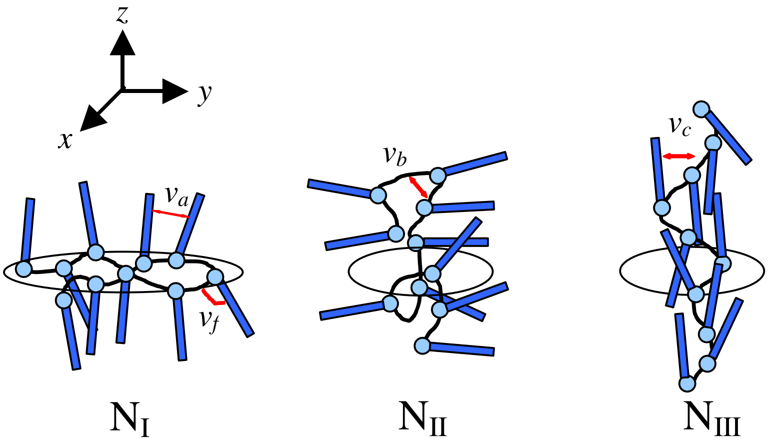

Figure 3.5. Drawing of three possible nematic phases from the Wang-Warner model. The phases are classified according to the direction of the side-chain and backbone ordering: N_I (S_M>0, S_B<0), N_{II} (S_M<0, S_B>0), and N_{III} (S_M>0, S_B>0). v_a, v_b, v_c and v_f represent coupling parameters from the Wang-Warner theory. The direction of uniaxial symmetry is z, i.e. the chain dimensions are identical in any direction orthogonal to z. Disks are drawn orthogonal towards z to aid the eye. The picture is redrawn from ref. [35].

In the strong segregation regime the total free energy can be described as:

$$F_T = F_{LC} + F_A + F_\gamma + F_e + F_{mix} \tag{3.15}$$

where

F_{LC} includes interactions and entropic components associated with the LC block

F_A is the stretching free energy of the amorphous block

F_γ accounts for the interfacial surface free energies

F_e arises from elastic distortions due to the curvature in the LC field

F_{mix} represents the Flory – Huggins mixing and is included only if the melt is homogeneously phase-mixed.

In order to calculate the phase diagram, the temperature as well as the structural and the interaction constants are specified. Then the F_T is minimised over the order parameter of the side chains S_M and of the backbone, S_B, for each of the possible morphologies. Figure 3.6 shows a sketch of the possible nematic phases and their theoretical LC brush height for planar and homeotropic anchoring to a block copolymer domain separating surface.

Figure 3.7 presents the predicted equilibrium morphologies versus the volume fraction of the LC block ϕ_{LC} and $1/T_{red}$ for a typical side-chain LC – amorphous block copolymer with planar anchoring. (T_{red} is the reduced temperature – $T_{red}{}^2 = \dfrac{(kT)^2}{\varepsilon v_B / l}$, which corresponds to the nematic-to-isotropic phase transition for the polymer backbone (polymer without side-chains). The side-chain and backbone parameters are consistent with the N_I phase, i.e. $S_M > 0$ and $S_B < 0$. The solid lines represent the boundaries between the various morphologies and the dotted lines are contours for different values of the backbone order parameter S_B. When the temperature increases, S_B gradually decreases and ultimately reaches zero. The side-chain order parameter S_M is positive at low temperature and vanishes at T_i. At this temperature the phase boundaries shift.

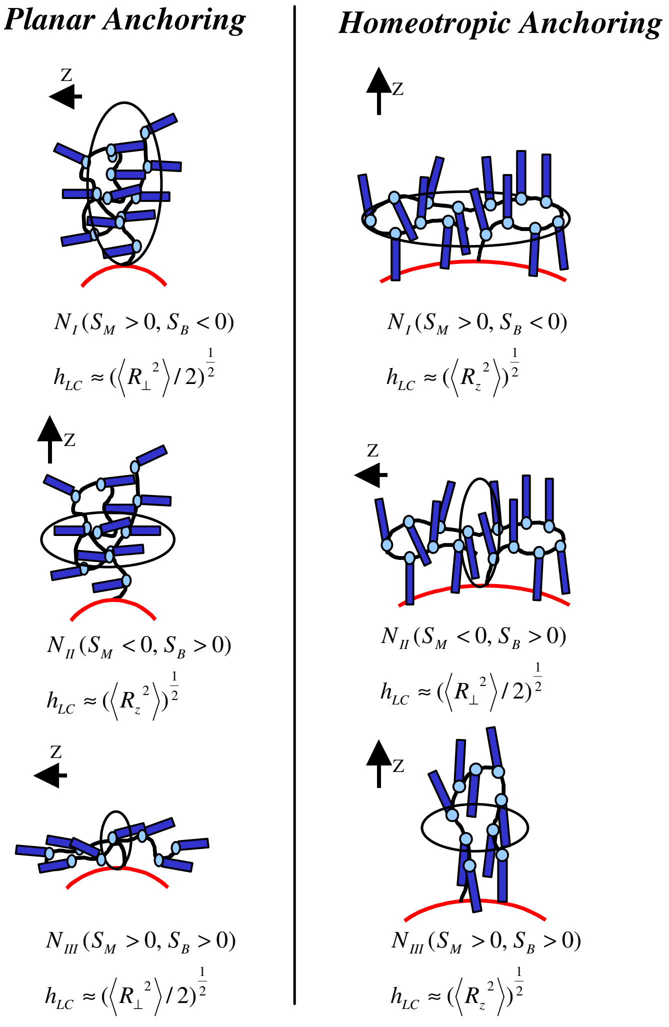

Figure 3.6. Drawing of the possible nematic phases and their theoretical LC brush height for planar and homeotropic anchoring to a block copolymer domain separating surface [35]. Disks lie in the plane orthogonal to the direction of uniaxial symmetry. The figure is redrawn from ref. [35].

Both above and below T_i the phase diagram is asymmetric with respect to that of the amorphous diblock copolymers (Figure 3.7). There is a preference for structures for which the amorphous block is on the concave side of the interface. In this model the mesogenic order is influenced by the domain morphology only at low ϕ_{LC}. At intermediate up to high ϕ_{LC} the structure has little effect on the mesogenic order.

The effect of molecular weight *W* on the predicted phase boundaries is shown in Figure 3.8. In this figure $W = L_A + L_{LC}(x+n)$ is the total molecular weight of the diblock copolymers, including side groups. The value *x* is equal to the length of the side chain divided to the segment length *l*. Finally, *n* is equal of the contour length along the LC backbone between the adjacent side chains divided by *l*. When the molecular weight increases, the phase diagram becomes more asymmetric.

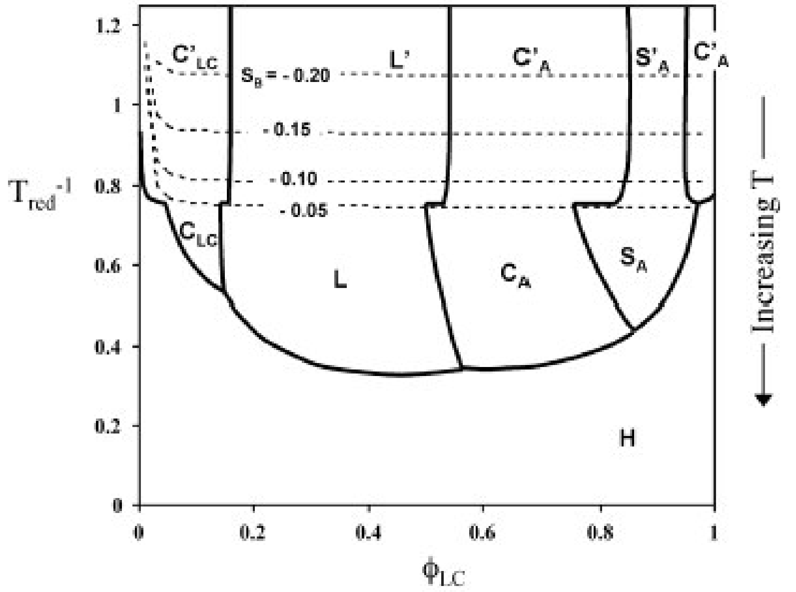

Figure 3.7. Predicted equilibrium phases for side-chain liquid crystal block copolymers with the planar anchoring boundary condition for L_T=2000. The phases are labelled as: S_{LC} – LC spheres, C_{LC} – LC cylinders, *L* – alternating lamellae, C_A – amorphous cylinders, S_A – amorphous spheres and *H*- homogeneous. Dashed lines are contour lines for various values of the backbone order parameter S_B. LC spheres are present for $\phi < 0.004$, but this phase is not shown in the figure [35].

Anthamatten and Hammond further regarded the effect of mesogen-mesogen interactions υ_A on phase diagrams. They showed that when the coupling is stronger, the isotropisation temperature T_i increases and then phase segregation occurs at higher temperatures because of the higher stability of the LC nematic phase.

The phase diagram is also influenced by the side-chain volume fraction *ω*. It is a new parameter, which emerges for the special case of LC/I block copolymers. When *ω* is low (*ω*=0.65), the phase diagram is more symmetric above T_i and is comparable to the phase diagrams of amorphous-amorphous block copolymers. Higher *ω* raises T_i, because of the increased mesogen-mesogen interactions. As a result, the phase diagram becomes more asymmetric.

The authors have also studied the phase behaviour in the case of homeotropic anchored mesogens. This case is not relevant to this thesis. The results can be found in the original article of Anthamatten and Hammond [35].

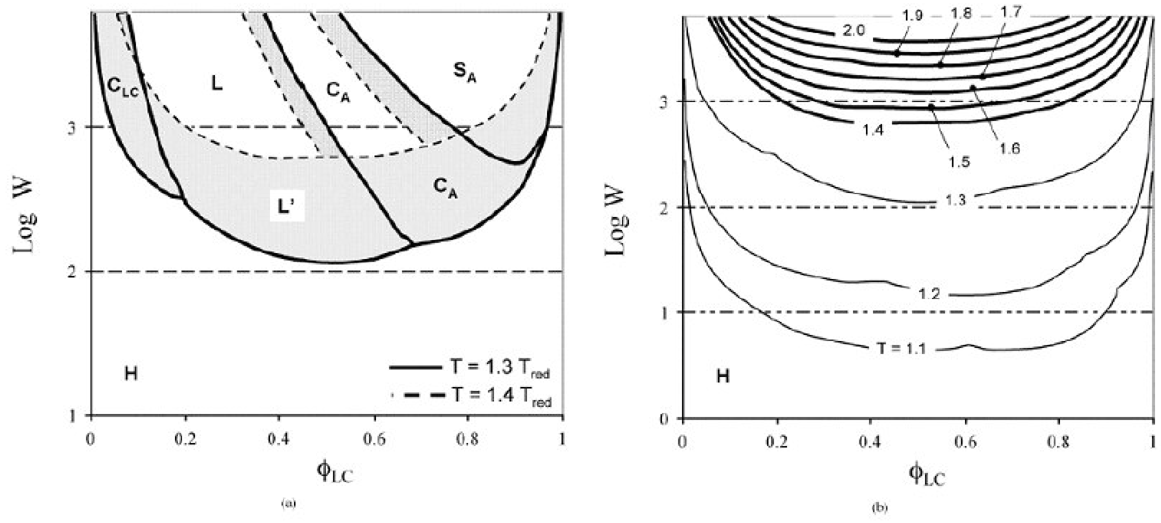

Figure 3.8. Effect of molecular weight W on the equilibrium phases for side-chain liquid crystal block copolymers with a planar anchoring boundary condition. The phases are labelled as: C_{LC} – LC cylinders, L – alternating lamellae, C_A – amorphous cylinders, S_A – amorphous spheres and H- homogeneous. The log W is plotted vs ϕ_{LC}, where $W = L_A + L_{LC}(x+n)$. In Figure 3.8(a) the solid lines correspond to $1.3T_{red}$, and the dashed lines correspond to $1.4T_{red}$. On heating, through $T_i = 1.34T_{red}$, the model predicts order-disorder transitions (vertically hatched regions) and order-order transitions (crosshatched regions). Figure 3.8(b) shows the molecular weight dependence of the phase segregation boundaries for various temperatures [35].

4. Experimental methods and materials

4.1. X-ray scattering

4.1.1. Basic principles

X-ray scattering is a powerful method for characterising the structure of materials. X-ray radiation occupies the electromagenetic wavelength spectrum from about 10^{-3} to 10^{1} nm. For structural investigations, wavelengths between 0.05 and 0.25nm are typically used. Studies on polymers are performed primarily with K_α characteristic radiation from a copper target tube possessing a wavelength of $\lambda_{\mathrm{Cu}} = 0.15418$ nm, which is also the case in the present work. Sometimes, the K_α line of wavelength 0.07107 nm from a molybdenum target tube is used instead, due to a smaller probe wavelength that makes observations over a smaller length scale possible. X-rays of similar wavelengths can also be selected from a broad spectrum of a synchrotron radiation source.

In Figure 4.1, a plane incident X-ray wave travelling in a direction specified by the unit vector $\vec{Q}_0$ is scattered by the particles (i.e. electrons) located at two points, O and P. A detector is placed in the direction specified by the unit vector $\vec{Q}$ located at a distance that is large compared to the spacing between the scattering centres (i.e., sample dimensions). If the scattering is coherent, the phase difference $\Delta\varphi$ between the two waves scattered at points O and P and arriving at the detector depends only on the path length difference $|MP| - |OR|$ of the two rays:

$$\Delta\varphi = \frac{2\pi\,(|MP| - |OR|)}{\lambda}$$

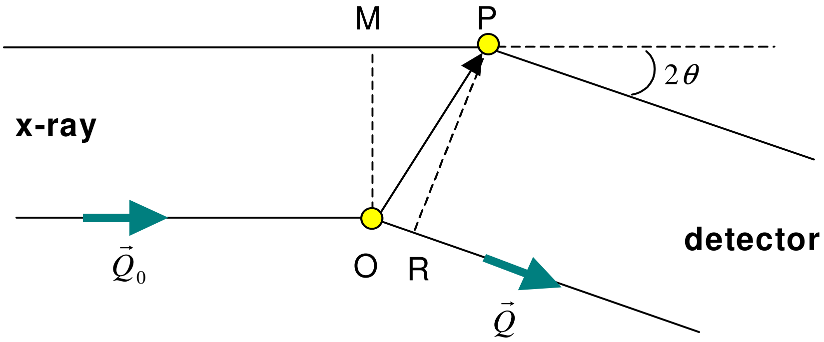

Figure 4.1. The geometry of the path length difference. The figure is redrawn from the Ref. [78].

If the vector $\overrightarrow{OP} = \vec{r}$, we have $\left|\overrightarrow{MP}\right| = \vec{Q}_0 \cdot \vec{r}$ and $\left|\overrightarrow{OR}\right| = \vec{Q} \cdot \vec{r}$. Therefore the phase difference comes out to be

$$\Delta\varphi = \frac{2\pi}{\lambda}(\vec{Q}_0.\vec{r} - \vec{Q}.\vec{r}) = -\vec{q}.\vec{r}$$

where $\vec{q}$ is defined as

$$\vec{q} = 2\pi\frac{\vec{Q} - \vec{Q}_0}{\lambda} = \vec{k} - \vec{k}_0, \tag{4.1a}$$

in which $\vec{k}$ and $\vec{k}_0$ are wave vectors characterizing the scattered and incident radiation, respectively. The vector $\vec{q}$ is referred to as a scattering vector and its magnitude is related to the scattering angle 2θ as

$$|\vec{q}| = q = \frac{4\pi \sin\theta}{\lambda} \tag{4.1b}$$

The amplitude $A(\vec{q})$ of the x-rays scattered by the sample, is given by the equation

$$A(\vec{q}) = A_0 b_e \sum_j e^{-i\vec{q}\vec{r}_j}, \tag{4.2}$$

where b_e is the scattering length of the electron; this expresses the efficiency of the scattering. The term A_0 is the amplitude of the incident beam and $\vec{r}_j$ are the positions of all the electrons in the sample. Since the incident beam is a plane wave and the scattered radiation is a spherical wave, b_e has a dimension of length. It can be expressed as:

$$b_e = r_e\left(\frac{1 + \cos^2 2\theta}{2}\right)^{\frac{1}{2}}, \tag{4.3}$$

where $r_e = \frac{e^2}{mc^2}$ is the classical radius of the electron. e, m and c are the electronic mass, electronic charge and the speed of light, respectively. The numerical value of r_e is $2{,}818.10^{-15}$ m.

When the scatterers are numerous and more or less continuously dispersed in space, the summation can be replaced by integration.

$$A(\vec{q}) = b_e \int_V n_e(\vec{r}) e^{-i\vec{q}\vec{r}} d\vec{r} \tag{4.4}$$

where $n_e(\vec{r})d\vec{r}$ represents the number of electrons within a volume element $d\vec{r} = dxdydz$ around $\vec{r}$ (or $n_e(\vec{r})$ which is the *electron density distribution*). The integration is performed over the scattering volume.

Equation (4.4) can be written as:

$$A(\vec{q}) = \int_V \rho_e(\vec{r}) e^{-i\vec{q}\vec{r}} d\vec{r}\,, \tag{4.5}$$

where $\rho_e(\vec{r})$ is the *electron scattering length density distribution*, which is equal to the *electron density distribution* $n_e(\vec{r})$ multiplied by b_e.

This equation shows that the wave amplitude $A(\vec{q})$ is proportional to the three dimensional Fourier transform of the scattering length density $\rho(\vec{r})$ of the electrons in the sample.

The normalized amplitude is related to the scattering intensity by

$$I(\vec{q}) = \left|A(\vec{q})\right|^2. \tag{4.6}$$

The intensity can be expressed in electron units (eu) per unit volume as:

$$I_{eu}(\vec{q}) = \frac{I(\vec{q})}{V b_e^2}, \tag{4.7}$$

where V is the volume of the illuminated sample. I_{eu} depends only on the sample structure and not on the chosen experimental conditions.

From Eqs. 4.1, 4.3, and 4.6, it follows that the scattered intensity has the highest value in the forward ($2\theta = 0°$) and backward ($2\theta = 180°$) directions and the lowest in the transverse ($2\theta = 90°$) direction. The factor $(1+\cos^2 2\theta)/2$ in Eq. 4.3 is called the polarization factor. This particular form is valid only when the incident beam is unpolarized. The radiation emerging from an X-ray tube is generally unpolarized. When monochromatized with a crystal monochromator, it becomes partially polarized. On the other hand, synchrotron radiation is highly polarized. Since, in this thesis, the polarization factor at small angles is very close to 1, it has been disregarded.

If one inserts Eq. 4.5 in Eq. 4.6, the scattering intensity $I(\vec{q})$ can be expressed as:

$$I(\vec{q}) = A(q)A^*(q) = \left\lfloor \int \rho_e(\vec{u}')e^{-i\vec{q}\vec{u}'} d\vec{u}' \right\rfloor \left\lfloor \int \rho_e(\vec{u})e^{i\vec{q}\vec{u}} d\vec{u} \right\rfloor, \tag{4.8}$$

and after changing the variables by $\vec{r} = \vec{u}' - \vec{u}$, one obtains:

$$I(\vec{q}) = \int \left\lfloor \int \rho_e(\vec{u})\rho_e(\vec{u}+\vec{r})d\vec{u} \right\rfloor e^{-iqr} d\vec{r} = \int \Gamma_\rho(\vec{r})\, e^{-i\vec{q}\vec{r}} d\vec{r} \tag{4.9}$$

where $\Gamma_p(\vec{r})$ is the autocorrelation function of $\rho_e(\vec{r})$, also known as the Patterson function, i.e. the scattering intensity is given by a Fourier transform of the autocorrelation function of the electron scattering length density distribution $\rho_e(\vec{r})$, which defines the structure.

The electron density $n_e(\vec{r})$ can be expressed by mass density $\rho_m(\vec{r})$ in the following way:

$$n_e(\vec{r}) = N_{Av} \frac{Z}{M} \rho_m(\vec{r}) \tag{4.10}$$

where N_{Av} is Avogadro Number, Z is the number of the electrons in the atom or the molecule, M the mass of the atom or the molecule. For any given sample, $N_A \frac{Z}{M} = C = const$. In this way, $I(\vec{q})$ is proportional to the Fourier transform of the mass density $\rho_m(\vec{r})$ correlation function.

The influence of the geometry of the equipment on the intensity of the Bragg reflections can be taken into account applying the Lorentz correction for a powder pattern. For small angle scattering it is given by the equation:

$$I^{LorCorr} = I_{eu}(q).q^2$$

Small- Angle X-ray Scattering (SAXS)

The small angle X-ray scattering (SAXS) method is used for studying structures on length scales ranging from ~1 nm to ~100 nm.

When the structure of the sample (scattering length density distribution $\rho_e(\vec{r})$) is known, it is always possible to calculate the scattering intensity (see Eq. 4.9). On the other hand, by knowing the scattering intensity, one can derive the autocorrelation function of $\rho_e(\vec{r})$ – $\Gamma_p(\vec{r})$ by the inverse Fourier transform of Eq. 4.9. However, knowing $\Gamma_p(\vec{r})$ one can not obtain a unique result for $\rho_e(\vec{r})$ or, in other words, the complete structure of the material. Then, in order to derive $\rho_e(\vec{r})$ from the measured scattering intensity $I(q)$, one has to assume some plausible models for the structure, based on additional information obtained from other experiments. There are four theoretical models most commonly used for SAXS analysis [78]:

1) **Dilute particulate system -** when the particles of one material are dispersed in a uniform matrix of the second material. În this case, when the concentration of the

particles is sufficiently dilute, the positions of the individual particles far apart from each other are uncorrelated.

2) **Nonparticulate two-phase system –** when two different materials are irregularly intermixed and neither of them is considered the host matrix or the dispersed phase. The analysis of scattering data from such a system leads to determination of the parameters characterizing the mean domain size, the specific interface boundary area, and possibly the thickness of the phase boundaries.
3) **Soluble blend system** –a single phase material in which two components (for instance two polymeric species or a polymer and a solvent) are dissolved molecularly as a homogeneous solution in the thermodynamic sense. The examples for such kind of systems are a miscible polymer blend, a block copolymer in disordered state and a polymer solution. This model is applied when one is interested in the thermodynamic properties of the system.
4) **Periodic system** – when the system has a kind of periodic structure. Good examples are block copolymers having ordered microphase segregated domains, semicrystalline polymers, consisting of stacks of lamellar crystals, biological materials, micellar aggregates, etc.

With the help of these models, the experimentally obtained scattering curve $I(q)$ vs. q could be fitted and the structure parameters estimated. The periodic system is the case, most relevant to the present work. As discussed in the previous chapter, the most common structures in microphase separated block copolymers are lamellar alternating layers of A and B type, hexagonally packed cylinders, and spheres ordered on a body-centred cubic (bcc) lattice. The methods developed for the analysis of wide angle diffraction from low molecular weight crystals can be applied to such systems, but some other factors must be also be accounted for, such as the form as well as the finite size of the scatterers etc.

Scattering from Lamellar Structure

Figure 4.2 represents a schematic drawing of the ideal lamellar structure. The PS phase with thickness d_{PS} and uniform scattering length density ρ_{PS} alternates with the LC phase of thickness (d-d_{PS}) with uniform scattering length density ρ_{LC}, where d is the lamellar period. The scattering length density profile $\rho(x)$ can be written as a convolution of two functions

$$\rho(x)=\rho_u(x)*z(x/d) \tag{4.11}$$

where $z(x)$ represents a one dimensional lattice of periodicity *d given by*:

$$z(x)=\sum_{n=-\infty}^{\infty}\delta(x-nd), \tag{4.12}$$

where $\delta(x-nd)$ is the delta function and *n* an integer number.

The term $\rho_u(x)$ represents the scattering length density distribution within a single period ($x\in[0,d]$):

$$\rho_u(x)=\rho_{PS}+\Delta\rho\Pi(x/d_{LC}) \tag{4.13}$$

where

$$\Delta\rho=\rho_{LC}-\rho_{PS} \tag{4.14}$$

and Π is a step function defined as

$$\Pi(x)=\begin{cases}1 & for \quad |x|<\frac{1}{2}\\ 0 & for \quad |x|>\frac{1}{2}\end{cases}$$

After convolution of these two functions, a periodic function with a period *d is obtained.* Within every period, the scattering length density distribution is $\rho_u(x)$.

The scattering intensity *I(q)* along the line normal to the lamellae can be obtained by taking the absolute square of the Fourier transform of $\rho(x)$ (see Eq. 4.5 and 4.6). According to the convolution theorem, the Fourier transform of $\rho(x)$ may be shown to be a multiplication of the Fourier transforms of $\rho_u(x)$ and $z(x)$, or

$$I(q)\propto|F(q)|^2\,z(\frac{qd}{2\pi}) \tag{4.15}$$

Now using $\rho_u(x)$, $|F(q)|^2$ can be expressed as [78]:

$$|F(q)|^2=(\Delta\rho)^2\frac{4}{q^2}\sin^2(\frac{q\,d_{LC}}{2}) \tag{4.16}$$

Then, it follows that,

$$I(q)\propto(\Delta\rho)^2\frac{4}{q^2}\sin^2(\frac{qd_{LC}}{2})\,z(\frac{qd_{LC}}{2\pi}). \tag{4.17}$$

From the equation 4.17, it follows that Bragg peaks occur at scattering vectors $q = \frac{2\pi n}{d}$ and that the integrated area under the n^{th} order peak is proportional to $\sin^2(\pi n \phi_{LC}) / n^2$, where $\phi_{LC} = d_{LC} / d$ is the volume fraction of the LC phase. When the volumes of the phases are equal, then every even order peak vanishes.

The lamellar period can be obtained from the position q_n of the n-th order maximum from:

$$d = \frac{2\pi n}{q_n}. \tag{4.18}$$

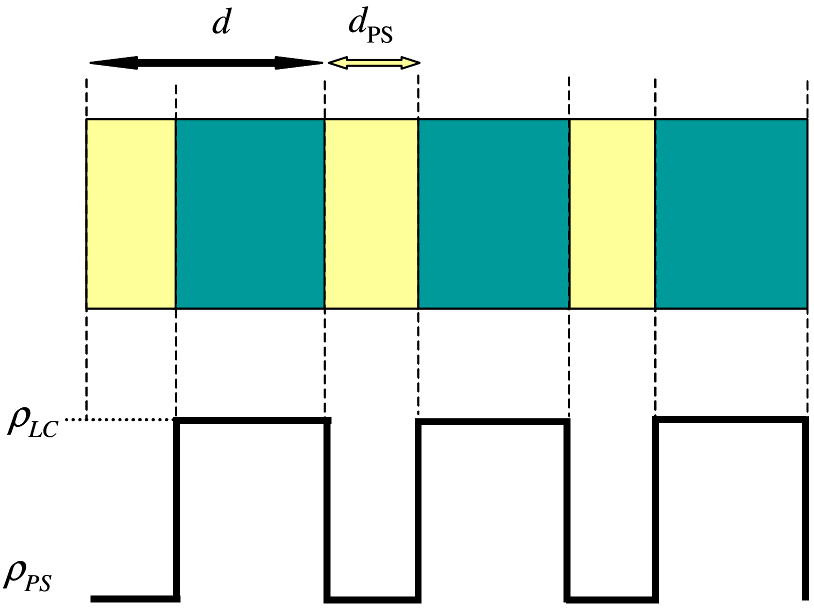

Figure 4.2. Lamellar structure. The two colours correspond to the two different phases: LC and PS.

An alternative method for estimating the lamellar period is to calculate the *one-dimensional electron density correlation function* $K(z)$ (Figure 4.3). This method, developed by Strobl [79] for the analysis of partially crystalline polymers, regards partially crystalline systems with lamellar structures, i.e. alternating amorphous and crystalline layers. It can be applied analogically to block copolymer systems with lamellar structures. It is a more general approach and can also be applied to not so well ordered structures with irregular lamellae stucks. The lamellae period d in block copolymers is more uniform in comparison with this in partialy crystalline polymers. However, the lamellae are not plane, but bent, therefore, this is a useful method for evaluating the block copolymer structure.

If the z-axis is chosen perpendicular to the lamellar surface, $K(z)$ can be represented as [79]:

$$K(z) = \frac{1}{2r_e^2\pi^2}\int_0^\infty \cos(qz)q^2 I_{eu}(q)dq \tag{4.19}$$

where r_e is the classical electron radius and z is the distance in direction, normal to the lamellar surface. $I_{eu}(q)$ is the scattering cross section (see Eq. 4.7) per unit volume.

Figure 4.3 (a) shows $K(z)$ for the ideal system. The lamellar period is denoted as d, the thickness of the PS layer as d_{PS} and the electron density difference as $n_{e,LC}$-$n_{e,PS}$. The volume fraction of PS, $\phi_{PS} = \frac{d_{PS}}{d}$ is assumed to be below 0.5. This means, that the PS part of the lamella is thinner than the LC part and its thickness d_{PS} can be directly derived from the correlation function, as will be shown later in this thesis. When $\phi_{LC} = \frac{d_{LC}}{d} < 0.5$, the evaluation can be performed analogically, i.e. d_{LC} can be derived from the correlation function and d_{PS} calculated as d-d_{LC}.

$K(z)$ has a characteristic shape– a periodic sequence of triangles, centred at z = 0, d, 2d etc. The first triangle at z = 0 represents the self-correlation, the second – the correlation between the first neighbours, the third – the correlation between second neighbours, and so on. The lamellar period d can be derived directly from the position of the second triangle. The triangles have a common 'base-line' located at K=-B. The correlation function $K(z)$ reaches the base-line at z = d_{PS}, which is equal to the dimension of the thinner part of the lamella (which in the particular case means the thickness of the PS block– d_{PS}). n_{eLC} and n_{PS} denote the electron densities of the LC and PS parts, correspondingly. The value of K at z=0, denoted as Q, is $Q = \phi_{PS}(1-\phi_{PS})(n_{e,LC} - n_{e,PS})^2$.

Figure 4.3 (b) shows the correlation function in case of systems with variations in lamellae thickness. One can see that the self-correlation part (the initial slope) remains unchanged, however the second and the third peak change their triangular shape, decrease and become broader. The additional influence of the non-uniform thickness on the correlation function is shown in Figure 4.3 (c). Here it is evident that a modification occurs near to the base line of the triangle, implying that $K(z)$ becomes curved. Finally, Figure 4.3 (d) adds the effect of the diffuse interface existing between the LC and the PS regions. In this case, $K(z)$ becomes curved in the vicinity of z=0.

The calculation of the correlation function was performed using the computer program "Correl", created in Prof. Strobl group (University of Freiburg, Department of Physics). Before applying the program to the experimental data, the Lorenz correction of the intensity was first performed and the background was subsequently subtracted.

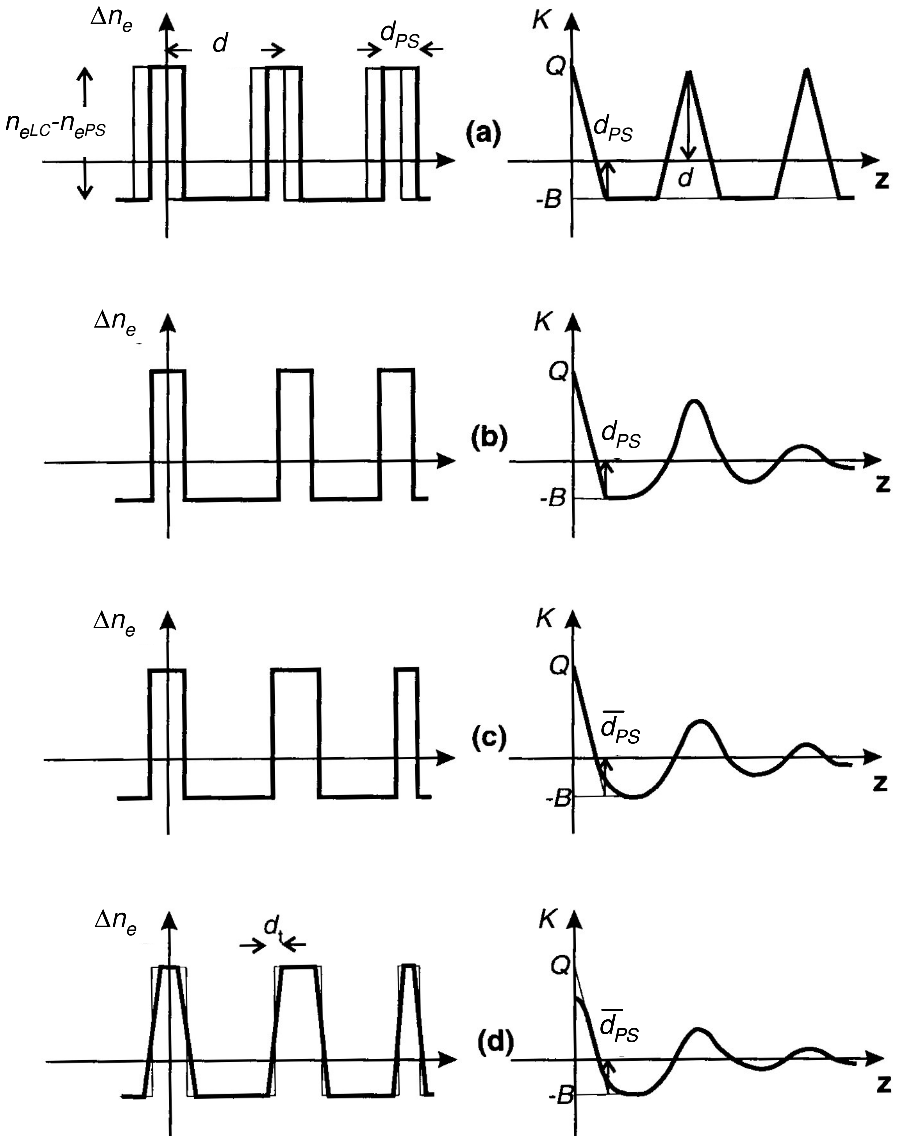

Figure 4.3. Two-phase layered system. Electron density distribution $\Delta n_e(z) = n_e(z) - \langle n_e \rangle$ and the associated one-dimensional correlation function $K(z)$ for a perfectly ordered system showing (a) the effects of varying the intercrystalline spacing, (b) crystallite thickness and (c) the diffuse interfaces (d) [79].

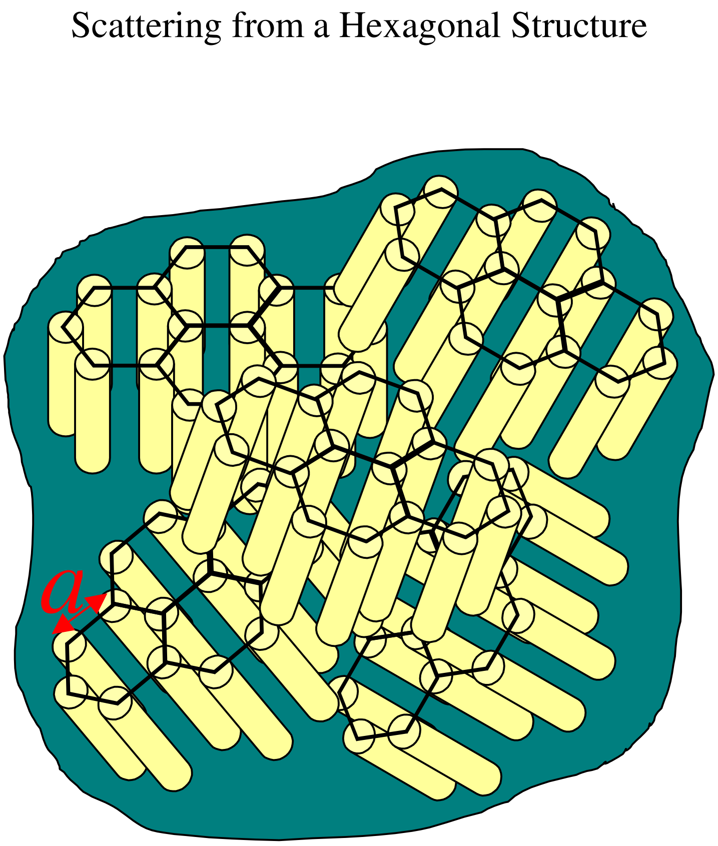
Scattering from a Hexagonal Structure

Figure 4.4. Schematic drawing of isotropic, randomly ordered domains of hexagonally packed cylinders. The background represents the polymer matrix, which fills the space in between the domains. It has been made to be transparent so that all the cylinders can be seen. In this drawing the domains consist of only four hexagonal cells.

The hexagonal microstructure consists of cylinders of one copolymer block ordered in a hexagonal lattice situated in a continuous matrix of the other block (Figure 4.4). It has two dimensional order in the plane perpendicular to the cylinder axis.

In the case of the hexagonal lattice structure, the scattering intensity $I_{eu}(q)$ can be decomposed into three components:

1) I_{Bragg} – Bragg reflections from the block copolymer microstructure modulated by the form factor of the scattering microdomains;
2) I_{diff} – diffusive scattering from the positional disorder and the size distribution of the microdomains;
3) I_k – background scattering due to the density fluctuations [27, 28, 41, 80]:

$$I_{eu}(q) = I_{Bragg} + I_{diff} + I_k \tag{4.20}$$

The scattered intensity of the Bragg reflections for a scattering vector with length q in an isotropic sample is given by [27]:

$$I_{Bragg} = \sum_{\{hkl\}} \overline{\Phi}^2(q_{hk}) \frac{j_{hk}}{q^2} G_{hk}(q;\sigma) \exp\{-q_{hk}{}^2 u^2/3\} \tag{4.21}$$

The summation if performed over all group reflections $\{hk\}$ in the two dimensional hexagonal lattice. j_{hk} is the multiplicity of reflection $\{hk\}$ and $1/q^2$ is the Lorenz factor for an isotropic distribution of the scatterers. $G_{hk}(q;\sigma)$ is a normalized Gaussian centred at q_{hk} with a variance of σ. The peak position q_{hk} is directly related to the lattice constant (i.e. the intercylinder distance) [27]:

$$q_{hk} = \frac{2\pi}{a}\sqrt{\frac{4}{3}(h^2 + k^2 + hk)} \tag{4.22}$$

For the $\{100\}$ reflection, $q^* = q_{100} = \dfrac{4\pi}{\sqrt{3}a}$, where a is the lattice constant (Figure 4.4).

The form factor of cylinders Φ accounts for the shape of the scatterers – they are not point-like objects, but domains with finite size. It can be expressed by the equation [27, 81]:

$$\Phi(q) = 2V \int_0^{2\pi} \frac{\sin(\frac{qL}{2}\cos\alpha)}{\frac{qL}{2}\cos\alpha} \frac{J_1(qR\sin\alpha)}{qR\sin\alpha} d\alpha \tag{4.23}$$

where V, L and R are the volume, length and radius of the cylinders, respectively, J_1 is the first order Bessel function and α is the angle between the cylinder axis and the scattering vector q. Eq. (4.23) is typically evaluated numerically.

The exponent in equation (4.21) represents the Debye – Waller factor. Its physical origin is the deviation of the location of individual scatterers from their equilibrium position. The mean squared displacement is u^2. This type of lattice distortion also gives a diffuse scattering I_{diff} [41].

$$I_{diff} \propto (1 - \exp(q^2 u^2/3))\overline{\Phi}^2 + (\overline{\Phi^2} - \overline{\Phi}^2) \tag{4.24}$$

Here $\overline{\Phi}$ is the average value of Φ over the various radius distributions.

Due to the large size of the scattering objects, this term depends on q, which can be used to obtain more information on the radius of the cylinders.

The last term – I_k in equation (4.20) represents the background due to density fluctuations. It is directly proportional to the temperature and compressibility of the material – $I_k \propto k_B \kappa T$, where k_B is the Bolzmann constant and κ is the compressibility. Fitting of the experimental data to the function (4.20) provides the lattice constant a and the radius of the cylinders R.

Scattering from Body Centered Cubic (bcc) Structure

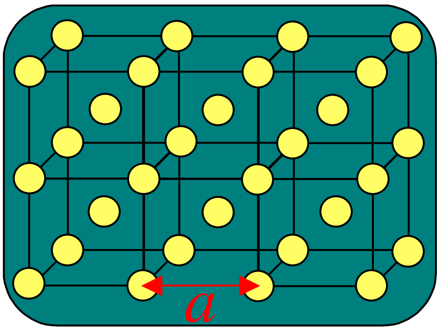

Figure 4.5. Schematic drawing of a bcc lattice. Only six unit cells are shown for clarity. The background represents the polymer matrix, which fills the space in between the spheres. For better visibility it has been made to be transparent.

Figure 4.5 shows a sketch of the bcc lattice. The evaluation of the scattering curves for a bcc lattice is analogous to that of the hexagonal lattice discussed above. The same equations- (4.20), (4.21) and (4.24) are used but, in this case, the form factor Φ is different. The form factor for a sphere is [82]:

$$\Phi(q) = 3V \frac{\sin(qR) - qR\cos(qR)}{(qR)^3} \tag{4.25}$$

where V and R is the volume and the radius of the sphere, respectively. Unlike Eq. 4.23, the integration here is not necessary due to the fact that the spheres are centro-symmetrical.

In case of the bcc lattice, the peak position q_{hkl} is related to the lattice constant as [83]:

$$q_{hkl} = \frac{2\pi}{a}\sqrt{h^2 + k^2 + l^2}$$

The $\{100\}$ reflection cannot be seen in the bcc lattice, because of the particular symmetry of this lattice. The reflection at the smallest q value, which can be detected is $\{110\}$. Then $q^* = q_{110} = \frac{2\sqrt{2}\pi}{a}$, where a is the lattice constant (Figure 4.5).

Scattering from liquid-like ordered hard spheres

When the microdomain distribution in diblock copolymers with asymmetric composition is in between the disordered and the bcc ordered state, the system can be represented as a liquid, consisting of hard spheres [28, 29, 30] (Figure 4.6).

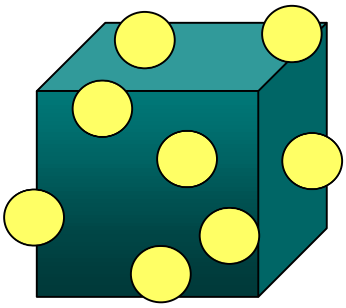

Figure 4.6. Liquid-like ordered hard spheres.

Such kind of structures may be well described by the Percus-Yevick model. In this case the scattered intensity is given by:

$$I_{eu}(q) = K_{PY}\overline{\Phi}^{2}(q,R)S(q,R_{hs},\phi) + I_k\,, \tag{4.26}$$

where the prefactor K_{PY} depends on the electron density difference between the domains and the matrix, Φ is the form factor of the spherical domains (Eq. 4.25), which needs to be averaged over their size distribution by a Gaussian function [28]. The term $S(q,R_{hs},\phi)$ is the interference structure factor, which can be expressed by:

$$S(q,R_{hs},\phi) = \frac{1}{1+\dfrac{24\phi G(A)}{A}} \tag{4.27}$$

where $A = 2qR_{hs}$;

$$G(A) = \frac{\alpha_{PY}}{A^2}(\sin A - A\cos A) + \frac{\beta_{PY}}{A^3}(2A\sin A + (2-A^2)\cos A - 2) + \frac{\gamma_{PY}}{A^5}\left\{-A^4\cos A + 4\left[\left(3A^2-6\right)\cos A + \left(A^3-6A\right)\sin A + 6\right]\right\} \tag{4.28}$$

where $\alpha = \dfrac{(1+2\phi)^2}{(1-\phi)^4}$; $\beta = \dfrac{-6\phi(1+\phi/2)^2}{(1-\phi)^4}$; $\gamma = \dfrac{\phi(1+2\phi)^2}{2(1-\phi)^4}$,

R is the radius of the spherical domains, R_{hs} is the effective hard sphere radius, which describes the range of the interaction between the domains, ϕ is the effective hard sphere volume fraction of the spheres and I_k is the scattering background due to the density fluctuations.

4.1.2 Measurement technique

Small-Angle X-ray Scattering

SAXS measurements were performed using a Kratky compact small-angle system (Anton Paar, Graz, Austria) (Figure 4.7) equipped with a scintillation counter operating in the step-scanning mode. Cu K_α radiation (see above) was provided by a sealed X-ray tube and an X-ray generator (Kristalloflex 710H, Siemens Germany). A Ni filter was used to suppress the contributions from K_β radiation. The sample-to-detector distance was 200 mm. The widths of the entrance slit and the detector slit were 80 μm and 150 μm, respectively. The camera volume was kept under vacuum during measurements to reduce background scattering from air. A temperature-controllable sample holder with a filament and an Eurotherm 2404 controller provided temperature stabilization in the range of 25 °C to 150 °C with a precision of ±0.1 °C.

Samples of the block copolymers were prepared in the form of uniform homogeneous bars with 2 mm thickness in the following way: block copolymer powder was placed in a stainless steel sample holder and set under pressure, then heated up to 150 °C to melt them and subsequently annealed under vacuum. This temperature was chosen so as to be above the $T_{g_{PS}}$ of the PS block (~100 °C) and the $T_{g_{LC}}$ (~30 °C) and the T_{i} (and 112 °C-123 °C) of the LC block. The samples were then placed in brass sample holders with acetate windows.

SAXS measurements were carried out during both, heating and cooling cycles in steps of 10 degrees. Following each temperature change the sample was equilibrated for 30 minutes. Before every measurement cycle, the position of the primary beam was determined as explained below. We have used a slit collimated primary beam in order to have a larger primary beam intensity.

The primary beam has a lateral intensity profile shown in Figure 4.8a (a trapezoid). Therefore, when placed at a certain height *h,* the detector not only records the radiation at the scattering vector $\vec{q}$, but also at $\vec{q}_1,\ldots,\vec{q}_n$ (Figure 4.9). The resulting intensities are consequently *slit-smeared* and have to be corrected by a mathematical procedure called *desmearing*, to their equivalent pin-hole values. The integral intensity of the measured curve $\tilde{I}(h)$ could be presented as [84]:

$$\tilde{I}(h) = \int_{b=h}^{\infty} g(h,b) I_p(b) db . \tag{4.29}$$

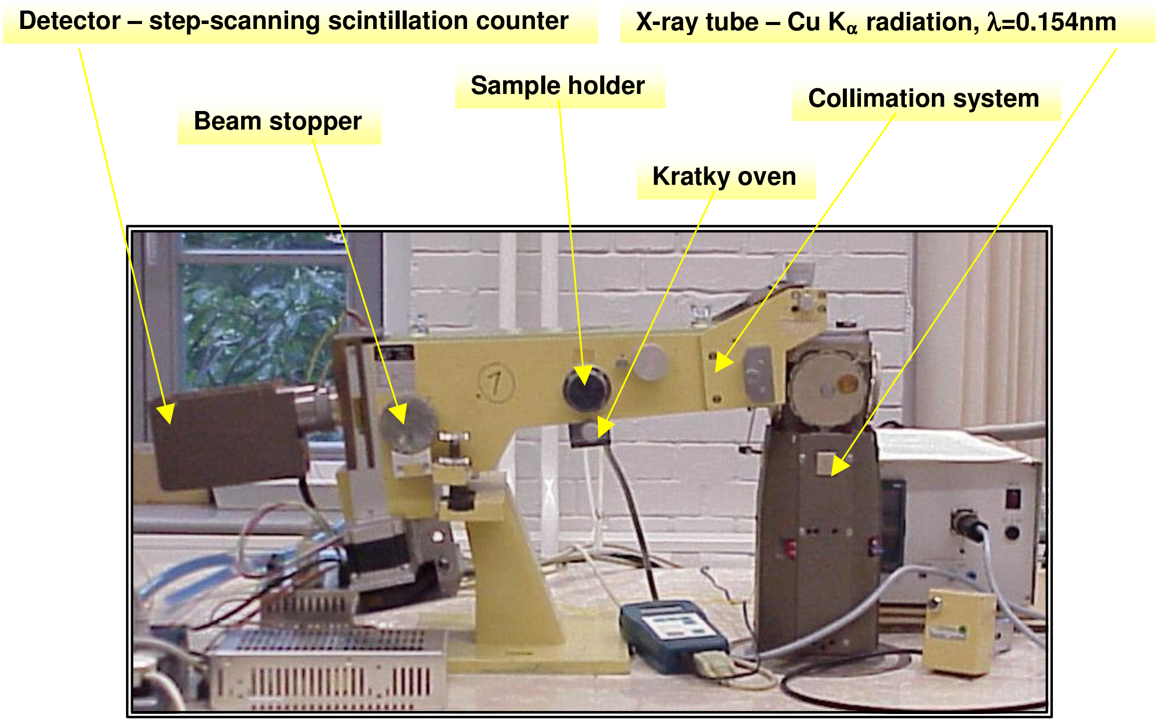

Figure 4.7. Kratky camera.

Here $I_p(b)$ is the corresponding pinhole scattering intensity distribution in the plane of registration (Figure 4.9). The weighting function $g(h,b)$ depends on the collimation-system and registration-system geometries. $g(h,b)$ includes several factors– the length and the width of the detector slit, and the lateral distribution of the primary beam intensity. In this thesis, the latter has the form of a trapezoid (Figure 4.8a). Knowing $g(h,b)$ and $\tilde{I}(h)$, $I_p(b)$ can be recovered through inversion of the integration of Eq. (4.29).

The desmearing was accomplished by the Strobl method [84] using a custom-designed computer program. In this program, the calculations could be applied to the measured curves without any smoothing. The procedure requires some additional measurements. At first, the background scattering has to be measured. The program then subtracts it from the experimental data. Later, the primary beam intensity with a sample and without a sample has to be measured. The measured intensity is subsequently integrated along the full length of the beam profile and has a certain lateral length (Fig. 4.8a).

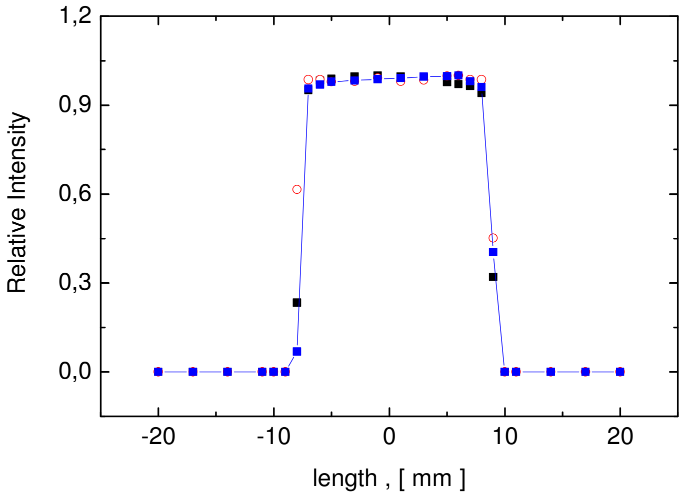

a)

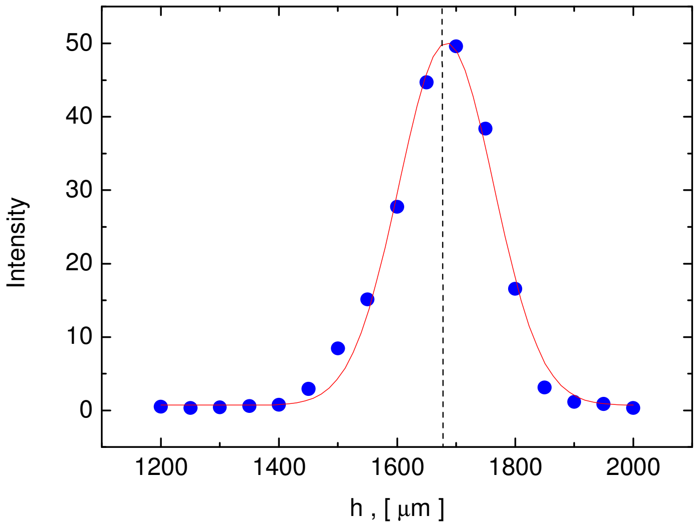

b)

Figure 4.8. The primary beam horizontal profile (a) and the vertical profile (b)

In order to measure the “point” intensity, we cut a very thin vertical slice from the trapezoid center with the help of a moving slit device (Wanderspalt) and a vertical detector slit. The Wanderspalt has a very thin vertical slit, which can move in a plane perpendicular to the primary beam. In this way, the detector is hit by the primary beam for a very short time interval at a certain “point” and the “point” intensity is measured. In addition, the intensity, passing through the Wanderspalt and the vertical slit is not very high and the detector cannot be destroyed. The measured intensities were inputted in the program in order to correct the experimental curve for the absorption of the material. The program gives as output a desmeared curve with normalized intensities for unit volume in electron units – $I_{\mathrm{eu}}(q)$.

The height profile of the primary beam (suitably attenuated) is measured (Figure 4.8b and its centre of gravity is taken as the zero of the detector height (the position of the dashed line on Figure 4.8b).

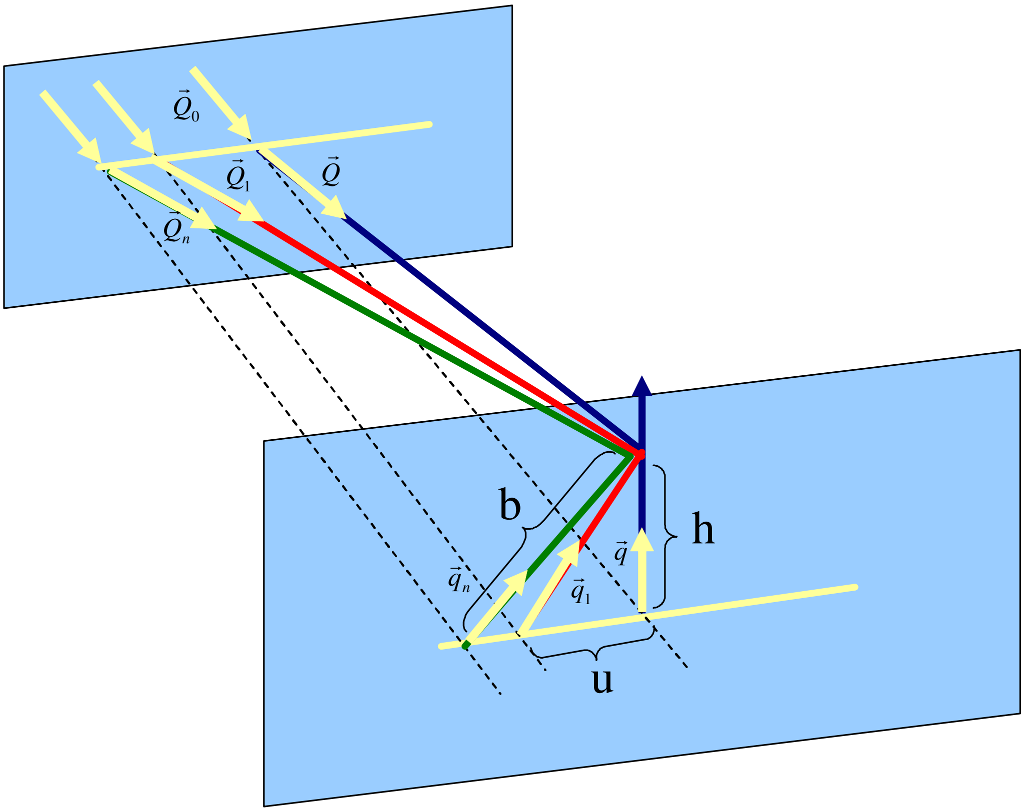

Figure 4.9. Measurement geometry to illustrate slit smearing. Here $\vec{Q}_0$ is the incident beam unit vector, $\vec{Q}$ is the unit vector of the scattered radiation from the centre of the sample, $\vec{Q}_1$ and $\vec{Q}_n$ are the unit vectors of the scattered radiation from different (non-central) parts of the sample. $\vec{q}$, $\vec{q}_1$ and $\vec{q}_n$ are the corresponding scattering vectors. The figure was drown using Ref. [78] and [84].

Wide angle X-ray diffraction (WAXD)

In this thesis, wide angle X-ray diffraction (WAXD) measurements were performed using the X'Pert-PRO Philips diffractometer using a PW3050/60 Theta/Theta goniometer with a radius of 24 cm. The voltage and the current generated from the PW3040 generator were set at 40 kV and 40 mA, respectively. The wavelength of 1.54 Å (CuK_α radiation) was selected by a secondary curved crystal pyrolitic graphite monochromator. Two soller slits of 0.04 rad, one in the incident and one in the diffracted beam optics, were used to control the axial divergence of the X-ray beam. A programmable divergence slit with an irradiated length 10mm was used to restrict the X-ray spot in direction parallel to the beam path. A 10 mm beam mask confined the spot in the direction perpendicular to the beam. The scattering profiles were registered by a sealed proportional detector. The measurement was done at room temperature using a spinner stage PW3064. The type of the scan was θ-2θ: – the angle between the incident and diffracted beam was always double the angle between the incident beam and the sample plane. This geometry was realized as the sample was fixed parallel to the *x-y* plane and the X-ray source and the detector were moving with equal speed (Figure 4.10). The measurements were done using continuous scan mode with a step of 0.02°. In order to achieve better statistic (placing different parts of the circlet sample in the irradiated recrangle), the sample was rotated around the angle φ at a rate one revolution per second (Figure 4.10).

Samples were prepared in the same steel tool used for SAXS. However, in this case they were made in a disk-like shape. The diameter of the disk was 13 mm and the height-about 1-2 mm.

Unlike the case of SAXS, here it is not necessary to desmear the data, because the soller slits restrict the axial divergence of the primary and the scattered beams.

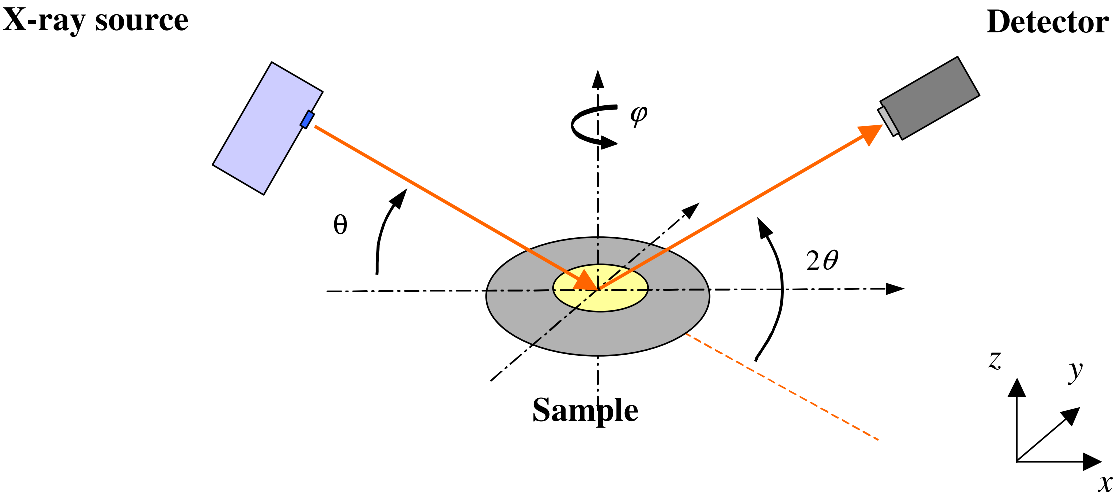

Figure 4.10. Schematic picture of the WAXD geometry.

4.2. Dielectric Relaxation Spectroscopy

4.2.1. Basic theory

The dielectric spectroscopy (DS) is one of the most powerful methods for studying the molecular dynamics in liquid crystalline materials. It covers a broad timescale of motions, from about 10^4s to 10^{-11}s.

When a sample is brought into a static external field, all charged particles experience forces tending to move them along the field in the appropriate direction. This results in dielectric polarization of the sample on several length scales [74]:

1) *induced electronic polarization* – occurs due to the displacement of the electrons in respect to the nuclei;
2) *atomic polarization* – due to the displacement of atoms or group of atoms relative to each other;
3) *orientational polarization* – due to the orientation of the molecules having permanent dipole moments in the field direction;
4) *interfacial polarization* – due to the movement of the free ions toward the surface.

The mean dielectric polarization $\vec{P}$ of the homogeneous system is equal to the dipole density [74]:

$$\vec{P} = \frac{\langle \vec{M} \rangle}{V},$$

where V is the volume of the sample, and $\langle \vec{M} \rangle$ is the average total dipole moment of this volume. If the material is isotropic, then $\langle \vec{M} \rangle$ has a direction of the electric field and the polarization is proportional to the field strength $\vec{E}$:

$$\vec{P} = \varepsilon_0 \chi_{DI} \vec{E} = \varepsilon_0 (\varepsilon - 1) \vec{E} \tag{4.30}$$

where ε_0 is the dielectric permittivity of vacuum, χ_{DI} is the dielectric susceptibility and ε is the dielectric permittivity of the material. Then the dielectric displacement can be expressed as:

$$\vec{D} = \varepsilon_0 \vec{E} + \vec{P} = \varepsilon_0 (1 + \chi_{DI}) \vec{E} = \varepsilon_0 \varepsilon \vec{E} \tag{4.31}$$

If an alternating sinusoidal field is applied:

$$\vec{E}^{*} = \vec{E}_0 \exp i\omega t, \tag{4.32}$$

then the dielectric polarization of the material is a time dependent function $\vec{P}(t)$:

$$\vec{P}^{*}(t) = \vec{P}_0 \exp i(\omega t - \delta_\omega) \tag{4.33}$$

where the angle δ_ω denotes the phase difference between the electric field and the dielectric polarization.

In order to study the dielectric response of a material to alternative fields, it is convenient to use the *complex dielectric permittivity* $\varepsilon^{*}(\omega)$:

$$\vec{D}^{*}(t) = \varepsilon_0 \varepsilon^{*}(\omega) E^{*}(t) \tag{4.34}$$

$$\varepsilon^{*}(\omega) = \varepsilon'(\omega) - i\varepsilon''(\omega), \tag{4.35}$$

where the "-" sign is conventionally chosen. ε' is the frequency dependent dielectric "constant" ; ε'' is called the dielectric loss factor; and δ_ω is the loss angle ($\tan(\delta_\omega) = \varepsilon''/\varepsilon'$).

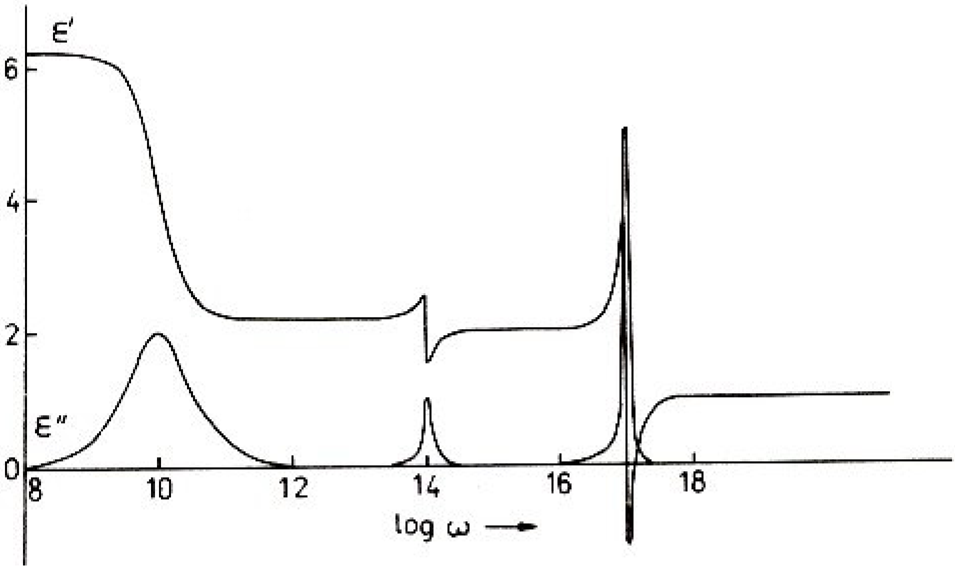

Figure 4.11. Dielectric constant ε' and loss factor ε'' as a function of frequency for a polar material in the condensed state. The figure is adopted from the J. K. Moscicki article [74].

The dielectric "constant" $\varepsilon'(\omega)$ and the loss factor $\varepsilon''(\omega)$ as a function of the frequency for a polar material in the condensed state are shown on Figure 4.11. If the frequency is low, all contributions to the polarization have enough time to build up and the polarization is in equilibrium with the electric field. In such a case $\varepsilon'(\omega)$ is equal to the static dielectric constant $\varepsilon(0)$ and $\varepsilon''(\omega)=0$. With increasing of frequency, several dispersion regions are observed, associated with the orientational, atomic and electronic polarization. $\varepsilon''(\omega)$ shows narrow peaks which correspond to the changes in $\varepsilon'(\omega)$. Dielectric spectroscopy is applied in the frequency region of orientational polarization.

The complex dielectric permittivity is related to the time autocorrelation function of the total dipole moment of the sample $\vec{M}$ by [74]:

$$\frac{\varepsilon^*(\omega)-\varepsilon_\infty}{\varepsilon(0)-\varepsilon_\infty} = p_\alpha\left[1-i\omega L_{i\omega}\{F(t)\}\right] = p_\alpha L_{i\omega}\left\{-\dot{F}_D(t)\right\} \tag{4.36}$$

where $F_D(t)=\frac{\langle \vec{M}(0)\vec{M}(t)\rangle}{\langle \vec{M}(0)\vec{M}(0)\rangle}$, is the normalized autocorrelation function of $\vec{M}$ or the macroscopic correlation function and $L_{i\omega}$ denotes the Laplace transform. ε_∞ is the dielectric constant at frequencies much higher than this of the orientational polarization. p_α is a proportionality factor, which accounts for the polarizability of the sample and depends on the shape of the sample and on $\varepsilon(0)$ and ε_∞.

The parameter $\varepsilon(0)-\varepsilon_\infty = \Delta\varepsilon$ is called dielectric relaxation strength and is an important characteristic of the material.

For an ideal case, $F_D(t)$ is a simple decay function [74]

$$F_D(t) = \exp\left(-\frac{t}{\tau_0}\right). \tag{4.37}$$

The decay constant τ_0 which is specific for every single relaxation process (Debye relaxation) is called dielectric relaxation time. The complex dielectric constant in this simple case is given by:

$$\varepsilon^*(\omega)-\varepsilon_\infty = \frac{\Delta\varepsilon}{1+i\omega\tau_0} \tag{4.38}$$

In this case the dielectric loss factor ε'' can be expressed as:

$$\varepsilon''(\omega) = \Delta\varepsilon\frac{\omega\tau_0}{1+\omega^2{\tau_0}^2}$$

and has a maximal value at $\omega\tau_0 = 1$.

If the orientational polarization arises from different dipole moments or the orientation of the dipoles is anisotropic, the Eq. 4.38 is not more valid. Then, the autocorrelation function for a discrete distribution of the relaxation times can be written as:

$$F_D(t)=\sum_k g_k \exp\left(-\frac{t}{\tau_k}\right) \qquad \sum_k g_k = 1, \tag{4.39}$$

where g_k are normalized weighting coefficients. When the distribution is continuous the sum is replaced by an integral:

$$F_D(t)=\int_0^\infty g(\tau)\exp\left(-\frac{t}{\tau}\right)d\tau \quad \int_0^\infty g(\tau)d\tau = 1 . \tag{4.40}$$

Therefore the equation 4.38 can be written in the following form:

$$\varepsilon^*(\omega)-\varepsilon_\infty = \Delta\varepsilon \sum_k \frac{g_k}{1+i\omega\tau_k} \tag{4.41}$$

or

$$\varepsilon^*(\omega)-\varepsilon_\infty = \Delta\varepsilon \int_0^\infty \frac{g(t)}{1+i\omega\tau}d\tau \tag{4.42}$$

In the most cases the relaxation processes are more complicated and can not be described by the Debye function. Then, for fitting of the experimental curves several other empirical expressions may be used:

Cole-Cole

$$\varepsilon^*(\omega)-\varepsilon_\infty = \frac{\Delta\varepsilon}{1+(i\omega\tau_0)^\alpha} \tag{4.43}$$

where $0<\alpha\le 1$

The Cole-Cole function describes a symmetric broadening of the dielectric function compared with Eq. 4.38.

Davidson-Cole

$$\varepsilon^*(\omega)-\varepsilon_\infty = \frac{\Delta\varepsilon}{(1+i\omega\tau_0)^\gamma} \tag{4.44}$$

where $0<\gamma\le 1$

Davidson-Cole function corresponds to an asymmetrical broadening of the dielectric function.

Havriliak-Negami [85]

$$\varepsilon^*(\omega)-\varepsilon_\infty = \frac{\Delta\varepsilon}{\left[1+(i\omega\tau_0)^\alpha\right]^\gamma} \tag{4.45}$$

where $0<\alpha\le 1$ and $0<\alpha\gamma\le 1$.

The shape parameters α and γ describe the symmetric and asymmetric broadening of the relaxation peak, respectively. In the case of $\gamma = 1$, the Havriliak-Negami function coincides with the Cole-Cole equation. When $\alpha = 1$, it transforms in the Davidson- Cole equation. In general, the maximum value of the asymmetric Havriliak-Negami and Davidson-Cole functions does not coincide with the relaxation time τ_0.

Fuoss-Kirkwood

$$\varepsilon''(\omega) = \varepsilon''_{\max} \sec h(\alpha' \ln \omega\tau_0) \qquad 0 < \alpha' \le 1 \tag{4.46}$$

where $\varepsilon''_{\max}$ is the dielectric loss maximum and α' is a phenomenological parameter. The Fuoss-Kirkwood equation describes symmetric relaxation processes.

Figure 4.12 shows the values of $\varepsilon''(\omega)/\Delta\varepsilon$ for the Debye, Cole-Cole, Davidson-Cole and Havriliak-Negami functions and $\varepsilon''(\omega)/\varepsilon_{\max}''$ for the Fuoss-Kirkwood function, calculated for a relaxation time $\tau = 0{,}001\,s$ and various values of the parameters α, γ and α'. The explicit expressions for $\varepsilon''(\omega)$ can be found in [86] and [93].

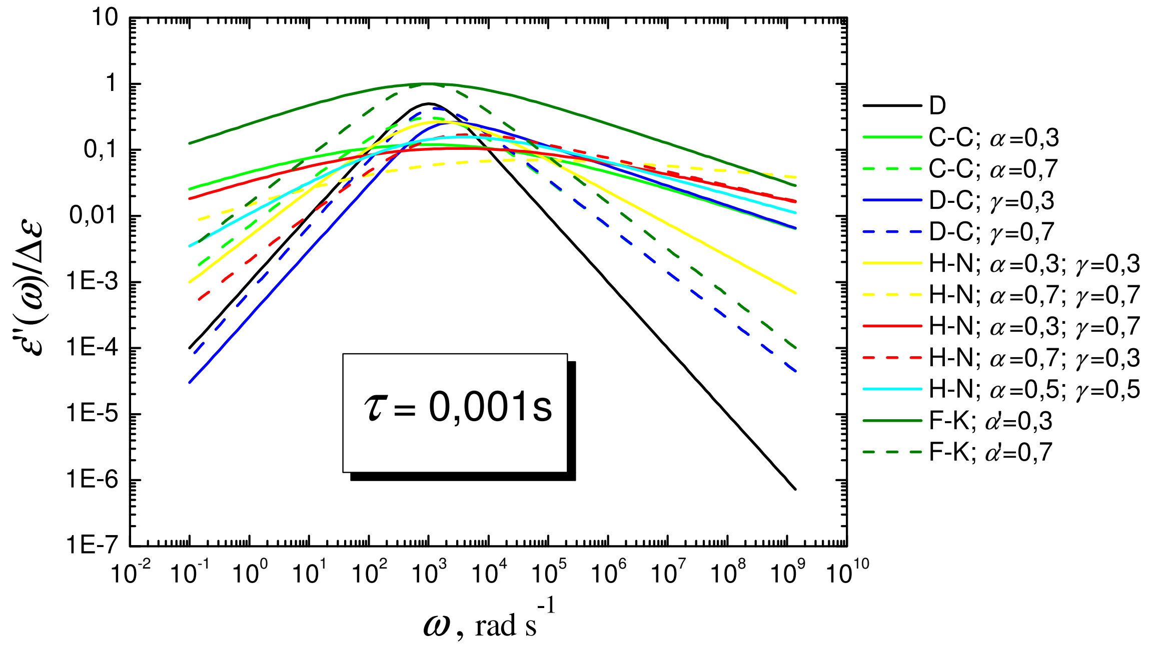

Figure 4.12. $\varepsilon''(\omega)/\Delta\varepsilon$ for the Debye (D), Cole-Cole (C-C), Davidson-Cole (D-C) and Havriliak-Negami (H-N) functions and $\varepsilon''(\omega)/\varepsilon_{\max}''$ for the Fuoss-Kirkwood (F-K) function, calculated for a relaxation time $\tau = 0{,}001\,s$ and various values of the parameters α, γ and α'.

All of the above mentioned functions may be applied to polymeric systems. The evaluation of the relaxation processes in PSLC polymers will be performed using the equations (4.43), (4.45) and (4.46). The movement of free charges in the sample gives rise to the dc conductivity contribution to the dielectric spectra at low frequencies. Therefore, an additional term should be included in the fit function. Equation 4.47 gives an example for a fitting function containing *k* Havriliak-Negami functions plus conductivity contribution:

$$\varepsilon^*(\omega) - \varepsilon_\infty = \sum_k \frac{\Delta\varepsilon_k}{(1+(i\omega\tau_k)^{\alpha_k})^{\gamma_k}} - \frac{i\sigma}{\varepsilon_0\omega^p} \tag{4.47}$$

For purely ohmic behavior σ denotes the dc conductivity and the exponent p equals one. In some cases, the qualitative description of of $\varepsilon(\omega)$ requires use of p values different from 1.

4.2.2. Dielectric relaxation of rod shaped nematic liquid crystals

The dielectric spectra of liquid crystals depend on the symmetry of the liquid crystalline phase. The dynamics of the molecules is influenced by the intermolecular order. In order to explain the observed dielectric spectra of liquid crystals several theories are proposed. The results from these theories are summarised in Moscicki's work [74]. Here the main equations describing the molecular motion in systems forming a uniaxial liquid crystalline phase with head-tail symmetry (nematic and smectic A) will be presented. The shape of the molecules in this type of systems may be approximated by rods (Figure 4.12). When the system is in its liquid crystalline state, the rods are oriented in one preferred direction $\vec{n}$, called director (see Chapter 2). In order to describe all possible motions of the rod-like molecule in an external electric field, two frames of reference will be introduced: a molecular frame and a laboratory frame (Figure 4.12). The laboratory frame (XYZ) is defined as having Z axis in the direction of the nematic director $\vec{n}$. The molecular frame is fixed to the molecule. Its z-axis is parallel to the long molecular axis. The orientation of the molecule in space is given by the orientation of the molecular frame with respect to the laboratory frame which is defined by set of Eulerian angles $\Omega \equiv \{\alpha, \beta, \gamma\}$ in the following way [74] (Figure 4.12):

–Angle α describes the precession of the long molecular axis about the director (or the *Z*-axis.

–Angle β describes the declination of the long molecular axis from the director.

–Angle γ describes the rotation of the molecule around its long axis.

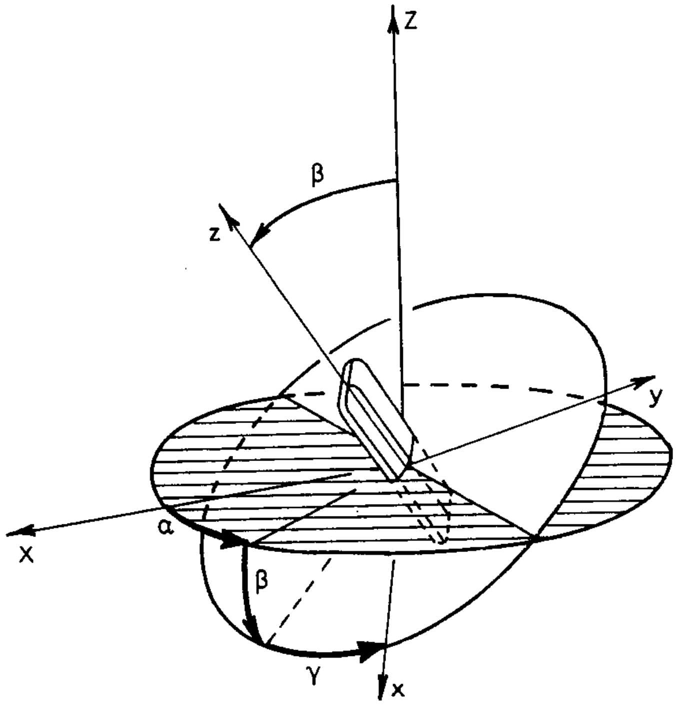

Figure 4.13. Definition of the Euler angles linking the molecular frame (*xyz*) and the laboratory frame (*XYZ*) [74].

Let us assume that the rod-like liquid-crystalline molecule possesses a permanent dipole moment $\vec{u}\,(u_l,\ u_t)$, where u_l is the longitudinal component, parallel to the molecular long axis, and u_t is the transverse component. In order to understand easier the dielectric spectra of multidomain systems (in which every domain has different director) we will regard first a monodomain system, with molecules aligned parallel or perpendicular to the external electrical field. The correlation functions of the projections of $\vec{u}$ on the *Z*- and *X*- axes of the laboratory frame are [74]:

$$u_{//} = u_Z = \sum_{j'=-1}^{1} D^{1*}_{0j'}(\Omega)\, u^{(1,j')}_{mF} \tag{4.48}$$

$$u_{\perp} = u_X = \sum_{j'=-1}^{1} \left[D^{1*}_{-1j'}(\Omega) - D^{1*}_{1j'}(\Omega) \right] u^{(1,j')}_{mF}\ , \tag{4.49}$$

where $u^{(1,j')}_{mF}$ are linear combinations of the components of the dipole moment in the molecular frame

$$u^{(1,0)}_{mF} = u_z\ ; \qquad\qquad u^{(1,\pm1)}_{mF} = \mp(u_x \pm i u_y)/\sqrt{2} \tag{4.50}$$

and

$$D^1_{mk}(\alpha,\beta,\gamma) = e^{-im\alpha} d^1_{mk}(\beta)\, e^{-ik\gamma} \tag{4.51}$$

are the Wigner rotation matrices [87] ($d^1_{mk}(\beta)$ are given in Table 4.1). The Wigner rotation matrices transform the components of the dielectric moment expressed in the molecular frame to their corresponding values in the laboratory frame. The external field is connected to the laboratory frame. Choosing the field direction $\vec{E} \perp \vec{n}$ along the *X*- or *Y*-axis is equivalent, because of the uniaxial symmetry of the system.

m k	-1	0	1
-1	$(1+\cos\beta)/2$	$-\sin\beta/\sqrt{2}$	$(1-\cos\beta)/2$
0	$\sin\beta/\sqrt{2}$	$\cos\beta$	$-\sin\beta/\sqrt{2}$
1	$(1-\cos\beta)/2$	$\sin\beta/\sqrt{2}$	$(1+\cos\beta)/2$

Table 4.1. Wigner rotation matrices $D^1_{mk}(\alpha,\beta,\gamma) = e^{-im\alpha} d^1_{mk}(\beta)\, e^{-iky}$. Explicit forms of $d^1_{mk}(\beta)$ functions [74].

After some calculations, which will be not given here in details, the following results for the dipole-dipole correlation functions are derived [74]:

$$\langle u^*_{//}(0)\, u_{//}(t)\rangle = \frac{1}{3}[(1+2S)\, A_{00}(t) u_l{}^2 + (1-S) A_{01}(t) u_t{}^2] \tag{4.52}$$

$$\langle u^*_{\perp}(0) u_{\perp}(t)\rangle = \frac{1}{3}[(1-S)\, A_{10}(t) u_l{}^2 + (1+\frac{S}{2})\, A_{11}(t) u_t{}^2] \ , \tag{4.53}$$

where

$$A_{00}(t) = a^1_{00}(t) \tag{4.54}$$

$$A_{01}(t) = [a^1_{01}(t) + a^1_{0-1}(t)]/2 \tag{4.55}$$

$$A_{10}(t) = [a^1_{10}(t) + a^1_{-10}(t)]/2 \tag{4.56}$$

$$A_{11} = a^1_{11}(t) + a^1_{1-1}(t) + a^1_{-11}(t) + a^1_{-1-1}(t) \tag{4.57}$$

and $a^1_{lm}(t)$ are the normalized autocorrelation functions of $D^1_{lm}(\Omega)$.

Equations 4.52 and 4.53 show that the contribution of the both components of the permanent dipole moment to the decay of the correlation functions $\langle u_{//}(0)\, u_{//}(t)\rangle$ and $\langle u_{\perp}(0)\, u_{\perp}(t)\rangle$ depend on the order parameter *S*. For completely aligned system, i.e. *S*=1, the correlation function $\langle u_{//}(0)\, u_{//}(t)\rangle$ depends only on u_l, and $\langle u_{\perp}(0)\, u_{\perp}(t)\rangle$ - only on u_t.

For isotropic or not perfectly ordered system both u_l and u_t contribute to the decay of the both correlation functions. Let us regard the contribution of u_l and u_t to the molecular motion in two principle geometries when the electric field is parallel and perpendicular to the director (Figure 4.13). In parallel geometry the dependence of the correlation function $\langle u_{//}(0)\, u_{//}(t)\rangle$ on u_l is given by $A_{00}(t)$ (Eq. 4.54) which is the autocorrelation function of $D^1_{00}(\Omega)$. Since $D^1_{00}(\Omega) = \cos\beta$ (Table 4.1) depends only on the β angle, u_l contributes to $\langle u_{//}(0)\, u_{//}(t)\rangle$ via reorientation of the molecule around the short molecular axes (Figure 4.13). Because of the symmetry of the phase, this motion must be identified with the end-over-end reorientation of the long axis. The contribution of u_t to the $\langle u_{//}(0)\, u_{//}(t)\rangle$, is given by $A_{01}(t)$ (Eq. 4.55), which is a sum of the correlation functions of $D^1_{01}(\Omega)$ and $D^1_{0-1}(\Omega)$. Since $D^1_{01}(\Omega) = -\sin\beta/\sqrt{2}\, e^{-i\gamma}$ and $D^1_{0-1}(\Omega) = \sin\beta/\sqrt{2}\, e^{i\gamma}$ depend only on β and γ, the transverse dipole moment u_t contributes via combined motion of the molecule around the long axis (angle γ) and the short axis (angle β).

Similarly we can identify the motions in perpendicular geometry. The contribution of u_l in $\langle u_{\perp}(0)\, u_{\perp}(t)\rangle$ is described by $A_{10}(t)$ (Eq. 4.56). Since $A_{10}(t)$ is build up by the correlation functions of $D^1_{10}(\Omega)$ and $D^1_{-10}(\Omega)$ ($D^1_{10}(\Omega) = e^{-i\alpha}\sin\beta/\sqrt{2}$); $D^1_{-10}(\Omega) = -e^{i\alpha}\sin\beta/\sqrt{2}$), it describes precession (of angle α) of the long axis about $\vec{n}$ coupled to the reorientation of the molecule around the short axis. Finally, the contribution of u_t to the motion in perpendicular geometry is described by $A_{11}(t)$ (Eq. 4.57), which is a sum of the correlation functions of $D^1_{11}(\Omega)$, $D^1_{1-1}(\Omega)$, $D^1_{-11}(\Omega)$ and $D^1_{-1-1}(\Omega)$.

Since

$$D^1_{11}(\Omega) = e^{-i\alpha}(1+\cos\beta)/2\, e^{-i\gamma},\ D^1_{1-1}(\Omega) = e^{-i\alpha}(1-\cos\beta)/2\, e^{i\gamma};$$

$$D^1_{-11}(\Omega) = e^{i\alpha}(1-\cos\beta)/2\, e^{-i\gamma} \text{ and } D^1_{-1-1}(\Omega) = e^{i\alpha}(1+\cos\beta)/2\, e^{i\gamma},$$

the motion is a combination of reorientation around the short axis (angle β), rotation about the long axis (angle γ), and precession of the long axis around the director $\vec{n}$ (angle α).

The correlation functions (Eq. 4.52 and 4.53) may be expressed as a function of the frequency as [74]:

$$[\varepsilon^*_{//}(\omega) - \varepsilon_{//}(\infty)]/[\varepsilon_{//0} - \varepsilon_{//\infty}] = G_{//}[(1+2S)u_l^{\,2}F^l_{//}(\omega) + (1-S)u_t^{\,2}F^t_{//}(\omega)] \tag{4.58}$$

$$[\varepsilon^*_{\perp}(\omega) - \varepsilon_{\perp}(\infty)]/[\varepsilon_{\perp 0} - \varepsilon_{\perp\infty}] = G_{\perp}[(1-S)u_l^{\,2}F^l_{\perp}(\omega) + (1+S/2)u_t^{\,2}F^t_{\perp}(\omega)], \tag{4.59}$$

where the proportionality factors $G_{//}$ and $G_{\perp}$ account for the polarizability of the sample and incorporate the local field effects.

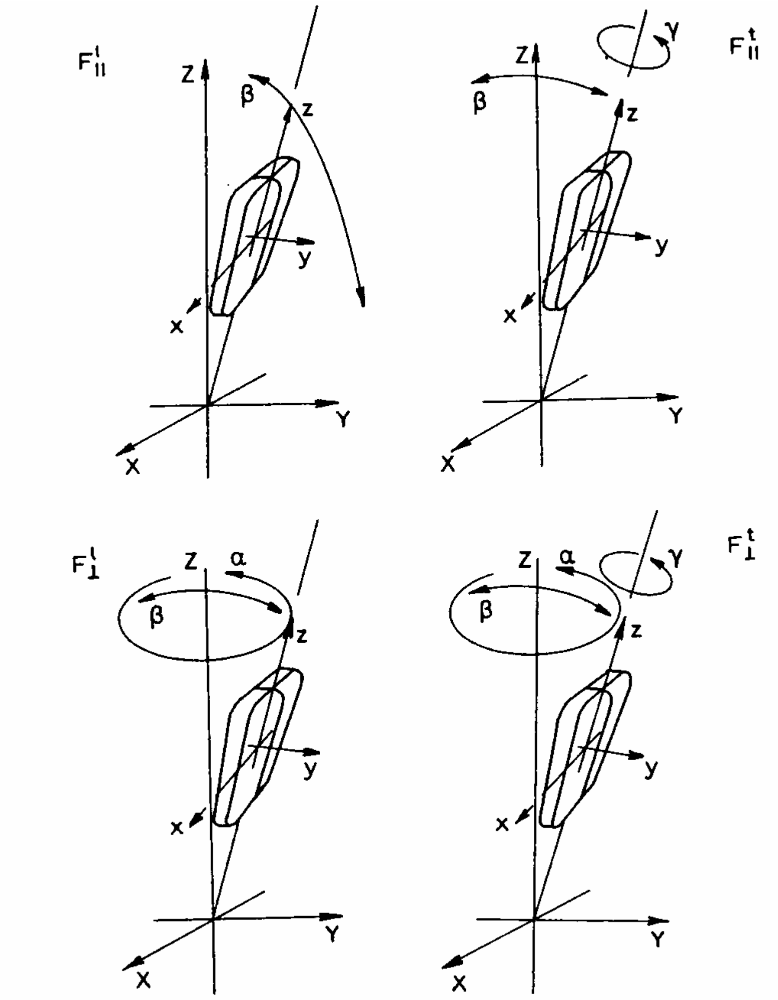

Figure 4.14. A schematic representation of molecular motions involved in the four principal modes of dielectric relaxation in the uniaxial liquid crystal phase [74].

The dielectric relaxation of the mesogens in side-chain liquid crystalline polymers could be described analogically to the regarded molecular dynamics of low molecular liquid crystals. The theory, developed for the low molecular LCs, can still be applied; although the mesogens are bound covalently to the side chain (i.e. the one of the ends is fixed). The main relaxation processes in side-chain LC polymers are denoted in literature [86] as (Figure 4.14):

–δ-relaxation – associated with the reorientation of the side chain around its short axis.

–α-relaxation – arises due to the movement of the main chain segments. The α-relaxation is connected with the glass transition of the sample.

–β-relaxation – associated with the rotation of the mesogen around its long axis.

–γ-relaxation – arises from the spacer mobility when it is connected to a polar group. More detailed explanation of these relaxation processes will be given in Chapter 5.3.

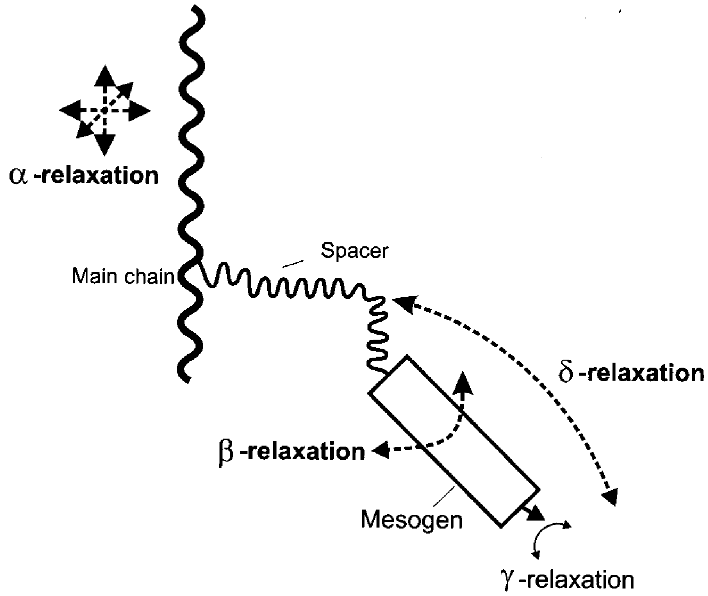

Figure 4.15. Scheme of a SCLC polymer. Possible dielectric relaxation processes are indicated by arrows. The figure is adopted from the book of F. Kremer and A. Schönhals [86].

In addition to these four processes, characteristic for side-chain LC polymers there we will regard a relaxation called the Maxwell-Wagner (MW) polarization. It is observed in heterogeneous systems such as microphase separated block copolymers [88], a phase separated polymer mixture, or mixture of polymer with stabilizers, fillers, dyestuff etc. [89]. It arises due to the accumulation of charges at the interface between two phases having different permittivities and/or conductivities [89, 90]. The complex dielectric function can be written as [86]:

$$\varepsilon^*_{MW}(\omega) = \varepsilon_{MW\infty} + \frac{\Delta\varepsilon_{MW}}{1 + i\omega\tau_{MW}} \tag{4.60}$$

$$\varepsilon'(\omega) = \varepsilon_{MW\infty} + \frac{\Delta\varepsilon_{MW}}{1 + \omega^2\tau_{MW}{}^2} \tag{4.61}$$

$$\varepsilon''(\omega) = \frac{\Delta\varepsilon_{MW}\,\omega\tau_{MW}}{1 + \omega^2\tau_{MW}{}^2} + \frac{\bar{\sigma}}{\varepsilon_0\omega}, \tag{4.62}$$

Van Beek [90] calculated the relaxation time and the conductivity of MW polarization for a layered system:

$$\tau_{MW} = \varepsilon_0 \frac{\varepsilon_1' d_2 + \varepsilon_2' d_1}{\sigma_1 d_2 + \sigma_2 d_1} \tag{4.63}$$

$$\bar{\sigma} = \frac{d\, \sigma_1 \sigma_2}{\sigma_1 d_2 + \sigma_2 d_1} \tag{4.64}$$

where ε_1' and σ_1 are the permittivity and the conductivity of the first layer; ε_2' and σ_2 are the permittivity and the conductivity of the second layer; d_1 and d_2 are the thicknesses of the first and the second layer and $d = d_1 + d_2$.

4.2.3. Measurement technique

Low frequency equipment

Figure 4.15 shows a scheme of a frequency response analyser– an equipment for dielectric measurements in low frequency interval – 10^{-2}-4.10^{5} Hz [91, 92]. The sample is placed in the plate capacitor. The impedance of the capacitor is measured with the help of Schlumberger's Impedanceanalyser SI-1260 (Figure 4.15). The integral generator of frequency generates sinusoidal voltage $V_1=V_1^0\sin(\omega t)$ – the in-phase signal, which is measured before passing the sample and one reference signal, shifted on 90°. Passing through the sample, the initial sinusoidal signal changes its phase and amplitude:

$$V_2=V_2^0\sin(\omega t+\delta) \tag{4.65}$$

The shifted signal is multiplied in the correlator with the in-phase signal, and after that integrated by a given number N of cycles with period T. At the same time it is multiplied with the 90° shifted signal and the result is integrated using the same procedure:

$$V_2' = \frac{2}{NT} \cdot \int_0^{NT} V_2^0 \sin(\omega t + \delta) \sin(\omega t) . dt = V_2^0 \cos\delta \tag{4.66}$$

$$V_2'' = \frac{2}{NT} \cdot \int_0^{NT} V_2^0 \sin(\omega t + \delta) \cos(\omega t) . dt = V_2^0 \sin\delta \tag{4.67}$$

V_2' and V_2'' are the real in the imaginary part of the complex voltage V_2*:

$$V_2^* = V_2' + iV_2'' = V_2^0 \cos\delta + V_2^0 \sin\delta = V_2^0 \exp(i\delta) \tag{4.68}$$

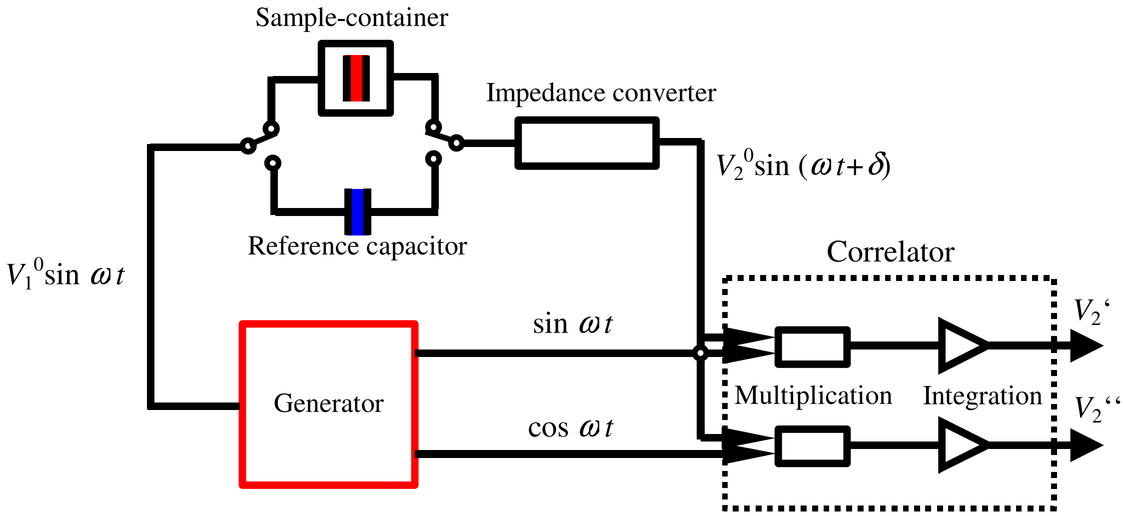

Figure 4.16. Scheme of Schlumberger's Impedanceanalyser SI-1260 [91, 92].

In order to improve the measurement in the low frequency interval between the sample and the correlator is connected Chelsea impedance converter. It corrects the errors in the displacement current which occurs due to the high input resistance of the correlator. In order to make the corrections, a reference capacitor with known characteristics is measured. The admittance of the sample Y_S and of the reference capacitor Y_R can be expressed as [92]:

$$Y_S = -g_S(\varphi).Y_m^S.\frac{V_2^S}{V_1^S} \tag{4.69}$$

$$Y_R = -g_R(\varphi).Y_m^R.\frac{V_2^R}{V_1^R} \tag{4.70}$$

where $Y_m^{S,R}$ is the admittance of the feed back path and $g_{S,R}(\varphi)$ is the error in the phase inserted by the different parts of the frequency analyser.

When the measured voltages have similar values, i.e. $V_2^R \sim V_2^S$, the errors in the phase are also similar, i.e $g_S(\varphi) \sim g_R(\varphi)$. Moreover, $Y_m^R = Y_m^S$. Hence, dividing equation 4.69 to equation 4.70, we obtain

$$Y_S = Y_R \frac{V_2^S}{V_1^S}\frac{V_1^R}{V_2^R} \tag{4.71}$$

If we neglect the inductivity of the sample and the reference capacitor, and the resistance of the latter, then

$$Y_R = i\omega C_R \tag{4.72}$$

$$Y_S = G_S + i\omega C_S \tag{4.73}$$

where G_S is the conductivity of the sample, C_S is the capacity of the sample capacitor, and C_R is the capacity of the reference capacitor.

$$Y_S = i\omega C_R \left[\mathrm{Re}\left[\frac{V_2^S}{V_1^S} \frac{V_1^R}{V_2^R} \right] + \mathrm{Im}\left[\frac{V_2^S}{V_1^S} \frac{V_1^R}{V_2^R} \right] \right]. \tag{4.74}$$

Therefore

$$\mathrm{Re}[Y_S] = G_S = -\omega C_R . \mathrm{Im}\left[\frac{V_2^S}{V_1^S} \frac{V_1^R}{V_2^R} \right] \tag{4.75}$$

$$\mathrm{Im}[Y_S] = \omega C_S = \omega C_R \,\mathrm{Re}\left[\frac{V_2^S}{V_1^S} \frac{V_1^R}{V_2^R} \right] \tag{4.76}$$

$$\tan\delta = \frac{\mathrm{Re}[Y_S]}{\mathrm{Im}[Y_S]} = -\frac{\mathrm{Im}\left[\frac{V_2^S}{V_1^S} \frac{V_1^R}{V_2^R} \right]}{\mathrm{Re}\left[\frac{V_2^S}{V_1^S} \frac{V_1^R}{V_2^R} \right]} \tag{4.77}$$

The measured voltages V_1^S, V_2^S, V_1^R and V_2^R can be connected with the complex permittivity in the following way.

The capacity C_S of a capacitor, filled with dielectric with a complex permittivity $\varepsilon^*(\omega)$ is:

$$C_S = \varepsilon^*(\omega).\varepsilon_0.\frac{A}{d} = \varepsilon^*(\omega).C_0, \tag{4.78}$$

Where A is the area of the capacitor plates, d is the distance between them and C_0 is the capacity of the empty capacitor.

The current in the capacitor can be represented as a sum of the conductivity current and displacement current. The point of interest for the dielectric measurement is the displacement current I_d*, which is a result of the charge displacement in a dielectric media.

$$I_d^* = A.\frac{\partial D^*}{\partial t} \tag{4.79}$$

Using Eq. 4.34 one obtains

$$I_d^* = A.\varepsilon^*(\omega).\varepsilon_0.i\omega E^* \tag{4.80}$$

Keeping in mind that $E^* = \frac{V^*}{d}$, the displacement current I_d* can be expressed as:

$$I_d^* = A.\varepsilon^*(\omega).\varepsilon_0.i\omega\frac{V^*}{d} \tag{4.81}$$

Then, the admittance of the sample is determined as:

$$Y_S = \frac{I_d^*}{V^*} = i\omega\varepsilon^*(\omega).C_0 = i\omega(\varepsilon'(\omega) - i\varepsilon''(\omega)).C_0 \qquad (4.82)$$

$$\mathrm{Re}[Y_S] = \omega\varepsilon''(\omega).C_0 \qquad (4.83)$$

$$\mathrm{Im}[Y_S] = \omega\varepsilon'(\omega).C_0 \qquad (4.84)$$

Comparing Eq.4.83 and 4.84 with the Eq.4.75 and 4.76, we obtain the following expressions for $\varepsilon'(\omega)$, $\varepsilon''(\omega)$ and tan δ:

$$\varepsilon'(\omega) = \frac{C_R}{C_0}\mathrm{Re}\left(\frac{V_2^S}{V_1^S}.\frac{V_1^R}{V_2^R}\right) \qquad (4.85)$$

$$\varepsilon''(\omega) = -\frac{C_R}{C_0}\mathrm{Im}\left(\frac{V_2^S}{V_1^S}.\frac{V_1^R}{V_2^R}\right) \qquad (4.86)$$

$$\tan\delta(\omega) = \frac{\varepsilon''(\omega)}{\varepsilon'(\omega)} = -\frac{\mathrm{Im}\left(\frac{V_2^S}{V_1^S}.\frac{V_1^R}{V_2^R}\right)}{\mathrm{Re}\left(\frac{V_2^S}{V_1^S}.\frac{V_1^R}{V_2^R}\right)} \qquad (4.87)$$

The capacity C_R is known, the capacity C_0 can be calculated after measuring the A and d values and the voltages V_1^S, V_2^S, V_1^R and V_2^R can be measured with the impedance analyser.

The sketch of the sample container, used in this equipment is given on Figure 4.16.

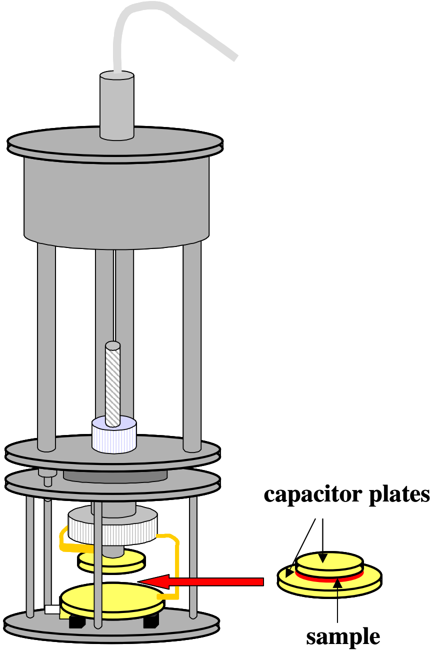

Figure 4.17. A sample container used in the frequency response analyser.

The sample capacitor consists of two gold-coated stainless steel electrodes. It is filled with the polymer at 150^0C. Glass fibres put between the two capacitor plates insure uniform distance between them. The sample thickness is 0.05-0.1 mm. The temperature is regulated by floating the sample container with liquid nitrogen and heating the capacitor at the same time. The sample temperature, measured (at a distance < 1mm) with the help of a platinum resister (Pt 100) by use of four-wire technique, shows stability better than 0.05°C.

High frequency equipment

The frequency response analyser can not be used at high frequencies because of the scattering capacities and contact resistance. The frequency interval of $1.10^6 - 2.10^8$ Hz can be explored with the help of the coaxial line reflectometer Hewlett-Packard 4191A [91] (Figure 4.17). It has a coaxial cylindrical waveguide with circular cross section. The outer cylinder is grounded. The inner conductor transports the electrical signals.

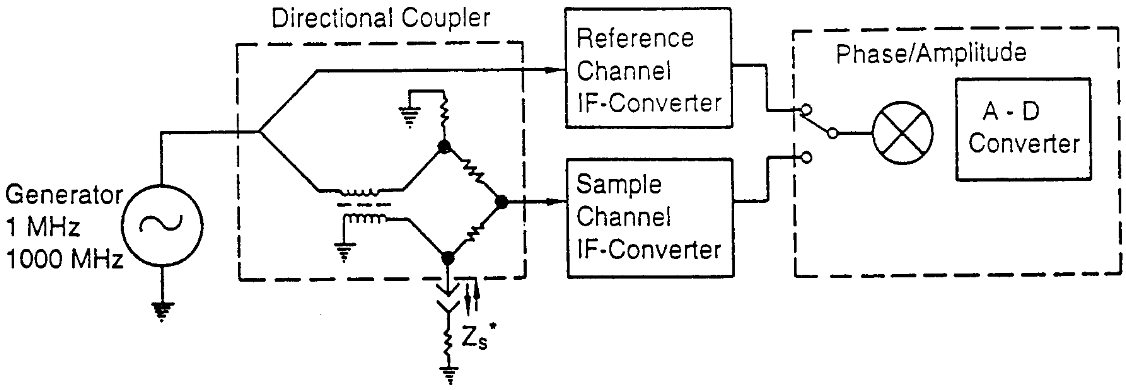

Figure 4.18. Scheme of a Coaxial line reflectometer Hewlett-Packard 4191A [91].

The frequency generator generates sinusoidal voltage, which is then split to a reference signal and a voltage passing through the sample. The waveguide with the sample capacitor is connected to the circuit on the one side of the bridge. The signal is reflected by the sample. The complex reflection coefficient Γ* is proportional to the quotient of the output and input voltages in the bridge. The output signal is lead to a vector voltmeter by the use of a directional coupler where it is compared with the signal from a reference channel. Thus the complex reflection coefficient is measured:

$$\Gamma^* = \frac{V_S^*}{V_R^*} \tag{4.88}$$

where V_S * is the reflected signal and V_R * is the reference signal (which are different from these in the previous discussion).

On the other hand

$$\Gamma^* = \frac{Z_S * - Z_0}{Z_S * + Z_0} \tag{4.89}$$

where Z_0 is the impedance of the waveguide and Z_S* is the impedance of the sample. $Z_0 = \sqrt{\frac{L}{C}}$, there L is the inductivity and C is the capacity of the waveguide.

Using Eq. 4.88 and 4.89 one obtains for the complex impedance of the sample Z_S^* the following equation:

$$Z_S^* = Z_0 \frac{1+\Gamma^*}{1-\Gamma^*} = Z_0 \frac{1+\frac{V_S *}{V_R *}}{1-\frac{V_S *}{V_R *}} \tag{4.90}$$

The impedance is connected to the admittance reciprocally:

$$Z_S * = \frac{V}{I} = \frac{1}{Y_S *} \tag{4.91}$$

Hence one can write:

$$Y_S * = \frac{1}{Z_0} \frac{1-\frac{V_S *}{V_R *}}{1+\frac{V_S *}{V_R *}} \tag{4.92}$$

Comparing this equation with Eq. 4.83 and 4.84, we obtain:

$$\varepsilon''(\omega) = \frac{1}{\omega C_0} \mathrm{Re}\left[\frac{1}{Z_0} \frac{1-\frac{V_S *}{V_R *}}{1+\frac{V_S *}{V_R *}}\right] \tag{4.93}$$

$$\varepsilon'(\omega) = \frac{1}{\omega C_0} \mathrm{Im}\left[\frac{1}{Z_0} \frac{1-\frac{V_S *}{V_R *}}{1+\frac{V_S *}{V_R *}}\right] \tag{4.94}$$

$$\tan\delta = \frac{\mathrm{Re}\left[\dfrac{1}{Z_0}\dfrac{1-\dfrac{V_S *}{V_R *}}{1+\dfrac{V_S *}{V_R *}}\right]}{\mathrm{Im}\left[\dfrac{1}{Z_0}\dfrac{1-\dfrac{V_S *}{V_R *}}{1+\dfrac{V_S *}{V_R *}}\right]} \tag{4.95}$$

All values in the last three expressions can be measured or calculated.

4.3. Materials – synthesis and chemical characterisation

The investigated series of PSLC block copolymers consists of two blocks– polystyrene (PS) and side-chain liquid crystalline (LC) ones. The volume fraction of the LC block ϕ_{LC} varies systematicaly, which results in variation of block copolymer morphology– from PS domains in LC matrix at high ϕ_{LC} through layered structure (lamellae) at intermediate ϕ_{LC} to LC domains in PS matrix at low ϕ_{LC}.

The PSLC block copolymers were synthesized at the Institute for Macromolecular Chemistry, Freiburg University [70]. The polymers are denoted as PSLC x/y where x is the content of PS block in volume percent and y is the content of LC block. The method of synthesis is called a modified three-step technique. This method was developed by Gronski et al. [94]. The isotropic polystyrene block was attached to the liquid crystalline block, which consists of cyanobiphenyl mesogens coupled to poly(1,2-butadiene) through valeric acid spacers (Figure 4.18). In the first step of synthesis, polystyrene-b-poly (1,2-butadiene) precursor block copolymers (PSPB) with strictly defined molecular weight and block volume ratios were synthesized through living anionic polymerization. In the second step, the vinyl 1,2-double bonds of the PB block of the precursor copolymers were converted into OH-groups (this intermediate product polymer is denoted as PSOH in Figure 4.18) through hydroboration with 9-BBN. The mesogen unit was prepared by coupling of the cyanobiphenyl mesogen to a valeric acid spacer by etherification. In the third step, the mesogen unit was inserted in the PSOH block copolymers through esterification of the OH-groups with the activated mesogenic groups. The excess of unbound mesogen units, which can severely disturb the dielectric experiments, was removed from the product by a novel combination of dialysis column chromatography and continuous extraction in various solvents depending on the solubility of the corresponding block copolymers. The method of size exclusion chromatography (SEC) proved that after the purification, the PSLC block copolymers does not content any low molecular weight impurities. Modification of the synthesizing technique was necessary because of the difficulties posed by its earlier variant in attaining polymers with strictly defined molecular weight, termination of the polymerization without side-reactions and purification of the solvent under the given conditions. A particular problem was encountered for block copolymers with extremely asymmetric composition concerning their solubility and solubility changes during the second and third step of synthesis. This problem was solved through an improvement of the method of synthesis, modification of the apparatus, novel terminating method, and modified control of the solvent polarity during the reaction and use of various solvent combinations.

The PSLC diblock copolymers were characterized using SEC for determination of the molecular weight and ^{1}H Nuclear magnetic resonance (^{1}H-NMR) for determination of the composition of the PSPB block copolymers (data are shown in Table 4.2). Fourier transformed infrared spectroscopy (FTIR) and ^{1}H-NMR proved that both polymer analogous reactions (step two and step three) proceed with 100% conversion and without side reactions. The molecular weight of the PSLC block copolymers is in the range 38000 – 125000 and has a polydispersity close to 1 ($M_w/M_n = 1.03 - 1.10$).

The block weight fractions are calculated stoichiometrically assuming that a 100% conversion of the precursor block copolymers into the end-products takes place. The block volume fractions are calculated from the corresponding weight fractions using the density of the PS block (1.04 g/cm^3) and that of the LC block (1.25 g/cm^3). Furthermore, we have performed an additional determination of the composition of the synthesized PSLC block copolymers using ^{1}H-NMR [80]. As Table 1 demonstrates, the experimentally obtained N_{LC}/N_{PS} values agree well with the calculated ones within 2% to 10%, with the exception of the block copolymer with the highest PS content. These results confirm the absence of low-molecular weight impurities (e.g., unbound mesogen units). The larger error in the case of the block copolymers with the most asymmetric compositions and the inability to measure the block copolymer with the lowest PS content are attributed to the poor solubility of the two blocks in the one and the same solvent. Since the method was not optimal for all studied block copolymers, we have further used the calculated composition values.

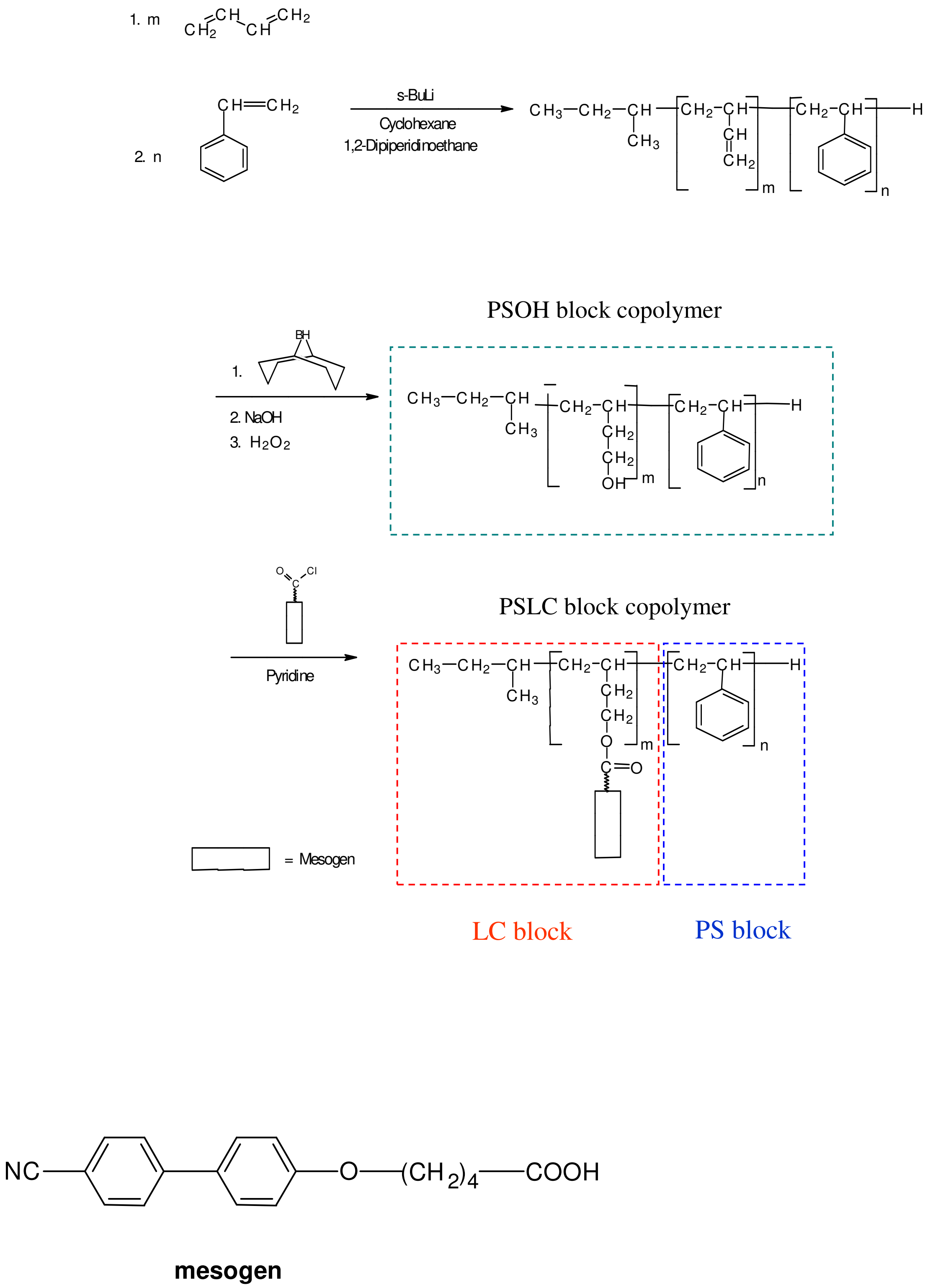

Figure 4.18. Route of synthesis of PSLC block copolymers [70].

Table 4.2. Chemical characteristics of the synthesised PSLC block copolymers. The values of PC and LC weight fractions are calculated stoichiometrically on the base of 100% convertion. The volume fractions were calculated from the corresponding weight fractions using the mass density of the PS block 1.04 g/cm^3 and of the LC block– 1.25 g/cm^3 [80].

PSLC block copolymer	M_w	N_{PS}	N_{LC}	PS wt.%	LC wt.%	N_{LC}/N_{PS}	N_{LC}/N_{PS}	PS vol%	LC vol%
				calculated		calculated	measured	calculated	
PSLC 7/93	77 000	42	208	5.7	94.3	4.95	a	6.8	93.2
PSLC 14/86	53 700	58	133	11.5	88.5	2.29	2.25	13.5	86.5
PSLC 19/81	104 300	163	250	16.3	83.7	1.53	b	19.0	81.0
PSLC 30/70	98 700	243	207	25.9	74.1	0.8518	b	29.6	70.4
PSLC 39/61	55 000	175	99	34.5	65.5	0.5657	0.553	38.8	61.2
PSLC 59/41	38 000	200	50	54.4	45.6	0.25	0.225	58.9	41.1
PSLC 77/23	62 800	444	48	73.4	26.6	0.1081	0.102	76.8	23.2
PSLC 85/15	86 500	662	42	82.5	17.5	0.0634	0.059	85	15.0
PSLC 97/3	125 000	1167	11	96.9	3.1	0.0094	0.014	97.4	2.6

[a] It was not possible to perform a measurement in the same solvent as the other block copolymer

[b] Measurements were not carried out

5. Results and discussion

5.1. LC mesophase– thermotropic behaviour

The thermotropic behaviour of the LC block was probed by Differential Scanning Calorimetry (DSC) and Polarized Optical Microscopy (POM).

Figure 5.1 shows DSC thermograms for the samples PSLC 7/93, PSLC 59/41, PSLC 77/23 and PSLC 85/15. It is seen that the DSC curves for PSLC 59/41, PSLC 77/23 and PSLC 85/15 show two transition steps and one peak, which corresponds to the glass transition of the LC block (at T_{gLC}~35°C), the glass transition of polystyrene (T_{gPS}~100°C) and the nematic-to-isotropic transition of the LC block (T_i~118-124°C). The two T_g's, corresponding to the glass transition of each block, are well separated confirming the existence of a microphase separation of the PS and LC blocks. The data, extracted from the DSC thermograms for all PSLC block copolymers are presented in Table 5.1. The glass transition temperature T_{gPS} of PS was not detected for PSLC polymers with PS volume fraction up to 0.3, because the total mass of PS examined was too small. The glass transition of LC block T_{gLC} and the nematic-to-isotropic transition temperature T_i for the polymer PSLC 97/3 (the sample with the lowest LC volume fraction) were not detected for the same reason.

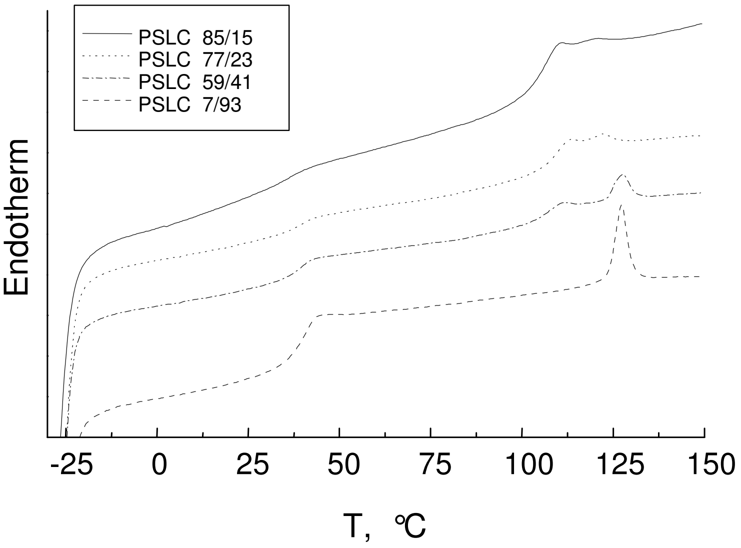

Figure 5.1. DSC measurements for selected PSLC block copolymers where each was recorded at a heating rate of 10 °C/min.

The POM studies of the PSLC block copolymers at various temperatures were performed using an Olympus 41 optical microscope (at a magnification 100x and 200x) equipped with a Linkam heating stage and an Eurotherm temperature controller, which provides a control precision of ±0.1 °C. The observations show that all samples are birefringent below the T_i, i.e. they exhibit LC order. Images at a higher magnification (500x) were recorded at room temperature with an Olympus BX 51 polarization optical microscope.

Table 5.1. Transition temperatures of the investigated copolymers.

Polymer	$T_{g\ PS}$, [°C]	$T_{g\ LC}$, [°C]	$T_{i\ DSC}$, [°C]	$T_{iPOM,}$ [°C]
LC homopolymer	-	33.5	112.1	121.5^h (117.5^c)
PSLC 7/93	-	32.0	116.1	121.5
PSLC 14/86	-	35.4	116.9	121.5
PSLC 19/81	-	36.9	116.7	121.5
PSLC 30/70	104.3	33.3	117.1	124-126
PSLC 39/61	102.2	35.1	117.9	125-127
PSLC 59/41	104.0	35.6	121	121-123
PSLC 77/23	106.1	35.7	116	113-118
PSLC 85/15	106.7	-	115	113-118
PSLC 97/3	108.9	-	-	-

Figure 5.2 shows the polarization microscopy at a magnification of 500x of LC homopolymer at room temperature obtained using cross polarizers. In this case, the sample was placed between thin glass plates, heated on a hot plate above T_{gPS} and T_i and pressed by cooling, in order to reduce the film thickness. Reducing the film thickness was necessary in order to obtain a good picture. However, the applied pressure may have introduced a certain orientation within the film. The image in Figure 5.2 contains coloured birefringent regions divided by black lines. The latter correspond most probably to the isotropic regions on the border between domains with different directors. The image differs from the usual “schlieren texture” [95] of small molecular nematic LC. However, it is similar to pictures of nematic LC polymers found in literature [96, 97].

The results for the nematic-to-isotropic transition temperature T_i obtained from the POM experiments are presented in Table 5.1. The study of the LC homopolymer shows that the temperature of the nematic-to-isotropic transition T_i^h (about 121°C) is not equal to the isotropic-to-nematic transition temperature T_i^c (about 117°C). This hysteresis effect is known as supercooling and is similar to the supercooling effect in concentrated solutions. Similar results were obtained by Schnurpfeil *et* al. [96] for low-molecular nematic liquid crystalline diepoxides. In the case of PSLC block copolymers, T_i^h=T_i^c, i.e. the two temperatures coincide. Probable explanation of this result is that in LC polymer the nucleation is homogeneous, which requires supercooling, while in the PSLC polymers nucleation is heterogeneous due to the presence of the PS block.

The difference between the isotropisation temperature T_i measured by DSC and POM (see Table 5.1) can be explained by the different working principles of both methods. The DSC isotropisation temperature is obtained by taking the onset value of the corresponding peak. This implies the onset temperature of the isotropisation process at which the first domains undergo a nematic-to-isotropic transition. The POM method accounts for the end temperature of the isotropisation process, i.e. the isotropisation is complete within the entire volume.

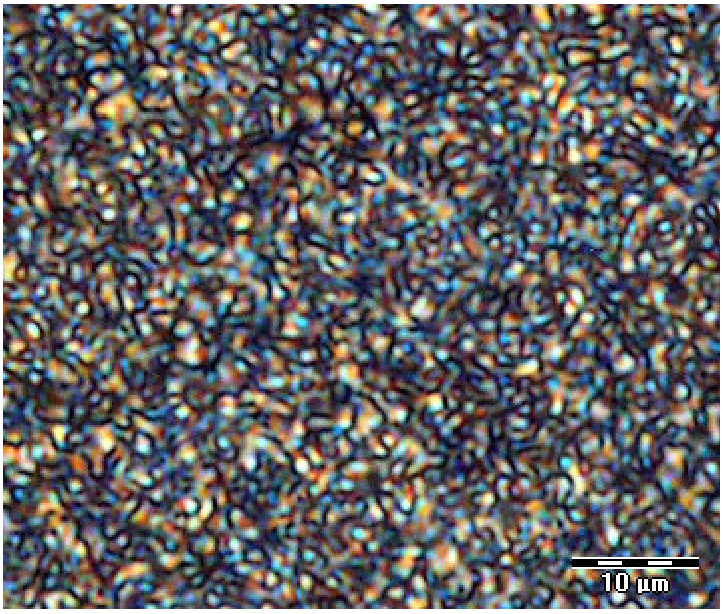

Figure 5.2. Polarized Optical Microscopy of the LC homopolymer at room temperature

The presence of nematic LC order is confirmed by SAXS and WAXD experiments (see below). The WAXD scattering curves show a peak, corresponding to the mean distance between the mesogens. The SAXS curves do not show peaks rising from any additional order of the mesogens (such as smectic reflection observed for similar mesogens at

q~1.5 nm^{-1} [72]). Therefore, one can conclude that the order within the LC mesogens is nematic. Using WAXD experiments Sänger and Gronski also found nematic order in PS-LC-PS triblock copolymer with the same structure of the LC block [94], like in the polymers investigated in this thesis.

The nematic-to-isotropic transition temperature T_i can be roughly estimated using dielectric spectroscopy data by following the variation of the relaxation strength with temperature.

Figure 5.3 shows the variation of the relaxation strength of the δ-process with temperature (see Chapters 4.2 and 5.3). The relaxation strength is extracted after fitting the dielectric spectra with a Havriliak-Negami function (see Chapter 5.3). The δ-process corresponds to the movement of the side-chain as a whole. Therefore its relaxation strength is strongly influenced by the LC order. In this work, the dielectric strength for all samples studied changes after the nematic-to-isotropic transition; it increases for some of the samples, while decreasing for others. This behaviour depends on the orientation of the mesogens with respect to the capacitor plates. An orientation might be introduced by pressing of the sample between both capacitor plates at temperatures above T_gLC and $T_\mathrm{i.}$ The nematic-to-isotropic transition temperature can be only roughly estimate from the dielectric spectra, because the transition is much broader in comparison with the nematic-to-isotropic transition interval, observed by POM. The DS may also detect minute changes, which are too small to be discerned with POM.

Figure 5.3 shows that the nematic-to-isotropic transition interval broadens with increasing the PS volume fraction. The relaxation strength for the sample PSLC 85/15, which is not shown in the

Figure **5.3** changes continuously and a transition interval cannot be estimated by this method at all. The relaxation strength is proportional to the number of relaxing dipoles. This decreases with decreasing of the LC volume fraction as expected.

The mesophase behaviour of LC block depends on backbone properties such as flexibility (more rigid backbones give less ordered mesogenic units [98]), length and tacticity, as well as on mesogen attributes including shape, chirality, polarity, or how the mesogens are incorporated into the polymer [36, 99]. An important parameter is also the length of the spacer, which connects the mesogen to the backbone. Usually, short spacers with four or five methylene groups lead to a nematic phase while longer spacers result in smectic phases [94, 100, 101]. Zaschke *et* al. suggest that the LC mesophase depends on the

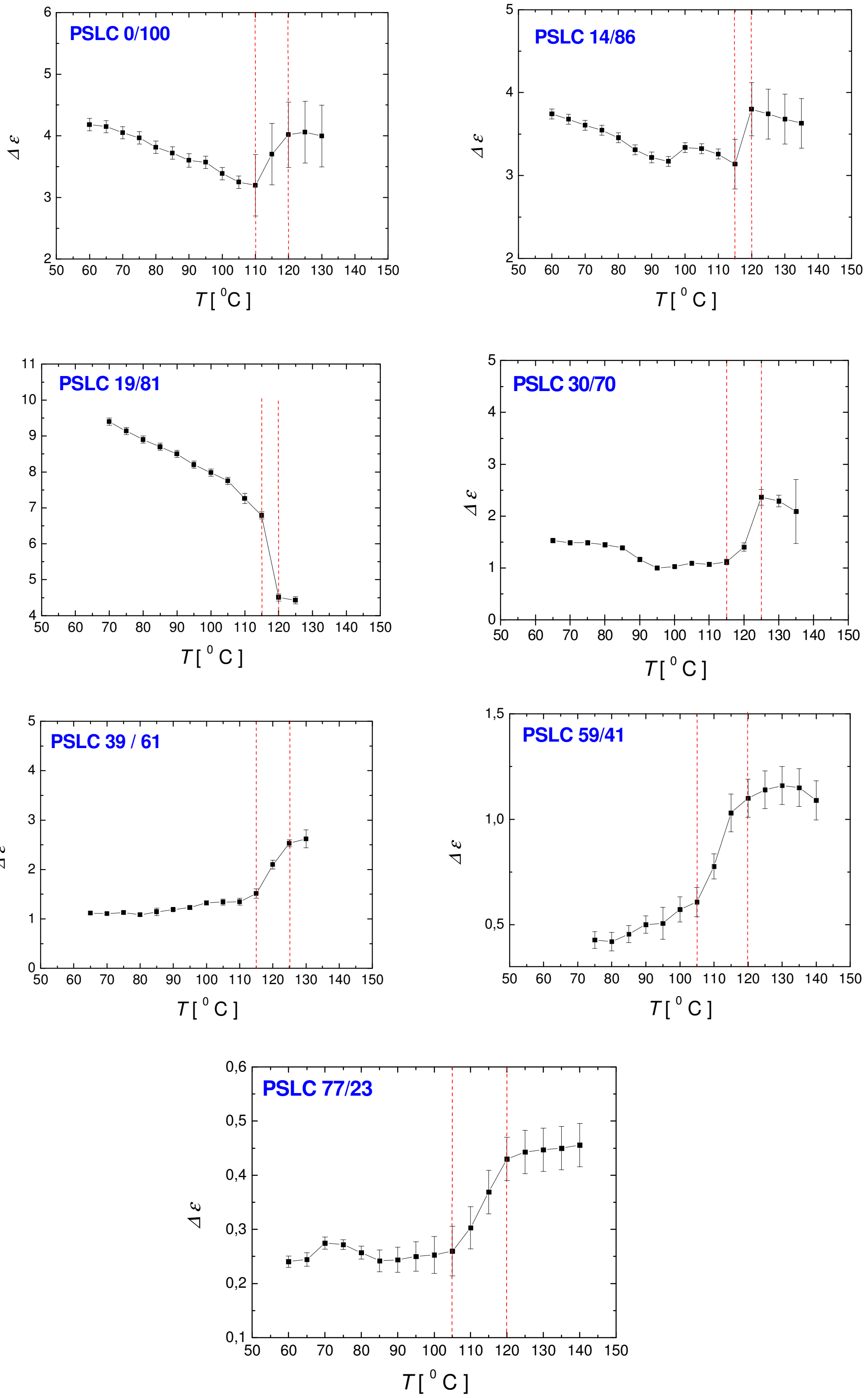

Figure 5.3. The relaxation strength $\Delta\varepsilon$ of PSLC block copolymers vs. temperature. The plots of PSLC 7/93 and PSLC 85/15 are not shown because it was not possible to reasonably divide the δ- and α- processes at high temperatures.

type of the amorphous block [102]. However, their results are not very clear, because the conversion obtained after synthesis varies in the interval of 50-100% and the LC behaviour in this report may be influenced by small molecule impurities still present after synthesis.

The nematic-to-isotropic transition temperature T_i of the liquid crystal block is found to depend on its molecular weight [103]. The T_i for the investigated in [103] SCLC/PMMA and SCLC/PS diblock copolymers increases from 115°C for $\overline{M_n} = 6.10^3$ up to 140° for $\overline{M_n} = 6.10^4$ and then remains nearly constant. T_i does not depend on the type or length of the amorphous block. A similar tendency was found also for smectic LC block copolymers. Yamada et al. have shown that with increasing the molecular weight of the LC block up to about 15 000, isotropisation temperature increases. Also, T_i remains constant with further increasing of the molecular weight [99, 104]. Laus *et* al. [105] report completely opposite results to these in [103], i.e. that T_i depends on the length of the amorphous block. They found, that for poly-(vinyl ether) smectic block copolymers T_i decreases with increasing the non-LC vinyl ether block content.

The dependence of T_i on the structure is quite complicated. It has been observed that the same type of morphology in some cases stabilizes the LC phase and in other cases destabilizes it. Most of the studies in this area are about LC/I block copolymers with the LC block forming a smectic phase. For chiral side-chain liquid crystalline diblock copolymers with low to moderate molecular weight, Zheng and Hammond [34] determined that the lamellar domains stabilize the layered smectic mesophase (particularly smectic C* phase over the smectic A and nematic LC phases). The smectic C* phase is particularly favoured at higher molecular weight and longer PS chain lengths. The reason suggested by them is that the increasing molecular weight leads to microphase separation with sharper interfaces. In low molecular weight block copolymers (M_n~18 000) with a high LC content (43 wt%) the order-disorder transition coincides with the LC isotropisation temperature.

The stabilization effect of lamellae phase on the smectic A mesophase also was observed by Fischer at al. [40] in polystyrene-polymethactylate cholesteryl based LC blocks. They found that the stabilization is independent of the molecular weight of the smectic block and specific morphology of the block copolymer. In many cases the presence of the interface stabilizes the smectic phase, i.e. the T_i of LC in block copolymers is higher than that of the LC homopolymer. Mao *et* al. have observed stabilization of the smectic phase for cylindrical morphology, but destabilization in a lamellar morphology [38]. Yamada *et* al. [104] demonstrated that the smectic phase in the cylindrical domain is more stable in comparison with that found in the lamellar domain. Bohnert and Finkelmann [103] did not find any stabilization effects for nematic LC block copolymers.

Figure 5.4 shows the dependence of T_i (measured by POM) on the molecular weight of the LC block. Although the scattering of the data is quite high, one can see a similar tendency of this effect, found in [103] for the nematic LC phase and in [99] and [104] for the smectic LC phase. T_i increases up to the certain molecular weight (in this case M_w ~ 15580) and then does not show any systematic dependence on M_w.

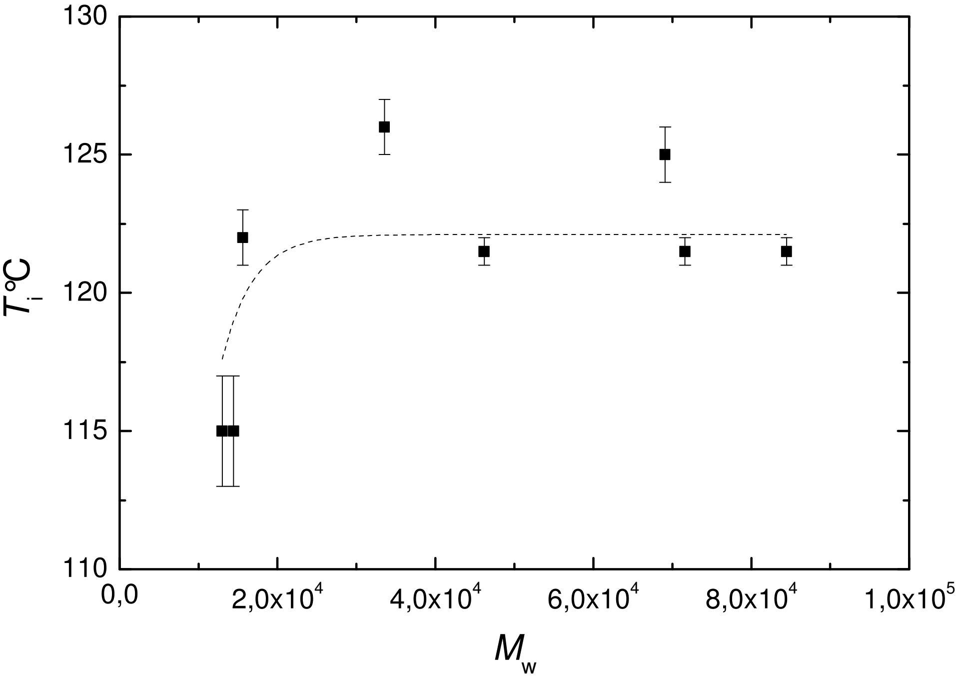

Figure 5.4. The dependence of T_i on the molecular weignt M_w of the LC block. The line is drawn to guide the eyes.

The data for T_i obtained from the different methods do not result in a unique dependence of T_i on volume fraction or domain form. In particular, the POM measurements were performed in heating and cooling cycles and a supercooling effect with a temperature difference about 4°C was observed in the pure LC polymer. It disappeared completely for the PSLC block copolymers – even for the sample with the lowest PS volume fraction (ϕ_{PS} ~0.07).

Wide angle X-ray diffraction (WAXD) results

Wide angle X-ray diffraction (WAXD) provides information about the interchain and intrachain correlation distances in amorphous polymers. In addition, the WAXD data for a liquid crystalline polymer should reveal a peak, corresponding to the average distance between the oriented mesogen units (i.e. the intermesogen distance).

Figure 5.5 shows WAXD profiles for LC and PS homopolymers at room temperature. The PS scattering profile is in agreement with data in literature [78, 106]. The data are fitted using three Lorentz functions with maximum values at q=7.1±0.07 nm^{-1}; 13.61±0.04 nm^{-1} and 28.3±1 nm^{-1}. The lower intensity peak at q=7.15 nm^{-1} is called polymerization peak [78] or polymerization ring [106] (in the two dimensional diffraction patterns), because it is completely absent in the scattering pattern of the styrene monomer. Studying of the oriented sample shows that this peak corresponds directly to the interchain correlation [106]. The X-ray diffraction patterns of the most amorphous polymers do not show such a peak. This difference occurs due to the particular chemical structure of polystyrene. The phenyl rings, which belong to neighbouring molecules, organize in stacks. X-ray diffraction of these stacks gives rise to the polymerization peak. The other peaks at higher angles represent both inter as well as intrachain correlations.

The LC scattering profile (Figure 5.5) does not have a polymerization peak at q~7 nm^{-1}. One can see only a small hump at q~5-6 nm^{-1}, which will be ignored in this study. The scattering curve shows two broad features. The fit of the first feature performed by use of two Lorentz functions gives better results than the fit performed using only one Lorentz function. The corresponding maximum's positions are at q_1=14.3±0.1 nm^{-1} and q_2=16.4±0.51 nm^{-1}. The third peak was as well fitted by the Lorentz function with a maximum at q_3=30±1 nm^{-1}~$2\left[\frac{q_1+q_2}{2}\right]$. The first peak at q_1=14.3 nm^{-1} is connected to the nematic order in the side-chains. The second peak, broader and much less pronounced corresponds to "pure" carbon-carbon correlations. The intermesogen distance d_N is given by $2\pi/q_1$, i.e. d_N = 0.44±0.005 nm. This agrees well with the values in literature for similar biphenyl mesogens [37, 72, 99, 107, 108].

Figure 5.6 shows the wide angle scattering profiles of the PSLC block copolymers (Table 4.2). The most intense peak (at q~14 nm^{-1}) is a superposition of the second PS peak and the first and second LC peaks. It was impossible to separate the three components by the fitting procedure. The fit was performed by use of one Lorentz function. The fit results about the position of the maximum are presented in Figure 5.7. One can clearly see that the most intense peak of the PSLC block copolymers shows a tendency to move to lower *q* values with increasing the PS volume fraction ϕ_{PS} (i.e. decreasing LC volume fraction). The *q* value remains constant within the experimental error only for the interval with ϕ_{PS} ~0.4–0.6 (i.e. around PS/LC composition 50/50).

Another feature, which changes with the composition is the polymerization peak at q~7 nm^{-1}. The intensity of the polymerization peak decreases with decreasing the PS volume fraction; the peak disappears at PSLC 59/41, and finally converts into a hump at the block copolymers with lower PS (higher LC) content. These two tendencies indicate a continuous conversion of the scattering profiles of the PSLC block copolymers from those of the PS homopolymer to those of the LC homopolymers with decreasing the PS content.

The initial idea of the measurements was to follow the change of the distance between the mesogens d_N with increasing the PS volume fraction of block copolymers. Unfortunately, as was already said, in the corresponding *q*-interval the PS and LC features overlap and trying to resolving them by the using two Gaussian or Lorentzian functions was not possible. However, regarding the *q* values in Figure 5.7, d_N variation with composition is no higher than 0.025 nm.

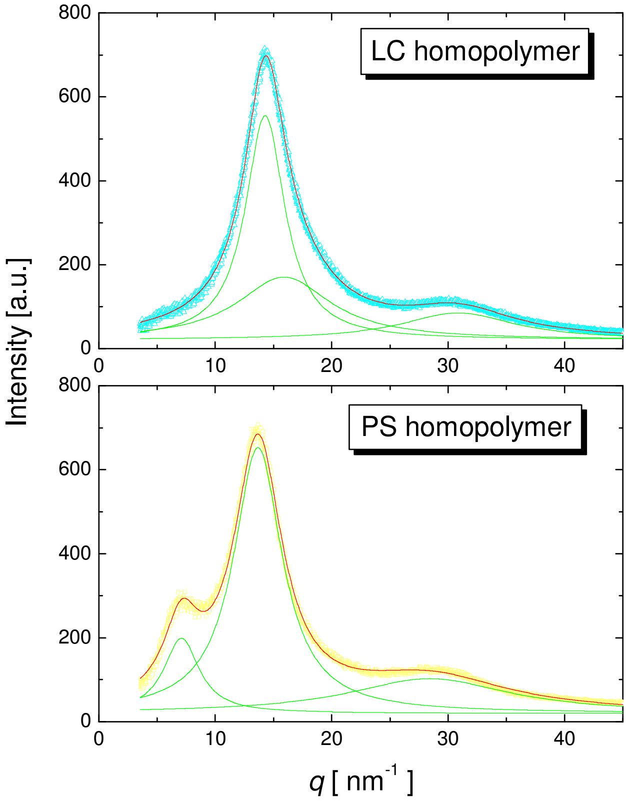

Figure 5.5. WAXD profiles measured at room temperature for LC and PS homopolymers.

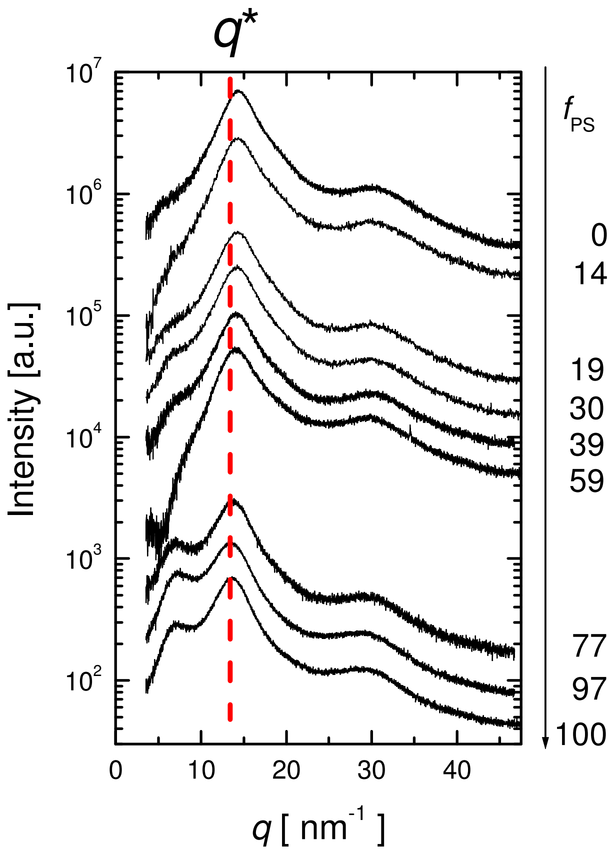

Figure 5.6. WAXD profiles measured at room temperature for PSLC block copolymers. The curves are shifted for clarity.

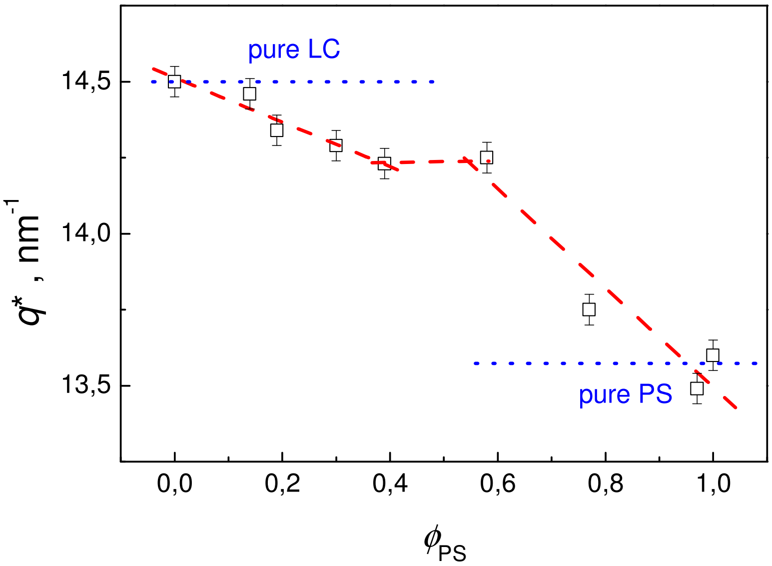

Figure 5.7. The position of the most intense peak in the PSLC block copolymer WAXD profiles as a function of the PS volume fraction.

5.2. Domain Structure of the PSLC Block Copolymers

The domain structure of the microphase separated PSLC block copolymers was studied by SAXS. Several structures were found – PS cylinders in LC matrix, alternating lamellae, hexagonally packed LC cylinders in PS matrix and LC spheres in PS matrix.

5.2.1. Lamellar microstructure

The desmeared SAXS profiles of the block copolymers PSLC 39/61, PSLC 59/41 and PSLC 77/23 are shown in Figure 5.8. Three to four narrow and high intensity Bragg peaks can be well distinguished in each scattering profile (Figure 5.8). The q_n values corresponding to the peak positions are related by $q_n = nq_1$, where q_1 is the position of the first peak. This relation is characteristic for a lamellar structure (see chapter 4.1). In case of PSLC 77/23, two additional higher order peaks of weak intensity at q_n values $5q_1$ and $6q_1$ are registered. In order to determine the precise q_n position of each peak, a Gaussian fit was used after a Lorenz correction of the data. Example fits are presented in Figure 5.8. The lamellae structure remains during the entire temperature interval of 25–150°C (for the sample PSLC 77/23 also at 170°C). As it was explained in Chapter 4.1, the lamellar period d is given by $\frac{2\pi n}{q_n}$, where n is the order of the reflection, i.e.

$$q_n = \frac{2\pi}{d} n$$

Hence, the peak positions q_n plotted vs. the order of reflection n should fit to a straight line. The d value can be calculated directly by the slope of the line. In this way, the error in the detector height determination (i.e. in the primary beam position) can be eliminated. The plot of the q_n values for PSLC 59/41 vs. n is presented in Figure 5.9. One can see that the data points fit perfectly to a straight line. The d value determined is $\frac{2\pi}{B}$, where B is the slope of the line. The same procedure was performed for all PSLC block copolymers with lamellar structure at the various temperatures. The results are presented in Figure 5.16 and will be discussed later.

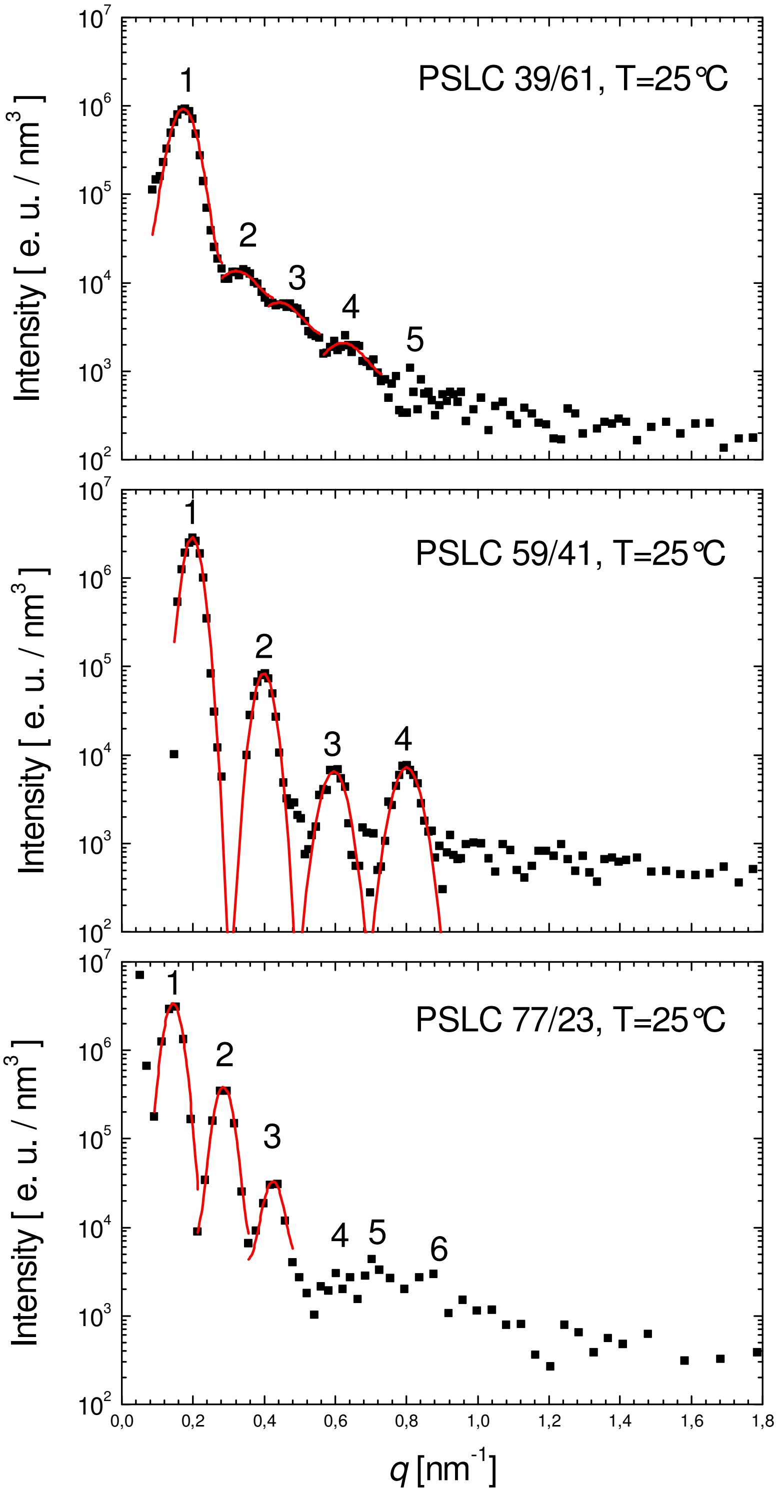

Figure 5.8. Desmeared SAXS profiles of the PSLC block copolymers with lamellar microstructure at 25 °C. The filled squares are the experimental measurements and the solid lines data are Gaussian fits to the data.

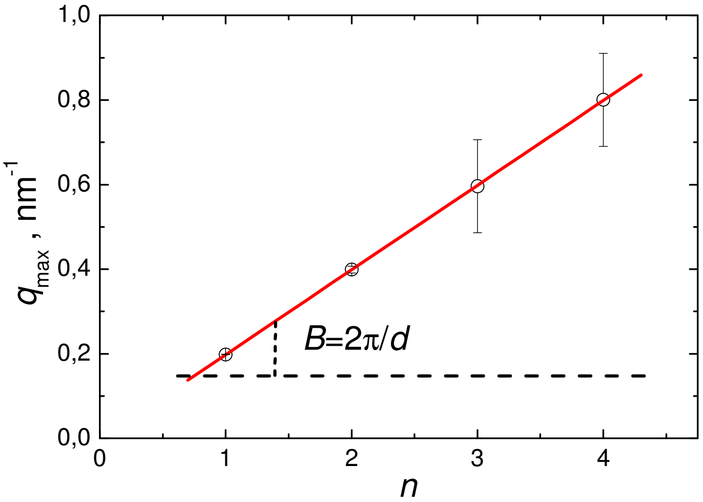

Figure 5.9. The position of the peak maximum vs. the reflection order for the sample PSLC 59/41 at 25 °C. The red line is a linear fit to the data.

As it was already mentioned in Chapter 4.1, there is an alternative method for calculating the lamellae period *d* and the thickness of the thinner lamellae layer i.e., by calculation of the one dimensional correlation function *K*(*z*). The calculated functions according to the given Eq. 4.19, are presented in Figure 5.10. The lamellae period *d* is equal to the position of the first maximum of *K*(*z*). The results at different temperatures are represented with red symbols in Figure 5.16b. One can see that the obtained values agree well within the experimental error with values obtained from the "q_n vs. *n*" plot. Depending on the volume fraction, the thinner layer of the PSLC lamella could be the LC layer (with thickness d_{LC}) or the PS layer (with thickness d_{PS}). When the PS volume fraction is lower than the LC volume fraction, i.e $\phi_{PS} < \phi_{LC}$, then the thickness of the polystyrene layer d_{PS} can be calculated from the correlation function as was explained in chapter 4.1 (Figure 4.3). In the case of $\phi_{LC} < \phi_{PS}$, d_{LC} is calculated analogically. Then, d_{PS} can be obtained as a difference between *d* and d_{LC}.The thickness d_{LC} of the LC layer is presented in Figure 5.16a); the temperature variation in *d* and d_{LC} will be discussed later. The data at room temperature are summarised in Table 5.2.

Let us now focus on the shape of the correlation function. The correlation functions for all PSLC block copolymers, presented in Figure 5.10 deviate from the ideal form as depicted in Figure 4.3. However, they are fairly linear in the initial interval (compare with the upper part of the first triangle in Figure 4.3), which is an indication for a sharp interface between the blocks. This result is consistent with the observations of Fisher at al. [40] and

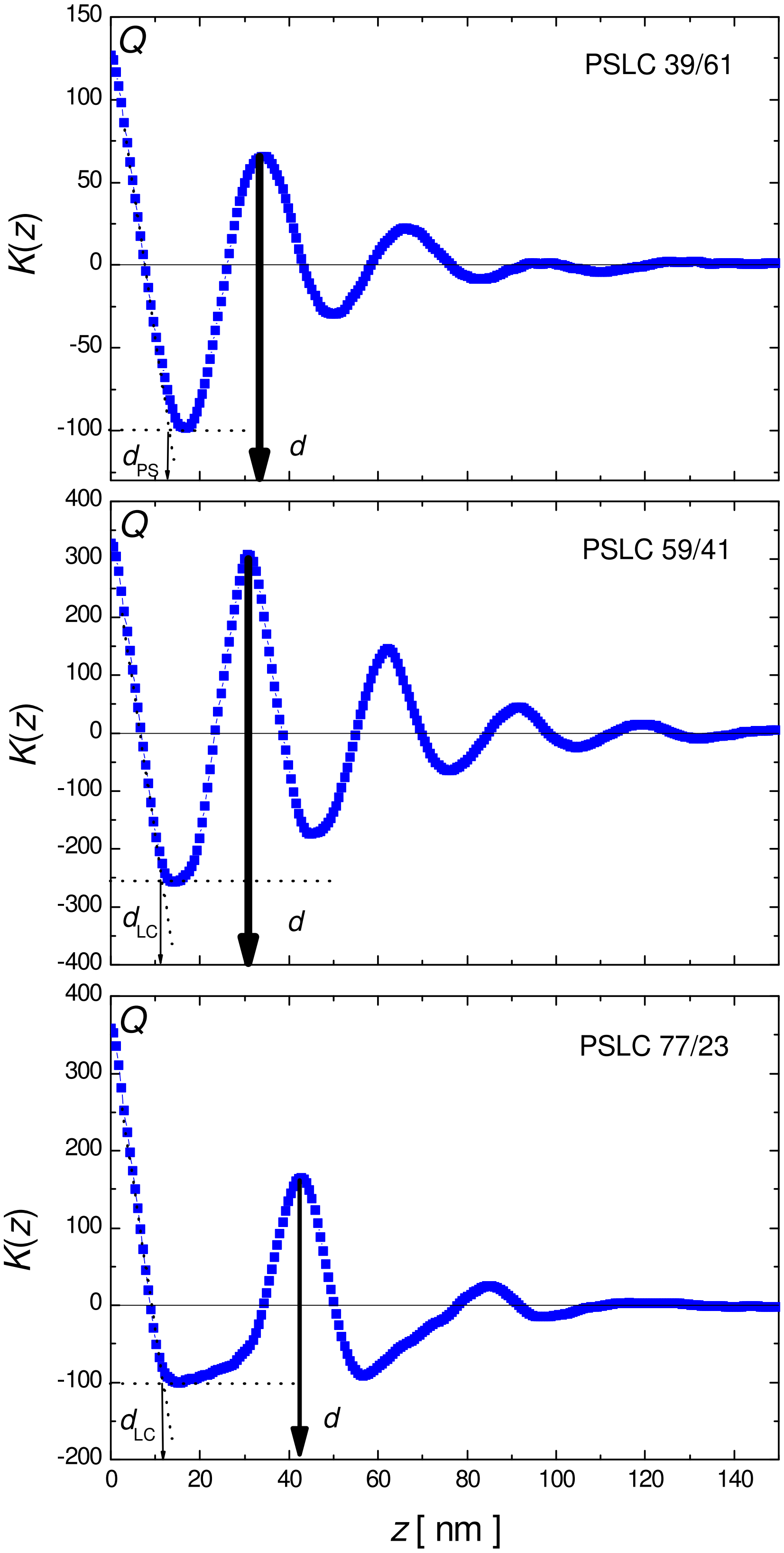

Figure 5.10. The correlation function of the SAXS scattering profiles of the PSLC block copolymers with lamellar microstructure.

Mao et al. [38] for smectic LC/PS block copolymers. The sharp interfaces are expected for block copolymers in strong segregation regime. However, the curvature in the interval around $z=d_{LC}$ ($z=d_{PS}$), indicated a size distribution of the thinner part of the lamellae d_{LC} (d_{PS}). One can estimate, from Figure 5.10 that the sample PSLC 77/23 has the most narrow distribution of d_{LC} (d_{PS}) followed by the PSLC 59/41 and then PSLC 39/61. The curvature around $z=d$ is a result of the variation of the lamellae period d. One can conclude from Figure 5.10 that the lamellae period varies for all presented block copolymers, but mostly for PSLC 39/61.

As we have already seen in Chapter 4.1, the intercept Q of the correlation function with the K-axis (i.e. $K(z=0)$) is proportional to the square of the electron density difference between the two blocks and the product of volume fractions, i.e. in the case of PSLC block copolymers:

$$\Delta n_e = \left| n_{e,LC} - n_{e,PS} \right| = \sqrt{\frac{Q}{\phi_{LC}(1-\phi_{LC})}}$$

The calculated value for Δn_e according the above equation is obtained in units e/nm^3 and increases with ϕ_{PS}. Δn_e is equal to 23 for the sample PSLC 39/61, to 37 for the sample PSLC 59/41 and to 45 for sample PSLC 77/23. The calculated electron density difference between the PS (with mass density ρ_{mPS}=1.04 g/cm^3) and LC (with mass density ρ_{mLC}=1.25 g/cm^3) homopolymers according the Eq.4.10 is: $\Delta n_e^H = 64\, e/nm^3$. The Δn_e^H is calculated, using the mass density ρ_m of the homopolymers, i.e. it should be equal to the Δn_e of fully phase separated system and without chain stretching, coming from the chemical bond between the blocks. All values of Δn_e, obtained from the correlation function are lower than Δn_e^H. This could be a consequence of the different methods of calculation – the correlation function includes several steps of data evaluation and could contain artifacts. The second possibility is that the block copolymers are not 100% phase separated at the domain interfaces. The third and less probable opportunity is that, due to the different stretching, chain conformation may not be the same within the homopolymer and the three lamellar samples, which follows to different mass densities. As we have already seen in Chapter 4.1, the mass density is directly proportional to the electron density, therefore it could lead to different values of Δn_e.

Taking into account that the integrated area under the n-th order peak in Figure 5.8 is proportional to $\sin^2(\pi n \phi_{PS})/n^2$, where $\phi_{PS} = d_{PS}/d$ is the volume fraction of the PS phase (see Chapter 4.1) one can calculate the volume fractions of the different blocks using the integrated intensities I_1 and I_2 of the first and the second peak, after a Lorenz correction of the scattering data for the isotropic sample. The Lorenz correction was performed, in order to fit the measurement of isotropic lamellae sample to Eqs. 4.15-17 (for one dimensional scattering intensity).

$$\frac{I_1}{I_2} = \frac{4\sin^2 \pi\phi_{PS}}{\sin^2 2\pi\phi_{PS}};\Rightarrow \qquad \phi_{PS} = \frac{\arccos\sqrt{\frac{I_2}{I_1}}}{\pi} \tag{5.1}$$

The results are presented in Figure 5.11. The calculated values agree well with the results from NMR measurements (the red points in Figure 5.11). In addition, they coincide within experimental error with the values $\phi_{PS} = d_{PS} / d_{corr}$, calculated from the correlation function (the blue symbols in Figure 5.11). One can see in Figure 5.11 that the calculated volume fractions do not vary with temperature within the experimental error.

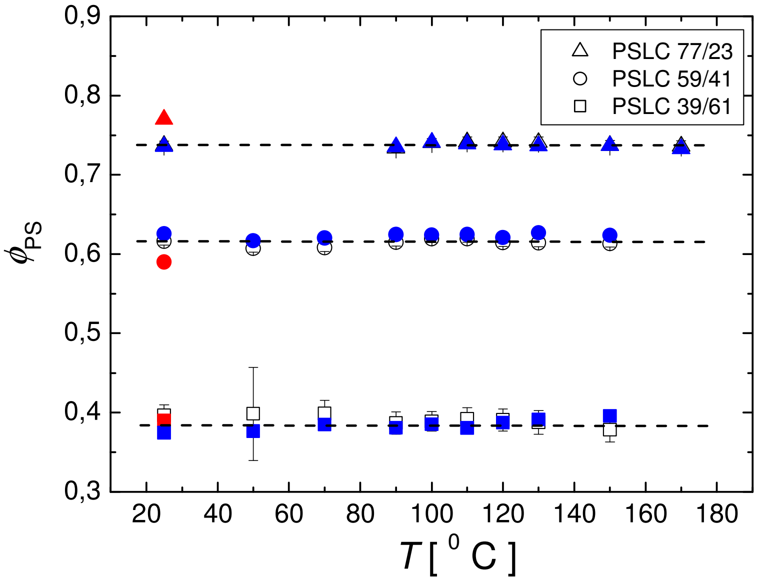

Figure 5.11. The calculated volume fractions of PSLC block copolymers with lamellae structure accorting to Eq.5.1 (black symbols) and $\phi_{PS} = d_{PS} / d_{corr}$ (blue symbols). The red symbols represent the results from the NMR measurements.

5.2.2. Hexagonal microstructure

The scattering profiles of the samples PSLC 7/93, PSLC 14/86, PSLC 19/81 and PSLC 85/15 at T=25 / 30°C and T=150°C are presented in Figure 5.12. Each scattering curve consists of several Bragg reflections superimposed on a significant diffuse scattering component. The positions of the Bragg peaks no longer follow the dependence $q_n = nq_1$ (n=1, 2, 3…), as it was the case for lamellae structures. The scattering profiles in the whole temperature interval were successfully fitted to the Eq.4.20, which describes a hexagonal structure (see Chapter 4.1). The fits to the experimental points are shown in Figure 5.12. It is obvious that in each case the theoretical model describes the experimental data very well. According to Eq. 4.22 the Bragg peaks are situated at q_1, $\sqrt{3}\ q_1$, $\sqrt{4}\ q_1$, $\sqrt{7}\ q_1$, $\sqrt{9}\ q_1$, $\sqrt{12}\ q_1$, $\sqrt{13}\ q_1$, $\sqrt{16}\ q_1$ etc. As a result, the fit gives the lattice constant, a, the radius of the cylinders, R, as well as the mean squared displacement u^2 of the cylinders from the "ideal hexagonal lattice" positions (which takes part in the Debye-Waller factor in Eq.4.21) and the variance of the cylinder radii distribution. The data for a and R at room temperature are summarised in Table 5.2 on page 95. The temperature dependence of the mean squared displacement u^2 is presented in Figure 5.13. The mean squared displacement does not vary with temperature within the experimental error. Such behaviour is expected, because the displacement is caused by intrinsic structure imperfections, unlike the case of small molecule crystal lattices in which the Debye-Waller factor reflects the temperature vibrations of the atoms. However, u^2 shows clear variation with the sample type. The relative lattice distortion – $\frac{|u|}{a}$ is in the range of 9-12% for PSLC 7/93, PSLC 14/86 and PSLC 19/81, and increases up to 26% for PSLC 85/15. In addition, the Bragg reflexions for PSLC 7/93, PSLC 14/86 and PSLC 19/81 are better pronounced in Figure 5.12, than those for PSLC 85/15, where diffuse scattering dominates. The relative lattice distortions seem to be much higher for the lattice with LC domains in the PS matrix than for the lattice with PS domains in the LC matrix. However, u^2 does not change with temperature, i.e. passing through the both PS and LC glass transitions and the nematic-to-isotropic transition. This means that the variation of u^2 depends on the polydispersity, which may be different for the four PSLC block copolymers, than on the chain conformation.

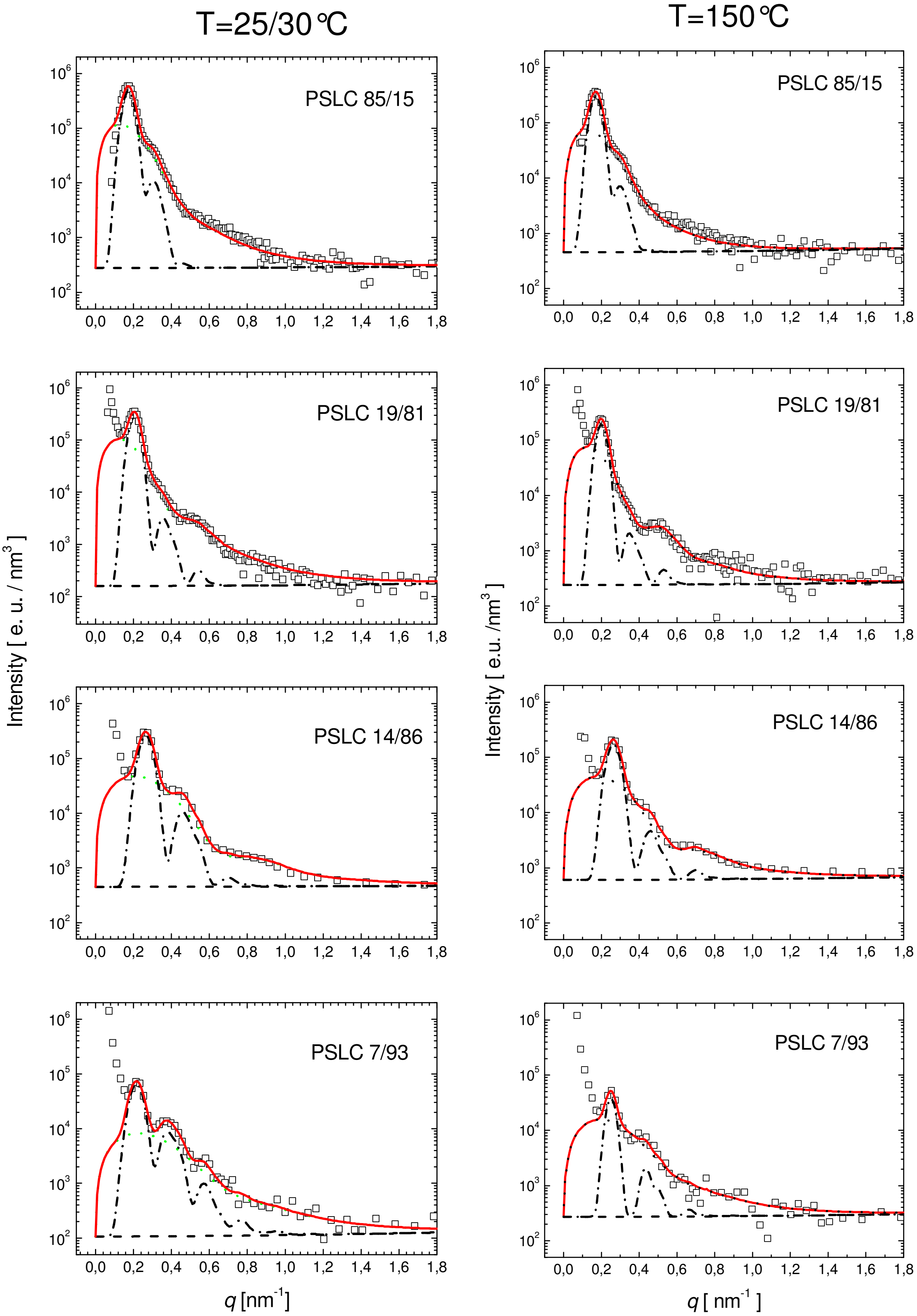

Figure 5.12. The desmeared SAXS profiles of the PSLC block copolymers with hexagonal microstructure at 25 °C (the data for PSLC 14/86 are taken at 30 °C) and 150 °C for samples PSLC 85/15; 19/81; 14/86; and 7/93. The experimental data are given by points and the fits by the solid red line. The dashed lines represent the three component of the scattered intensity (Chapter 4.1 Eq. 4.20).

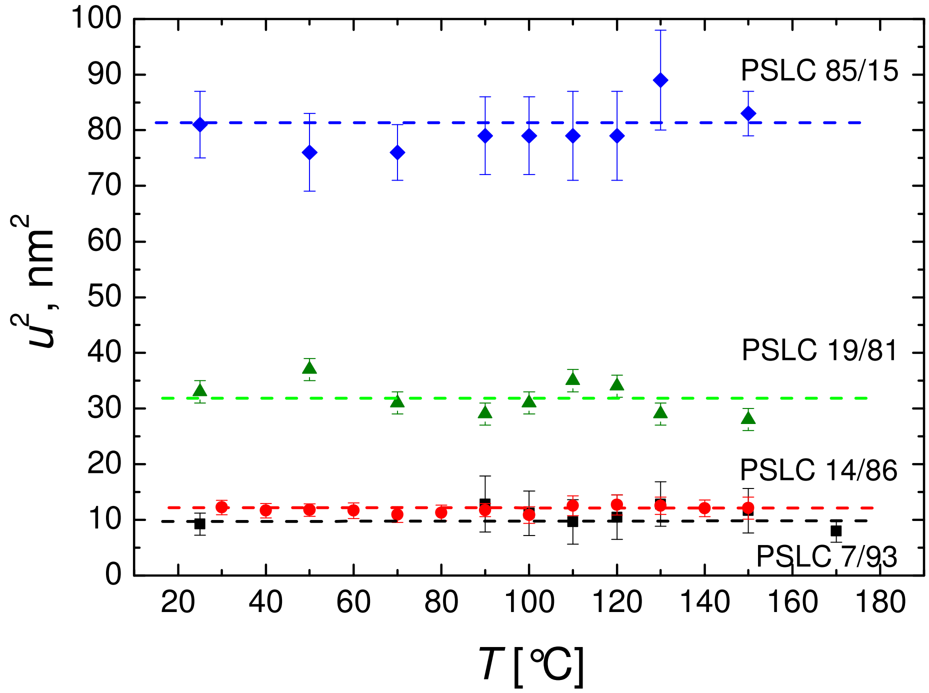

Figure 5.13. The mean squared displacement u^2 for samples PSLC 7/93, PSLC 14/86, PSLC 19/81 and PSLC 85/15.

5.2.3. PSLC 30/70 – on the border between lamellar and hexagonal microstructure

The scattering profiles of the sample PSLC 30/70 are presented in Figure 5.14. The diffraction intensities are high and comparable with those of the neighbouring samples PSLC 19/81 (hexagonal structure) and PSLC 39/61 (lamellar structure). However, it is hard to separate the Bragg peaks from the strong diffuse scattering. Two peaks can be recognized– one primary peak at $q_1 \sim 0.157$ nm^{-1} and a second one at position about $q_2 \sim 2.5q_1$. This ratio does not fit to 1:2, which characterises the lamellar structure. It is closer to $1{:}\sqrt{7}$, which is characteristic of the hexagonal structure. However, the fit of the scattering points to the hexagonal model did not give satisfactory results within the whole investigated temperature interval (the best possible fits at T=25°C and T=150°C are given in Figure 5.14). The composition of this sample is intermediate to those of samples which have lamellar and hexagonal structures, so it is possible these two microstructures may coexist in this sample.

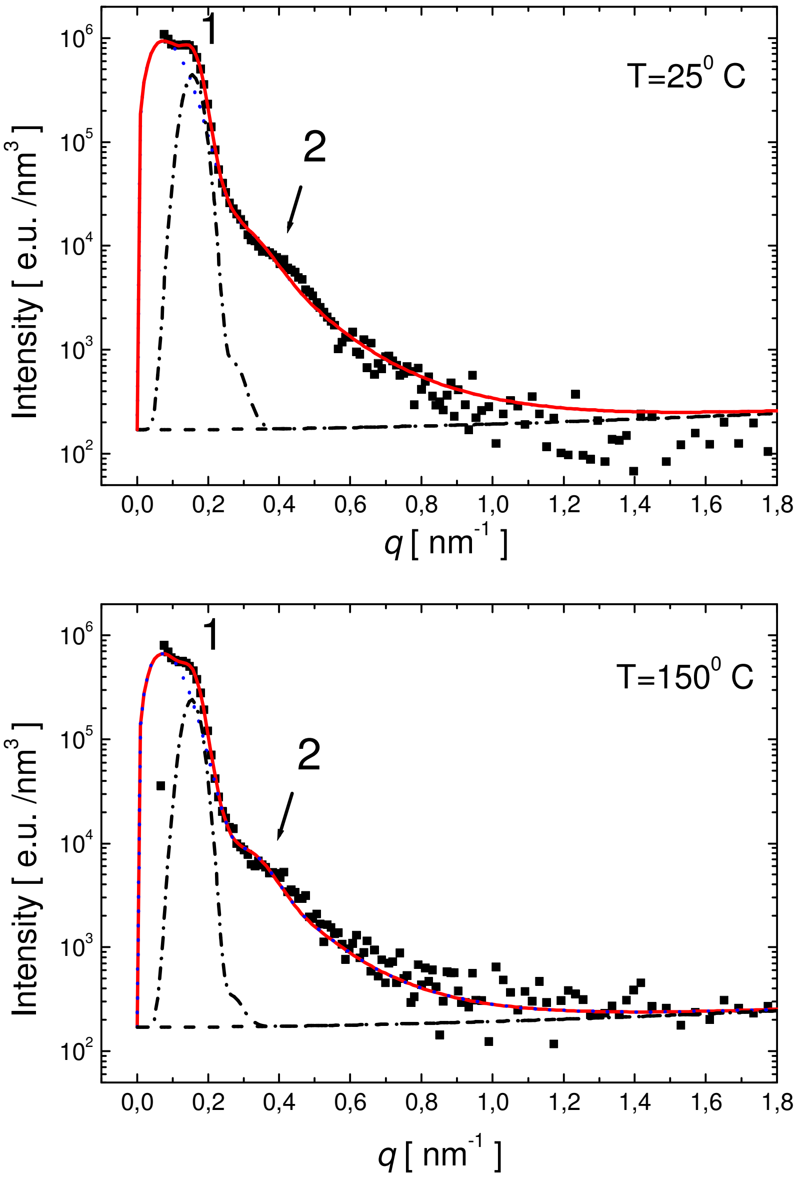

Figure 5.14. The desmeared SAXS profiles of PSLC 30/70 at 25°C and 150°C. The best fit to hexagonal microstructure is also shown.

Another possibility is that the sample has a bicontinuous cubic microstructure. Such structures have a complex three-dimensional geometry that can be represented as interconnected cylinders arranged in a cubic lattice (see Chapter 3.1, Figure 3.4). They appear in the phase diagram between the hexagonal and the lamellar microstructures and give scattering curves of high intensity exactly as in the present case. However, unlike the present case, they are expected in the weak and intermediate segregation regime [23] (see Figure 3.3). The attempt to fit the diffraction pattern of PSLC 30/70 to a bicontinuous cubic structure was not successful. The bicontinuous structure is observed very rarely in one-component LC/I block copolymer systems [38, 42].

The next possibility is that we have a mixed lamellar-hexagonal structure or perforated lamellae (PL) morphology [36]. The PL morphology consists of alternating lamellae with cylindrical perforations arranged in hexagonally close-packed layer (PL/HPC) [20, 24] or in a modified layer (PL/ML) [31]. The PL/ML structure retains periodic order between the planes of cylinders, but not necessarily between the cylinders themselves. As it was mentioned above, the strong diffuse scattering indicates large distortions in the lattice and thus, excludes the possibility of a pure structure, such as cylinders with hexagonal symmetry or a complex structure with high regularity. The sample PSLC 30/70 most probably lies at the border between the hexagonal and the lamellar microstructures and has a mixed structure with large domain disorder. It has to be noted that it was not possible to assign the data at any of the temperatures studied (25 °C up to 150 °C) to only one microstructure. An attempt was made to "cure" one of the present microstructures and obtain a pure structure by annealing the sample at 120 °C (a temperature higher than the T_i) for 24 hours under vacuum. However this was not successful, most likely due to the fact that the process of structural change is very slow.

5.2.4. PSLC 97/3 – spherical microdomains.

The scattering profiles for sample PSLC 97/3 at *T*=30°C and *T*=150°C are given in Figure 5.15. The scattering data show one primary peak and a relatively strong diffuse scattering component. The total intensity is very low compared to the other PSLC block copolymers, which is an indication for a not very well ordered structure. The sample PSLC 97/3 is the one with the highest molecular weight, but at the same time the one with the lowest LC volume fraction. Hence, it could be very close to the border between the microphase separated and disordered state (see the theoretical phase diagrams in Figure 3.3; 3.7 and 3.8). All theoretical diagrams were calculated for a certain value of the χ parameter, which could be higher or lower than χ of the block copolymers examined in this thesis. This is the reason that both, microphase phase separated and disordered states could be possible. DSC measurements for sample PSLC 97/3 show only one glass transition – that of PS, most probably because the mass of the LC block was too low to be detected. Hence, this fact is not a clear evidence for a disordered state.

Let us compare the scattering profile of the sample PSLC 97/3 at *T*=30°C with the theoretical scattering curve obtained by Leibler for the block copolymer in disordered state [9] (Chapter 3.1, Figure 3.1) and the experimental curves obtained by Stühn *et. al.* [26] (Figure 3.2). One can see that the peak of the disordered state is asymmetric and the intensity decreases with very smooth and continuous slope change with increasing of *q*. The block copolymer scattering pattern for microphase separated state in Figure 3.2 shows a shoulder at q~0.5 nm^{-1}, which disappears at temperatures above the order-to-disorder transition. The scattering pattern for PSLC 97/3 does not look similar to the scattering profiles of the disordered block copolymers shown in Figure 3.1 and 3.2 (open symbols). It shows one primary peak and additional broad feature at q~0.4 nm^{-1}, which can be well fitted with a spherical form factor function (Eq. 4.25).

One can see in Figure 5.15, that at *T*=150° the intensity of the first maximum slightly decreases and the diffuse scattering increases. This indicates that local order of the lattice decreases. However, the shape of the scattering curve remains similar to the shape at *T* = 30°. Therefore, one can suggest that despite the low volume fraction of the LC block, the sample is microphase separated in the whole temperature interval 25-150°C and the LC block forms spherical domains. The question is: what is the mutual correlation between the spheres, are they ordered in cubic lattice (the most common structure for such kind of systems is the body centred cubic lattice (bcc)) or they have only short range ("liquid-like") order? The scattering intensity for the sample PSLC 97/3 is about one order of magnitude lower than that for PCLS 85/15 and PSLC 30/70. Moreover, the total intensity mainly originates from diffuse scattering, which suggests that even if we have a bcc structure, the microdomains are not very well ordered. For diblock copolymers with chiral side chain LC block and PS block, with LC volume fraction less than 25%, Anthamatten and Hammond observed dispersed phase morphologies consisting of nonperiodic array of LC spheres inside continuous PS matrix [36]. However, the architecture of the LC block examined by them is quite different from ours, which could make a big difference in the phase diagram. For instance, they have not detected hexagonally packed LC cylinder structure in PS matrix and with decreasing the LC volume fraction, their system jumps directly from a lamellar to a dispersed phase.

The fits of the experimental scattered data with bcc (Eq. 4.20; 4.21; 4.24 and 4.25) and Percus-Yevick (Eq. 4.26) model functions (see chapter 4.1) are presented in Figure 5.15.

The bcc fit of the data at the room temperature gives as the radius of the spheres – $R = 4.7\pm0.8$ nm, the lattice constant – $a = 38.3\pm1$ nm, the mean squared displacement of the spheres from their equilibrium positions (included in the Debye-Waller factor) – $u^2 = 242\pm93$ nm^2, and the variance of the spherical radii distribution $\sigma_R = 1.44\pm0.2$ nm. The volume fraction calculated as $\phi_{LC} = 2.\frac{4}{3}.\pi R^3 / a^3$ is equal to 0.015, which is slightly lower than the value obtained from NMR experiments. This difference may appear because arround the pure LC domain core may exist "diffuse interface" shell, which cannot be detected compleately by the X-ray measurements.

The Percus-Yevick fit gives as a result the radius of the sphere $R = 4.8\pm0.1$nm, the variance of the spherical radii distribution $\sigma_R = 1.44\pm0.07$ nm, the hard sphere radius $R_{\mathrm{hs}} = 13.4\pm0.1$ nm and the hard sphere volume fraction $\phi_{LC}^{HS} = 0.24 \pm 0.4$. The last parameter is much larger than the volume fraction, calculated on base of the NMR measurements, because the radius of the hard sphere interaction R_{hs} is larger than the radius of the sphere R.

It is clear that both models equally fit the experimental data. However, some of the fit parameters as the mean squared displacement u^2 and the volume fraction are obtained with large uncertainty. The radius of the LC spherical microdomains obtained by the Percus-Yevick model ($R = 4.8 \pm 0.1$ nm) coincides with the value obtained by the bcc model ($R = 4.7 \pm 0.8$ nm). The equal quality of both fits shows that the microstructure of PSLC 97/3 is neither that of dilute separate spheres nor that of a well-ordered bcc lattice. Rather, it has to be considered as a largely disordered bcc lattice or an ordered liquid of spheres.

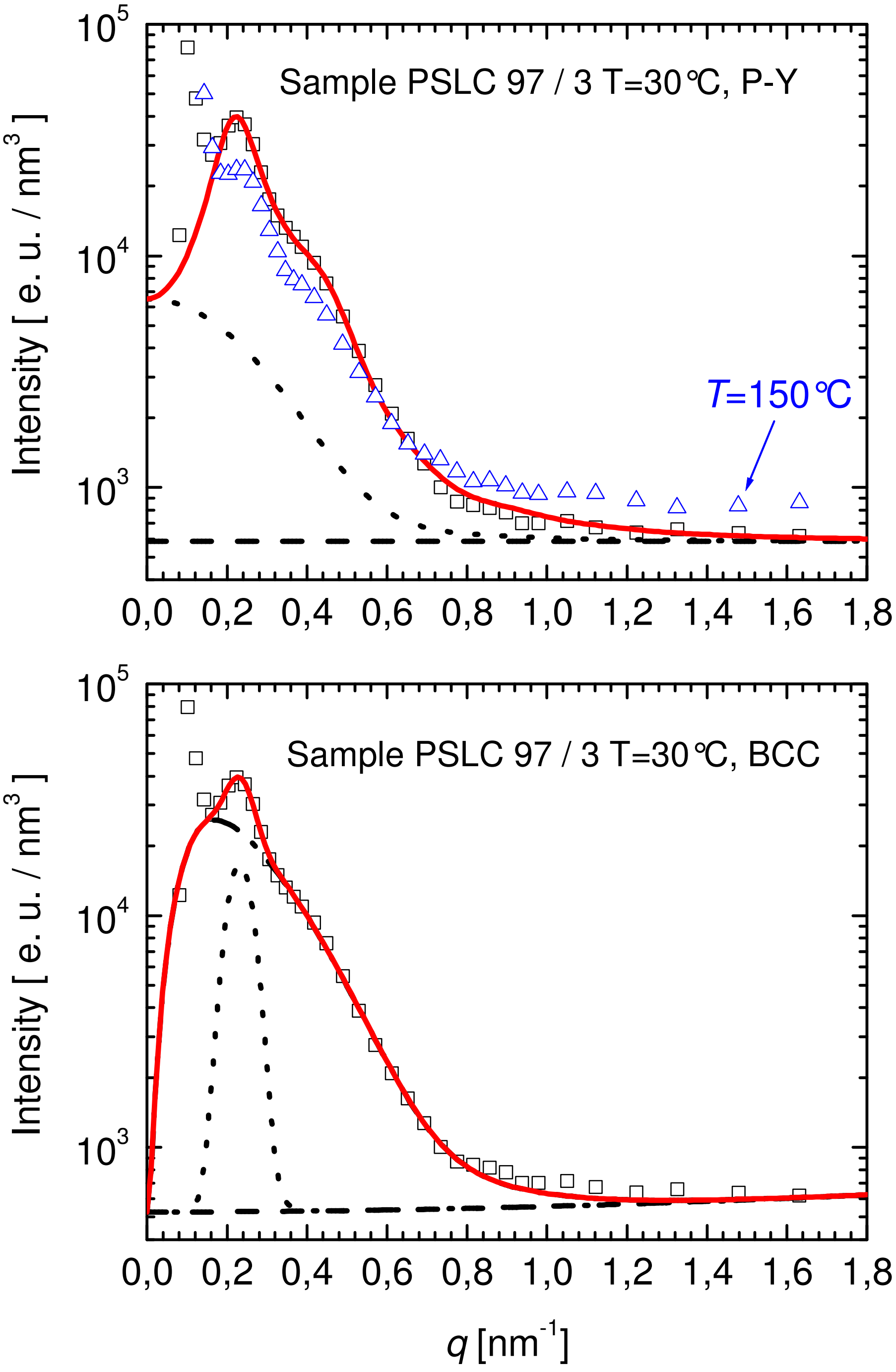

Figure 5.15. The desmeared SAXS profile of PSLC 97/3 at 30 °C and 150°C. Both the fits by the Percus-Yevick model of "hard sphere liquid" (top) and by the bcc model (bottom) of the data at 30 °C are presented.

5.2.5. Temperature Dependence of the Domain Dimensions

The temperature variations of the lattice parameters d, d_{LC} and d_{PS} of the samples PSLC 39/61, PSLC 59/41 and PSLC 77/23 with lamellar structure are shown in Figure 5.16. The data correspond to the scattering curves measured during the cooling run. The lamellae period d increases only slightly with increasing temperature, up to approx. 115 °C and then slightly decreases (1.1 nm (3.2%) for PSLC 39/61, 1.1 nm (2.6%) for PSLC 77/23 and only 0.2 nm (0.9%)for PSLC 59/41) (Figure 5.16b). A similar, but much more pronounced variation has been reported by Zheng and Hammond [34] in a detailed study of the domain spacing in lamellar microstructure attained by side-chain LC/I block copolymers with chiral LC block, forming smectic mesophase. They explain the decrease in the lamellae spacing above T_i as a result of the more random rearrangement of the LC backbone and side-chains in isotropic state than in the smectic one. The same effect is described by Yamada et al. [99] for block copolymers of polystyrene and poly [6-[4-(4-methoxyphenyl)phenoxy]hexyl methacrylate]. The lamellar period drops by more than 5 nm (~20%) above the smectic-to-isotropic transition. In contrast, the change in the lamellae period above the smectic-to-isitropic transition for diblock copolymer of polystyrene and poly[6-[4-(4'-cyanophenyl)phenoxy]hexyl methacrylate] is less than 1 nm (less than 5%) [104]. The different behavior of these two systems with a similar chemical structure was explained as a result of the different structure of the smectic phase. Data for the influence of the nematic-to-isotropic transition on the lattice parameters were not found in literature.

The lamellae period d for the samples PSLC 39/61, PSLC 59/41 and PSLC 77/23 decreases over the range of the nematic-to-isotropic transition (indicated by dashed lines). The decrease is comparable to this, found in [104]. The effect of the retraction of the LC block main chain above T_i overcomes the effect of the initial slight increase in the domain dimensions as a result of the thermal expansion of the polymer Information about the temperature variation of the domain dimensions d_{LC} and d_{PS} would be helpful, but the broad uncertainty interval inhibits an unambiguous analysis.

The conformation of the LC backbone is a result of the competition between several factors. The most important are the nematic field, the temperature and the spatial constrain, introduced by the chemical bond with the PS block. The end-to-end distance d_{ee} of the polymer chain is proportional to the lamellae period d. For a polymer chain with a random

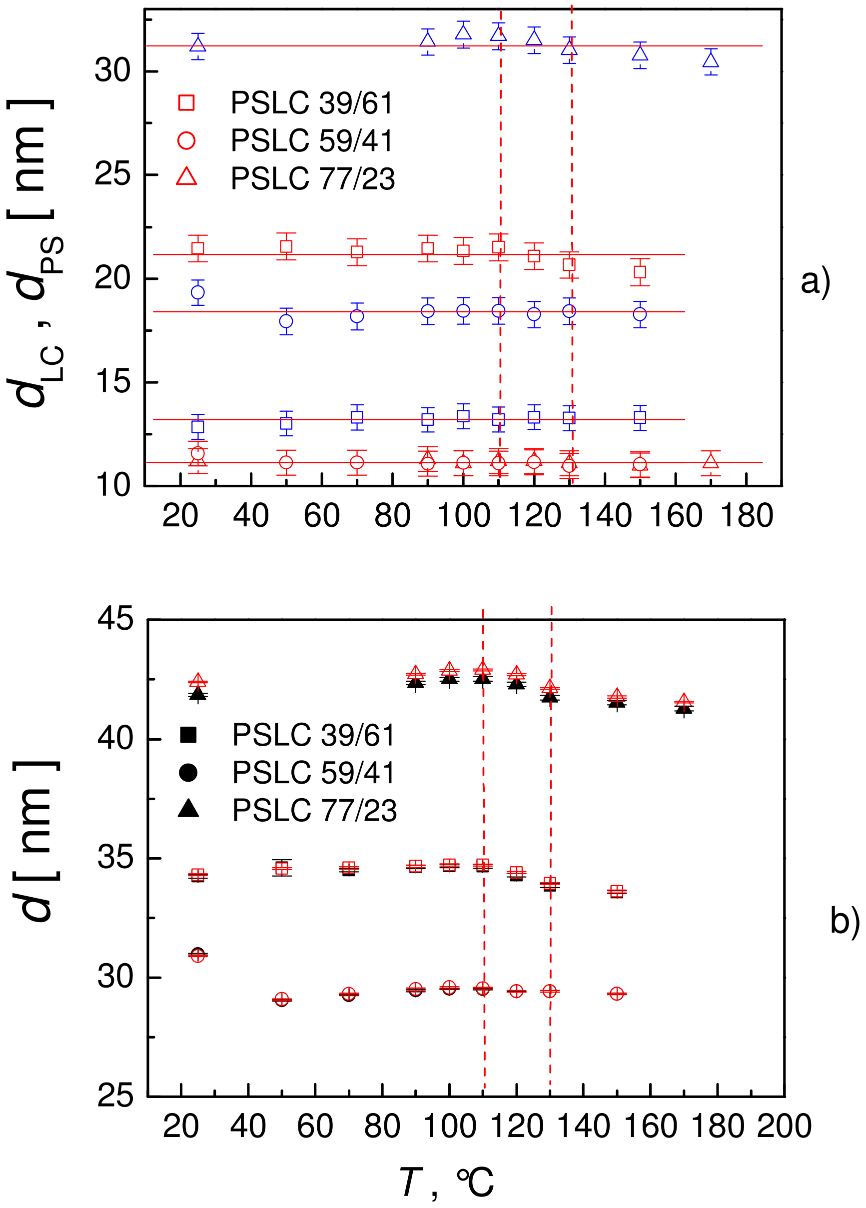

Figure 5.16. (a) The temperature dependence of the thickness of the LC block d_{LC} (red) and the thickness of the PS block d_{PS} (blue), derived from the correlation function. (b) The temperature dependence of the lamellae period d. The red points denote the results derived by calculating the correlation function; the black points represent the data calculated directly from the scattering pattern. The T_i is denoted by a dashed line.

coil conformation, d_{ee} is proportional to the square root of its molecular weight or equivalently, the degree of polymerization (the number of the monomer units) N, i.e. $d_{ee} \sim d \sim N^{\frac{1}{2}}$. The conformation of the polymer chain in microphase separated block copolymers differs from a random coil conformation, because the chains are stretched normal to the interface. This stretching is a consequence of the fact that the two blocks belong to separate domains but remain connected by a chemical bond. For example, the scaling behaviour for a standard I/I diblock copolymer in the strong segregation regime is

$d \sim \chi^{\frac{1}{6}} N^{\frac{2}{3}}$ [12, 109]. The Flory-Huggins interaction parameter is inversely proportional to the temperature (Eq. 3.1) and, therefore, d should decrease with increasing the temperature. χ takes part in the scaling equation with a power 1/6, but a certain influence can not be excluded. The additional stretching factor at temperatures below T_i is the nematic field. Above the T_i, the chain tends to retract and the scaling power decreases.

Let us consider the scaling of LC and PS block dimensions d_LC and d_PS with respect to the number of monomer units N. Figure 5.17 shows examples for linear fits of log $d_{\mathrm{PS(LC)}}$ vs log $N_{\mathrm{PS(LC)}}$. The data for d_{PS} and d_LC obtained by correlation function are used for estimating the scaling behaviour, although the error is large. Additional uncertainty is introduced by analyzing a data set consisting of only three points. One can see in Figure 5.17 that the uncertainty, obtained for PS block is much higher than this for LC block. The results from the fits (the scaling power for PS and LC blocks) are presented in Figure 5.18. The error in PS block scaling power is in the interval 27-40% therefore the temperature variation will be not regarded. The scaling of LC domain dimensions is compatible with a power law $d_{LC}\sim N^{0.85}$ at room temperature. Above the nematic-to-isotropic transition the scaling power decreases slightly to 0.81. This change could be explained with the retraction of the LC backbone favoured by the nematic-to-isotropic transition above T_i, although it is very close to the uncertainty interval. The nematic potential does not contribute anymore to the stretching of the backbone. This allows to the backbone to retract from its entropically unfavourable stretched conformation to a more random one and the power of scaling law decreases. This change of the LC chain conformation leads to the observed decrease of the domain dimensions. A scaling power of 0.8 was obtained from Almdal *et al.* [109] for isotropic nearly symmetric poly(ethylene-propylene)-poly(ethylene) diblock copolymer melts in the intermediate microphase separation regime. Hadziioannou and Skoulios [110] obtained a scaling power of 0.79 for polystyrene/polyisoprene di- and three- block copolymers in strong segregation regime. These values agree well with the results, obtained in this thesis.

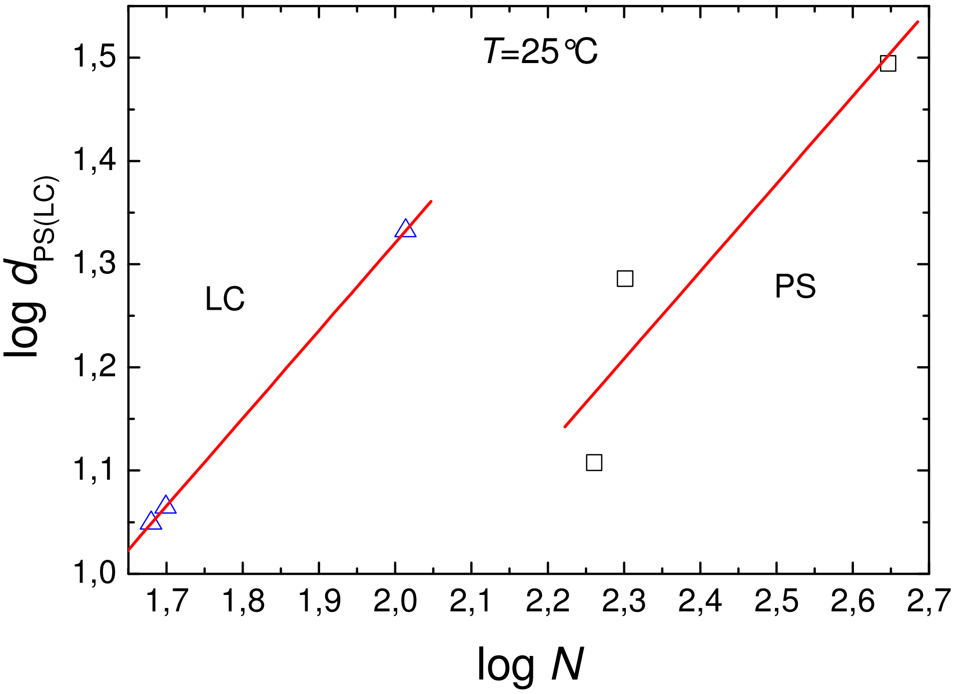

Figure 5.17. The log of domain dimensions for PS block vs. log of degree of polymerisation N at T=25°C.

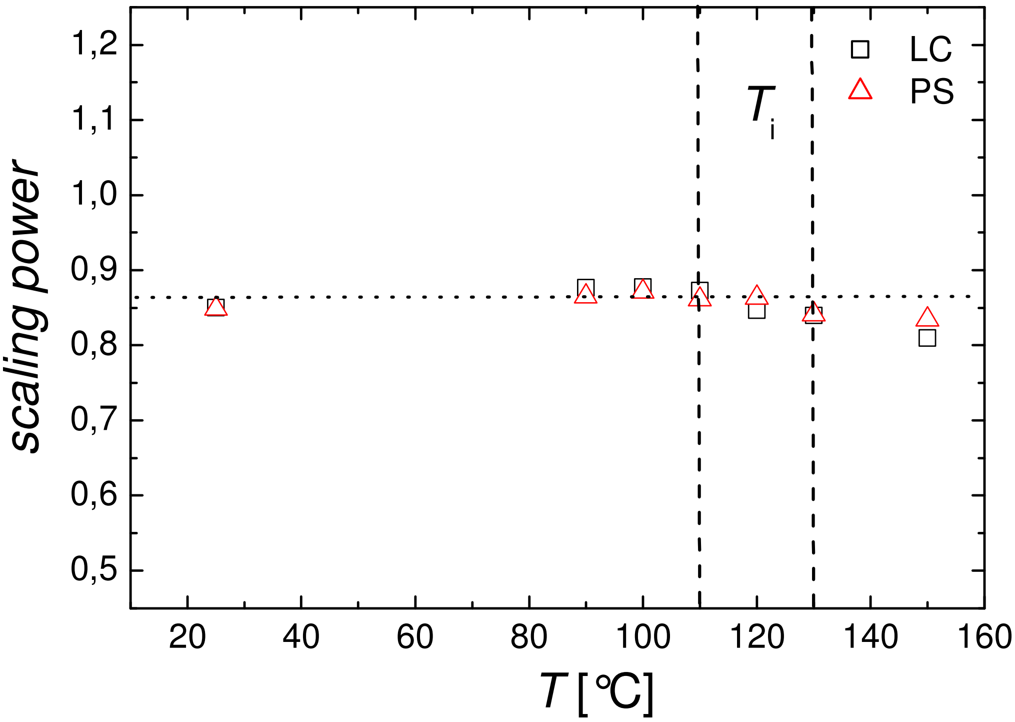

Figure 5.18. The scaling power for PS (red triangles) and LC (black squares) blocks vs. T.

The variations in the domain dimensions of the hexagonal structure will be regarded only qualitatively. The lattice constant of the hexagonal lattice and the radius of the cylinders vs. temperature are shown in Figure 5.19.

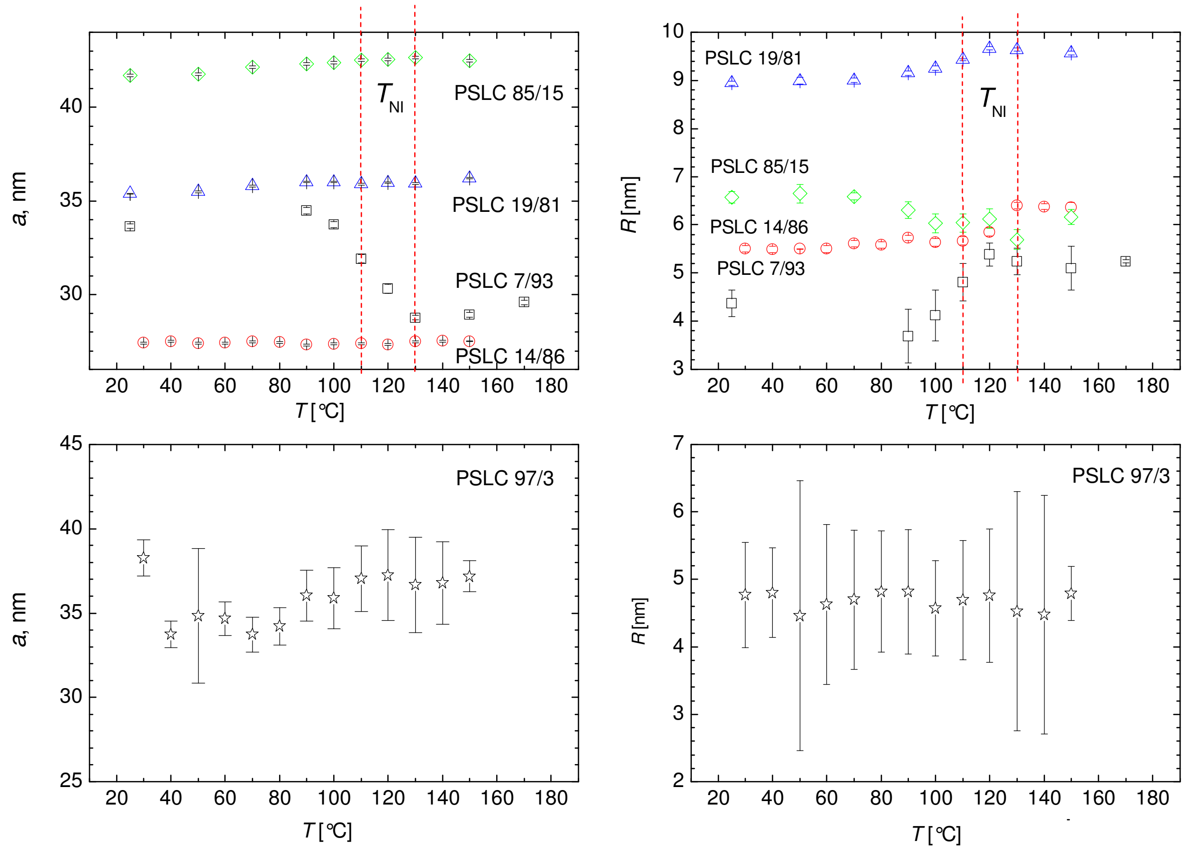

Figure 5.19. The temperature dependence of the microstructure parameters: (left) lattice parameter, a and (right) domain radius, R; (top) hexagonal structures, (bottom) cubic structure. The T_i interval is denoted by dashed lines.

The lattice constant does not vary with temperature, with the exception of sample PSLC 7/93. The lattice constant for PSLC 7/93 decreases above T_i whereas the radius of the PS cylinders increases. PSLC 7/93 has the lowest PS content and most probably lies very close to the border between the hexagonal and bcc microstructure in the phase diagram (as depicted in Figure 5.21). Therefore, an order-to-order transition (OOT) could be expected above the nematic-to-isotropic transition temperature. Usually, when the OOT occurs with increasing the temperature, a structure with lower curvature is replaced with a structure with higher curvature. An exception to this rule was reported by Anthamatten and Hammond [36]. They obtain an OOT from perforated lamellae to pure lamellae structure with the increasing of the temperature. This extraordinary behaviour was attributed to the conformational asymmetry of the diblocks. An OOT from hexagonally packed cylinders to bcc lattice on increasing the temperature has been experimentally detected for a PS-LC-PS triblock copolymer [41]. The order-to-order transition is determined by the change in the energy balance at temperatures above T_i. The elastic energy F_e (see Eq. 3.15) arising from nematic field distortions [35, 111] is excluded from the energy balance. It has been shown [111] that the elastic forces created by the nematic field distortions lead to interaction between the particles. These interactions can be repulsive or attractive, depending on the anchoring condition of the mesogen on the surface of the particle. The strong homeotropic anchoring results in the repulsion of the particles from each other, the soft homeotropic anchoring results in attraction at short distance. The case of planar anchoring has not been regarded theoretically. However, the experimental results suggest that the particles are attracted to each other similar to the case of weak homeotropic anchoring [41]. It was shown, that the coalescence of the spherical PS domains below T_i is realized along the [1,1,1] crystallographic direction (the shortest interdomain distance) [41]. In this case the lattice constant of the hexagonal lattice a_{hex} must be equal to the smallest distance between the spheres in the bcc lattice, i.e. $a_{hex} = (a/2)\sqrt{3} = 0.866\,a_{sph}$, where a_{sph} is the bcc lattice constant [41]. In addition, the nematic field around a spherical particle with planar anchoring has bipolar structure, which results in distortion in the shape of the particle [40]. The clearing of nematic field above T_i would allow the domain shape to return to that expected at such block volume ratio for I/I block copolymers.

The investigated PS-LC-PS triblock copolymer in [41] has the same chemical composition as the PSLC regarded in the present work. The PS volume fraction – $\phi_{PS} = 0.12$, was higher than the volume fraction of the sample PSLC 7/93. Therefore, one can expect that above T_i PSLC 7/93 may undergo order-to-disorder transition.

The variation of the position of the first maximum q_1 with temperature for sample PSLC 7/93 is presented in Figure 5.20. The scattering vector q_1 varies in the same way as described in [41]. Assuming a bcc structure and calculating the lattice constant from the position of the first maximum as $a_{sph} = 2\pi\sqrt{2}/q_1$, one obtains $a_{hex}(T = 110°C) = 0.9\,a_{sph}(T = 130°C)$, which is very close to the ratio obtained in [41]. However, the shapes of the scattering curves for the sample PSLC 7/93 below and above T_i are very similar and the attempt to fit the profile by bcc model was not successful. Hence, in the present case we do not clearly observe an OOT. This significant change in the lattice constant could indicate only an onset of OOT from hexagonal to bcc microstructure, which is, however, not completed. It means that even after excluding the elastic energy from the Equation 3.15, the bcc structure has higher free energy than the hexagonal arrangement. The released nematic field energy is not sufficient to cover the energy expenses for the OOT and the domains only rearrange. Above T_i the PS domains expand (R increases), while the LC domains contract (a decreases) due to retraction of the LC backbone in the isotropic state.

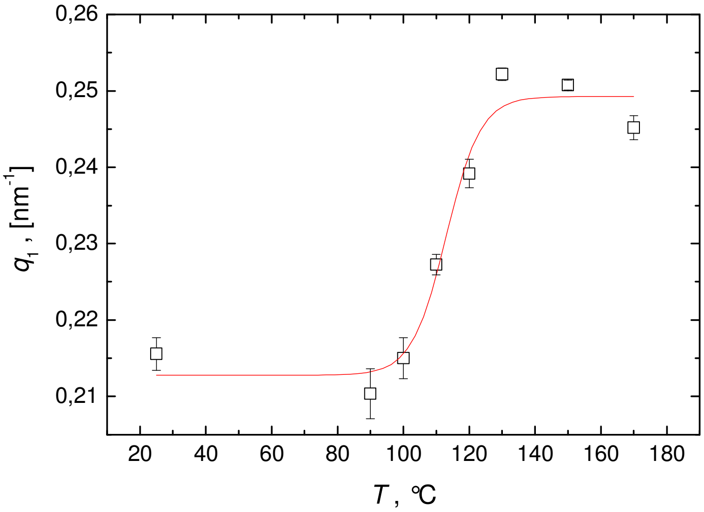

Figure 5.20. The variation of the position of the first maximum for sample 7/93 with temperature. The data are taken from the cooling run.

The lattice constant for the other three block copolymers with hexagonal structure practically does not vary with temperature. However, the radii of the cylinders R change. In the case of PSLC 14/86 and PSLC 19/81, R increases similarly as for PSLC 7/93. For PSLC 77/23 R decreases. Keeping in mind that for PSLC 77/23 the cylindrical microdomains encapsulate the LC block, unlike in PSLC 7/93 and PSLC 14/86, we arrive at the same conclusion as in the case of lamellae structure: above T_i the PS domains expand, while the LC domains retract.

5.2.6 The phase diagram

The phase diagram of PSLC block copolymers is presented in Figure 5.21. This differs from the experimentally measured [22, 23] and theoretically obtained value [14] ones (Figure 3.3) for I/I block copolymers. The phase diagrams of I/I block copolymers are symmetric and mainly determined by the ratio of the block volume fractions, i.e. from geometrical reasons. The phase diagrams of LC/I block copolymers depend strongly on the specific block copolymer, because the equilibrium structure is determined by several other factors in addition to the volume fractions [37], which are:

- The preferred anchoring condition of mesogens at the domain dividing surface (planar or homeotropic).
- The curvature of the interface, dividing the domains.
- The size of the microdomain relative to the size of the LC mesophase.
- The strength and density of the LC defects.
- The symmetry of the LC mesophase and that of the domains in the microphase separated structure.
- The relative positions of the thermal transition temperatures (T_g, T_i, etc.).
- The coupling of microdomains and LC mesophase to external fields.

Table 5.2 gives the morphologies of the PSLC block copolymers regarded here and the corresponding microdomain dimensions at room temperature.

The phase diagram in Figure 5.21 was built using the data presented in the Table 5.2. Different morphologies were denoted with different symbols and colours. The coloured bar just above the *x*-axis represents the expected morphologies for I/I block copolymer. The borders between the different structures were taken from Matsen and Bates [14] phase diagram for random chosen parameter χN in the strong segregation regime. The green colour represents the area where a bcc structure is expected, the red colour is for hexagonal packed cylinders and blue for lamellae structures. The same colours are used to denote the corresponding structures of the discussed PSLC block copolymers.

Contrary to the phase diagram of I/I block copolymers, PSLC phase diagram is asymmetric. The lamellae interval significantly broadens in the range of $\phi_{PS} > \phi_{LC}$ and the hexagonal and bcc structures shift to the higher PS volume fraction. The picture is different in the range of $\phi_{PS} < \phi_{LC}$: the lamellae structure extends only slightly at the expense of hexagonal structure. However, the hexagonal structure of amorphous cylinders in LC matrix persists down to $\phi_{PS} = 0.07$, which is a significantly lower than the value of 0.14 expected for I/I block copolymers. Therefore the bcc morphology, presuming it exists, is shifted to the lower ϕ_{PS} values compared to the I/I phase diagram. Due to the lack of PSLC block copolymers with $\phi_{PS} < 0.07$, the interval [0, 0,07] was not explored and the existence of bcc morphology of amorphous spheres in LC matrix was not experimentally proved.

Table 5.2. The microstructure characteristic length-scales (d, a, d_{PS} (d_{LC}), R) obtained from the fits.

PSLC block copolymer	Microstructure	Morphology	T [°C]	d, a [nm]	d (corr) [nm]	d_{PS} (d_{LC}), R [nm]
PSLC 7/93	hexagonal	PS cylinders in LC matrix	25	33.6±0.1		4.5±0.2
PSLC 14/86	hexagonal	PS cylinders in LC matrix	30	27.4±0.1		5.5±0.1
PSLC 19/81	hexagonal	PS cylinders in LC matrix	25	46.6±0.2		13.0±0.1
PSLC 39/61	lamellar	PS and LC lamellae	25	34.2±0.6	34.3±0.1	12.8±0.1
PSLC 59/41	lamellar	PS and LC lamellae	25	31.0±0.1	30.9±0.1	11.6±0.1
PSLC 77/23	lamellar	PS and LC lamellae	25	41.9±0.1	42.4±0.1	11.2±0.1
PSLC 85/15	hexagonal	LC cylinders in PS matrix	25	41.7±0.1		6.6±0.3
PSLC 97/3	bcc	LC spheres in PS matrix	30	38.3±1.0		4.7±0.8

Finally, one can conclude that the structures of low interfacial curvature (lamellar and hexagonal) are favoured at the expense of structures of high interfacial curvature (bcc). The physical reason for that is the distortion of the nematic field in the vicinity of the particles [111]. As it was mentioned above, spherical particles suspended in a nematic LC matrix lead to distortions of the nematic director which gives rise to elastic forces between the particles. These elastic forces are compensated by formation of cylindrical instead of spherical domains. Obviously, the energy penalty for the formation of the cylindrical domains, having the next smallest free energy but better compatible with the nematic filed, is smaller than the elastic energy from the nematic field distortions [80]. The distortions of the nematic field cannot explain the broadening of the lamellar phase (up to ϕ_{PS}~0.82 instead of 0.68) at the expense of hexagonal microstructure with morphology LC cylinders in PS matrix. In the case of planar anchoring (Figure 3.6) of the mesogen at the domain dividing surface, the nematic order fits to the both cylindrical and plane domain shape. A possible reason for the lamellae phase broadening could be the influence of the nematic field on the chain conformation so that a lamellar geometric shape is favoured over the cylindrical one. In this way can be explained the much larger broadening of the lamellae phase at $\phi_{PS} > \phi_{LC}$ side of the phase diagram (LC domains in PS matrix) than at $\phi_{PS} < \phi_{LC}$ (PS domains in LC matrix).

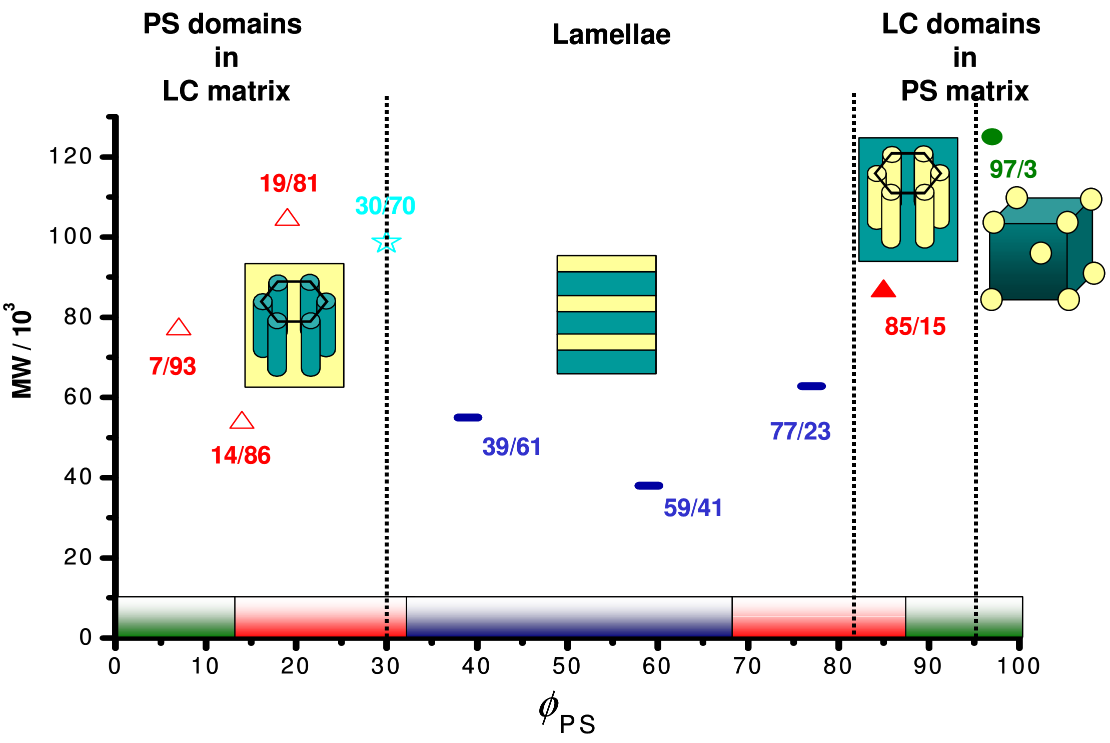

Figure 5.21. The phase diagram of the PSLC block copolymers. The coloured bar above the x-axis represents the expected morphologies for isotropic-isotropic block copolymer. The borders between the different structures were taken from Matsen and Bates [14] phase diagram for random chosen parameter χN in the strong segregation regime. The green colour represents the area where bcc phase is expected, the red colour is for hexagonal packed cylinders and blue- for lamellae structure. The same colours are used to denote the corresponding structures for PSLC samples, investigated in this thesis.

As it was mentioned above, the phase diagram of LC/I block copolymers depends on the anchoring of the mesogen in respect to the domain-dividing surface (defined from the mutual orientation of the domain dividing surface and the nematic mesogens) [35, 36, 37, 77]. Most probably the anchoring in the here presented PSLC block copolymers is planar, i.e. the nematic director is parallel to the interface (as schematically shown in Figure 3.6, Chapter 3). The planar anchoring is the most frequently observed in similar systems [99]. It has been found that mesogens attached to the backbone chain through long spacers can form LC phases with either planar or homeotropic anchoring, while mesogens with short spacers form mainly LC phases with planar anchoring [37, 112].

Figure 5.22 represents the theoretical phase diagram of Anthamatten and Hammond calculated according their free energy model of asymmetry in side-chain LC diblock copolymers [35] in the case of planar anchoring of mesogens with respect to the domain-dividing surface, (Chapter 3). In addition, the experimental results of several groups are plotted (those of the Hammond group as well as of the groups of Ober and Thomas, Fischer, and Ikkala). The data for the here regarded PSLC block copolymers are represented by red symbols.

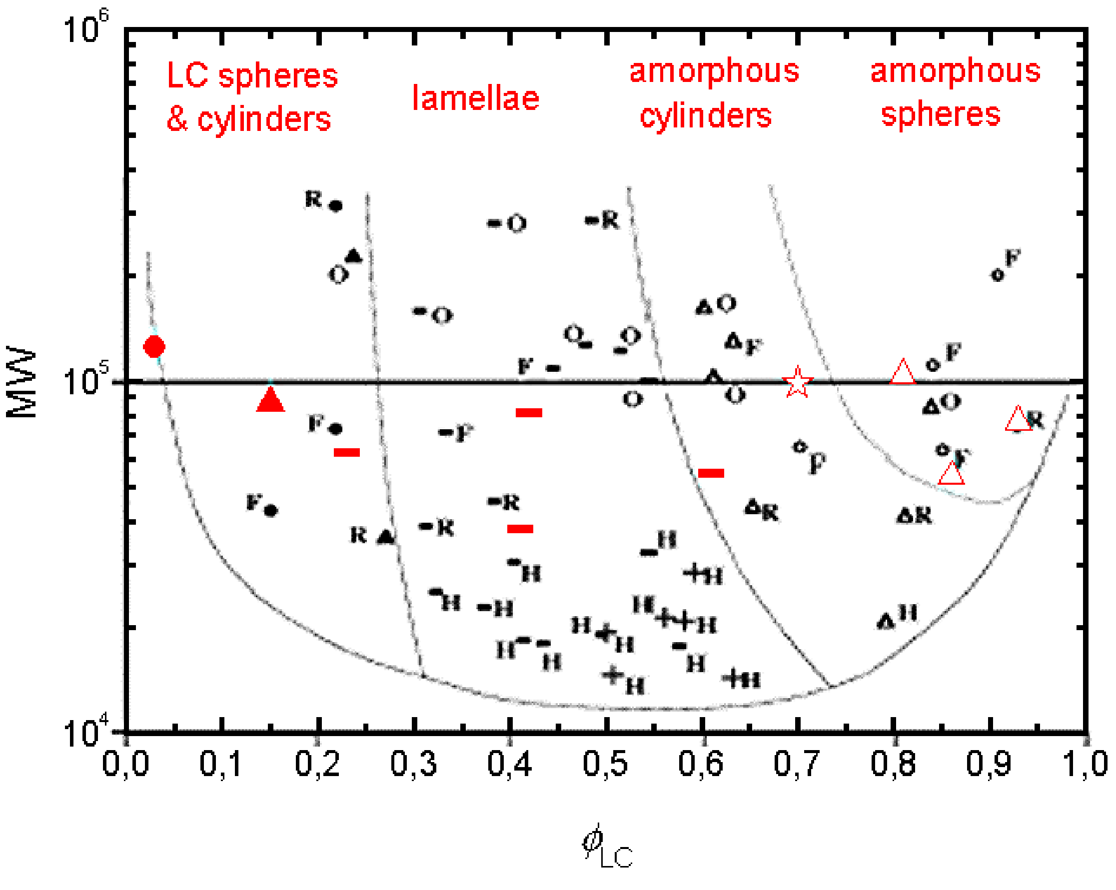

Figure 5.22. The phase diagram of the PSLC block copolymers investigated in this thesis (the red symbols) compared with the theoretical phase diagram of Anthamatten and Hammond for planar-anchored mesogens and the experimental data obtained from other authors (Hammond [34, 112], Ober and Thomas [38, 39], Fischer [40, 113], and Ikkala [8]). Observed morphologies are indicated as follows: full circles– LC spheres, full triangles– LC cylinders, lines– lamellae, pluses– partially defected or perforated lamellae, empty triangles– amorphous cylinders and the empty circles- amorphous spheres. (The red triangle at $\phi_{LC} = 0.93$ coincides with a circle, denoting a spherical morphology for the data obtained by Ikkala).

One can see that for the PSLC investigated in this thesis the lamellar interval broadens over the theoretically calculated lines and the interval of amorphous cylinders shifts to the area where bcc spheres are expected. In consistence with these results, the group of Ober and Thomas observed also cylindrical amorphous microdomains instead the predicted spherical ones for LC/I block copolymers with an azobenzene containing smectic A LC block [38]. However, the lamellar interval remains within the theoretically calculated borders. In addition, they obtained bicontinuous structure at $\phi_{LC} \sim 0.28$. The reported in [39] data for LC/I block copolymers with a chiral smectic C* LC block, fit within the theoretically calculated frames. The group of Fischer investigated PS-*b*-ChEMA block copolymers with a cholesteryl mesogen [40]. The data fit relatively well to the theoretical model with exception of the broadening of bcc structures on the expense of the cylindrical ones. They do not observe LC cylinder phase, but rather a direct transition from lamellar to spherical morphology. This result is contrary to the results for here presented PSLC block copolymers, where the cylindrical morphology is preferred over the spherical one in the similar molecular weight range. The difference is most probably due to the strongly nonlinear architecture of the ChEMA mesogen, which does not fit to the symmetry of the cylindrical geometry. In addition, Fischer *et* al. observed a different LC phase within the spheres and lamellae structures- nematic and smectic A, correspondingly. The layered smectic LC phase changes to the less ordered nematic one in order to fit to the symmetry of the microphase separated structure. The data of Ikalla [8] for PS-poly(4-vinylpyridine) block copolymers with hydrogen-bonded *4-n*-$C_{19}H_{39}C_6H_4$-OH (NDP) mesogens fit perfectly to the theoretically predicted model of Anthamatten and Hammond. They attend structures with higher curvature compared to the data in this thesis at comparable volume fractions. The relatively flexible NDP mesogens can adapt more easily to the curved domain dividing surfaces than the covalently bonded cyanobiphenyl mesogen. The experimental data of the Hammond group coincide as well with the theoretically predicted morphologies. In addition to the conventional structures, they observed morphologies with cylindrical defects within the lamellar phase. On heating above the isotropisation temperature, the mixed structure undergoes an OOT to the pure lamellar phase. This behaviour is contrary to the conventional observation that the OOT, triggered by the isotropisation temperature T_i goes from structure with low curvature to structure with higher curvature [41, 42]. The theoretically calculated phase diagram for planar anchoring of mesogens in [35] also show that above T_i, there is possible to occur OOT from domain morphologies with lower curvature to domain morphology with higher curvature (see

Figure 3.7). However, these effects cannot bring the phase diagram closer to that of the I/I block copolymers. The phase diagram remains strongly asymmetric also above T_i although the nematic elastic energy is excluded from the energy balance. The OOT occurrence depends also on the order parameter of the backbone S_B. It can occur only down to the certain $|S_B|$ value (Figure 3.7). Since each point in the phase diagram of one component block copolymer systems represent a separate block copolymer and means separate synthesis (hence no real fine tuning of the block volume faction is possible), the above discussion suggests that only a small room is left for the synthesized block copolymer where it has to be luckily located in order to undergo OOT. This readily explains why until now only few OOT has been reported [36, 41, 42].

5.3. Dielectric relaxation in PSLC block copolymers

The molecular dynamics of the LC block in bulk and in confined medium was studied by dielectric spectroscopy. The dielectric spectra of the LC homopolymer and the PSLC block copolymers were measured in the frequency range from 10^{-2} Hz to 10^{8} Hz within the temperature interval of –150 °C to 160 °C. Two segmental dynamics processes – δ- and α- as well as two local processes – β- and γ- were observed (see Chapter 4.2).

The segmental dynamics will be presented in the first section of this chapter. The local dynamics will be regarded in the second section. As we have seen in the chapter 5.2, the PSLC block copolymers are microphase separated and depending on the volume fraction, form PS microdomains in a LC matrix or LC microdomains in PS matrix. In order to compare the dynamics in a confined geometry with dynamics in the bulk state, the dielectric properties of the LC homopolymer and the LC block will be described separately as a matrix on one side and that of nanoscale confined LC block on the other.

The dielectric properties of bulk PS are well described in literature [114]. PS displays a typical α- relaxation with very small relaxation strength. The maximum value for the loss part of the dielectric function is $\varepsilon''_{max} \leq 0.01$. In comparison to that the intensity of the dielectric processes related to the LC block are much stronger. Depending on the volume fraction of the LC block the ε''_{max} varies between 2 and 0.1. The α- relaxation of the PS block is therefore hardly discernible in the spectra and will not be regarded in this work.

5.3.1. Segmental dynamics in LC

Dielectric relaxation in LC homopolymer and LC matrix

Figure 5.23 shows the dielectric spectra of the LC homopolymer for various temperatures. Each curve was measured with two different equipments (described in Chapter 4.2.3) – a frequency response analyser (for frequencies up to 4.10^{5} Hz) and coaxial line reflectometer (for frequencies from 1.10^{6} Hz up to 2.10^{8} Hz). Data between 4.10^{5} Hz and 1.10^{6} Hz were not collected, because they lie outside the measurable range.

One can distinguish in Figure 5.23 two main relaxation processes below T_i – α- and δ-segmental relaxation. The two processes overlap above T_i. The same behaviour is found in literature for other SCLC polymers [74, 115]. The lower frequency process is determined as a δ- relaxation and the higher frequency process– as a α-relaxation. It can be seen in Figure 5.23 that at 40° C an additional relaxation process appears at high frequencies. This process (namely β- relaxation) has a local origin and will be discussed in section 5.3.2.

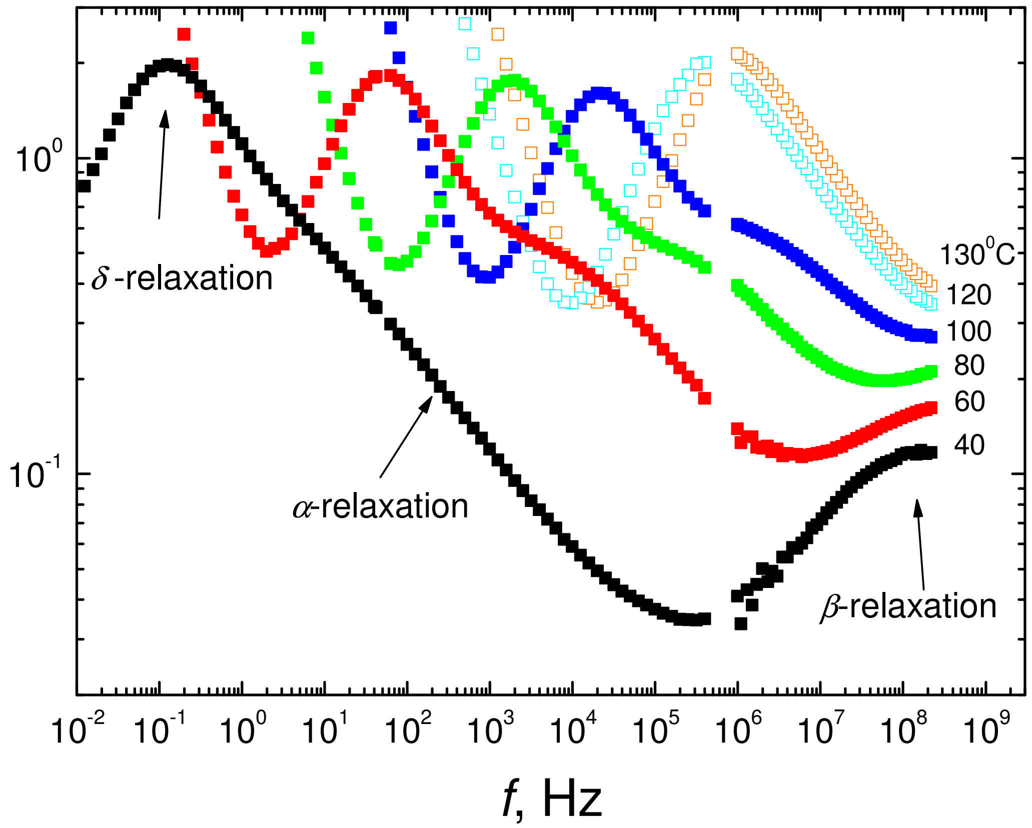

Figure 5.23. Dielectric spectra for the LC homopolymer at several temperatures as indicated in LC (solid symbols) and isotropic (open symbols) state.

The isothermal data of the dielectric losses ε'' were fitted to a superposition of two Havriliak-Negami (HN) functions and a conductivity contribution (see Chapter 4.2.1, Eq.4.47). The conductivity contribution appears at low frequencies. It is caused by the migration of free charges in the sample.

The high frequency α- relaxation is characterized by a very broad and asymmetrical regime of dielectric loss factor. In contrast to the α- process, the low frequency δ-relaxation has a narrow and symmetrical dielectric loss curve. Therefore we have used the HN function with $\gamma_k = 1$ (i.e. the symmetrical Cole-Cole equation, see chapter 4.2, Eq. 4.43) for the δ-relaxation relaxation in the fit routine. In this way, the number of variable parameters in the fitting process is reduced and hence the fit stability increases.

The fitting curves are calculated using a nonlinear least squares algorithm with the help of the "Origin 6.1 G" program (OriginLab Corporation (formerly Microcal Software)). The fit routine provides stable results for the relaxation times for the α and δ processes. The accuracy in the determination was generally better than 5% and 15%, respectively. We can see in Figure 5.24, an example of the fitting results for the LC homopolymer at T=50°C. This is seen that at this temperature the δ- and α- relaxation can be nicely separated. The fit gives as a result the relaxation time τ, the relaxation strength $\Delta\varepsilon$, and shape parameters α_k for both processes and in addition γ_k for the asymmetrical α- relaxation.

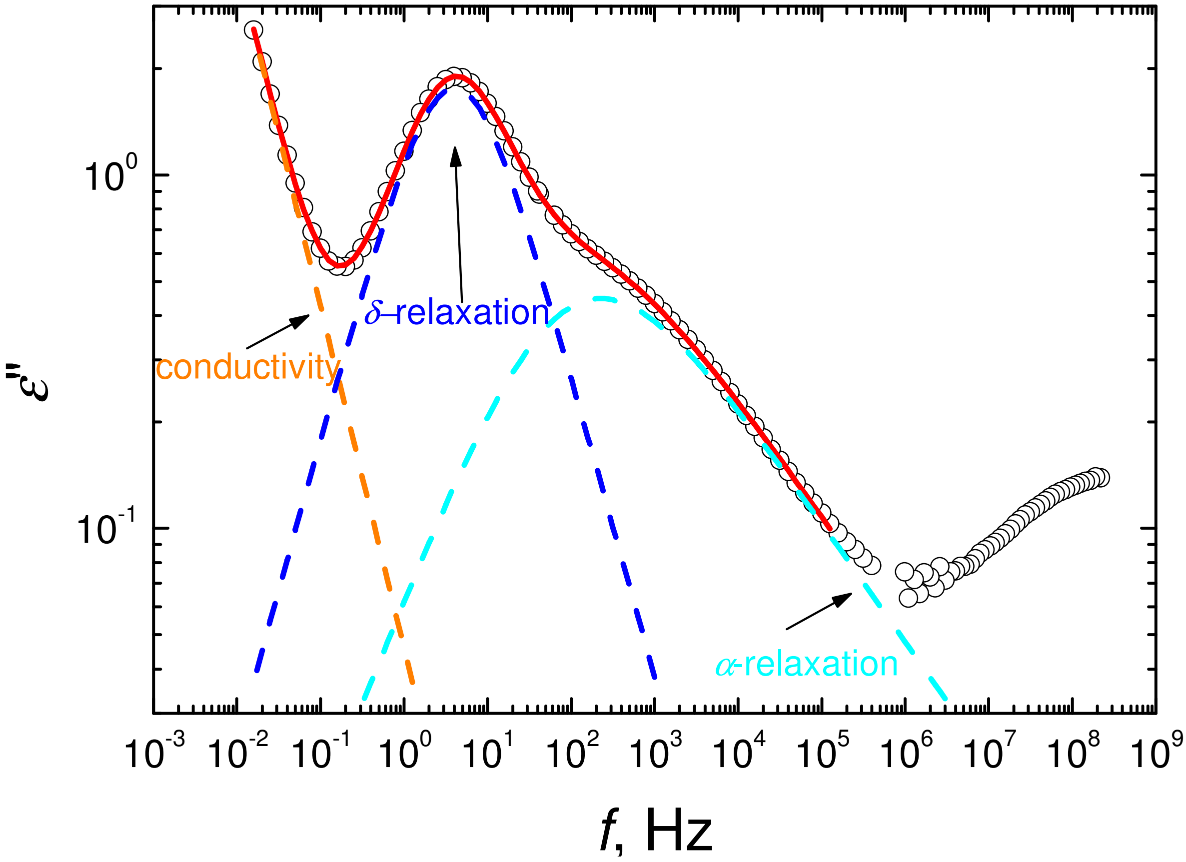

Figure 5.24. An example of the fitting results for the polymer LC homopolymer at 50.0°C. The solid line is the sum of the three curves shown by the dashed lines: α relaxation ($\Delta\varepsilon$=2.19±0.10; α=0.59±0.04; γ=0.58±0.06; τ=(1.71±0.12)×10^{-3}s), δ relaxation ($\Delta\varepsilon$=4.44±0.10; α=0.87±0.01; γ=1.00; τ=(4.24±0.05)×10^{-2}s) and conductivity contribution (σ/ε_0=0.22±0.01; s=0.92±0.01).

The dependence of the relaxation time on the temperature in Arrhenius coordinates for α- and δ- relaxations is displayed in Figure 5.25. One can see that it is strongly non-linear for both α- and δ- processes. In such a case, the phenomenological Vogel-Fulcher-Tammann (VFT) equation can be applied as a fitting function:

$$\tau = A\exp(\frac{B}{T - T_V}) \tag{5.2}$$

where τ is the relaxation time; A, B and T_V are the VFT parameters. The constant A is the limiting value for the relaxation time at $T \to \infty$, T_V is called the Vogel temperature, which is usually found to be 30-50°C lower than T_g, and B is an activation parameter.

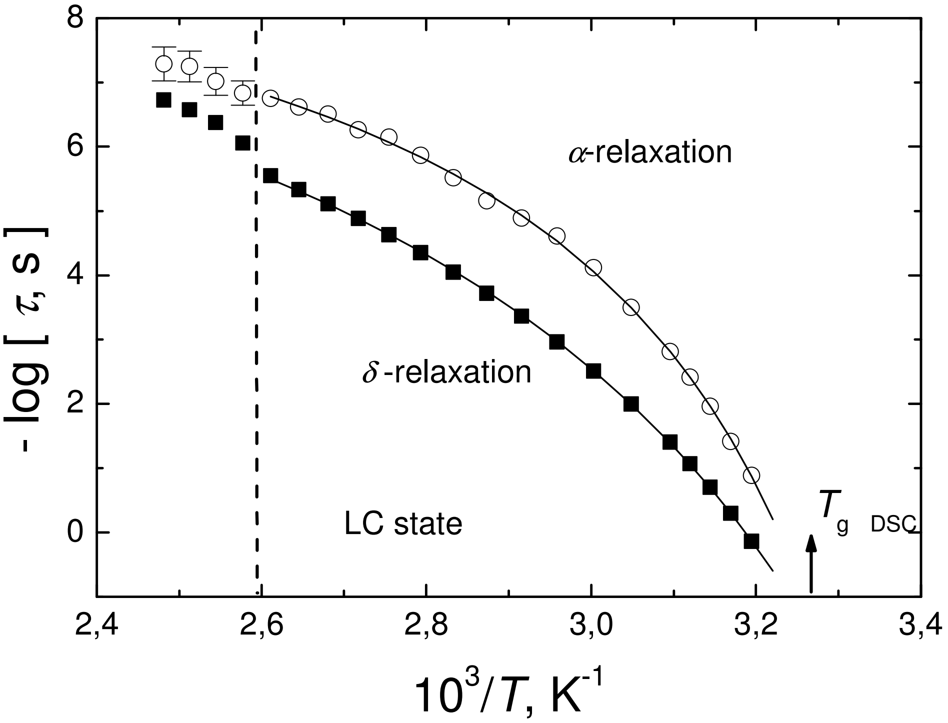

Figure 5.25. The relaxation time of both cooperative processes versus inverse temperature for the LC homopolymer. Lines are the fits of the VFT function to the data. The vertical dashed line marks the nematic-to-isotropic transition. The arrow indicates the glass transition temperature T_g as determined by DSC.

The calculated according to the Eq. 5.2 VFT parameters are presented in Table 5.3. The dynamic glass transition temperature (Tg_{DIEL}) is also given in Table 5.3. Tg_{DIEL} can be defined as the temperature of maximum loss at selected frequency (or relaxation time) [116]. Here it was determined at relaxation time τ equal to 10 s (Eq. 5.2).

Table 5.3. The VFT parameters for α and δ process of the LC block in the various types of microphase separated structures (see chapter 5.1).

Sample	δ				α			
	Ax10^{10},s	B, K	Tv, K	Tg_{DIEL},°C	Ax10^{10}, s	B, K	Tv, K	Tg_{DIEL},°C
Homopolymer								
LC homopolymer	0.82	1340	256	35	1.49	750	277	34
	(±0.12)	(±30)	(±1)		(±0.50)	(±30)	(±1)	
LC matrix								
PSLC 7/93	0.97	1320	257	36	3.20	680	279	34.0
	(±0.25)	(±40)	(±1)		(±0.86)	(±30)	(±1)	
PSLC 14/86	0.91	1340	257	37	2.75	680	279	34
	(±0.25)	(±50)	(±1)		(±0.42)	(±20)	(±1)	
PSLC 19/81	0.93	1340	257	37	3.55	670	281	34
	(±0.18)	(±40)	(±1)		(±0.60)	(±30)	(±1)	
PSLC 30/70	0.87	1340	257	37	5.63	630	281	35
	(±0.25)	(±50)	(±1)		(±1.5)	(±30)	(±1)	
Lamellae structure (LC thin films, 1D confined)								
PSLC 39/61	0.56	1390	256	37	1.25	770	276	34
	(±0.21)	(±60)	(±2)		(±0.42)	(±30)	(±1)	
PSLC 59/41	1.91	1600	249	36	0.82	840	273	32
	(±1.02)	(±90)	(±2)		(±0.17)	(±30)	(±1)	
PSLC 77/23	4.86	1460	252	35	1.70	750	275	32
	(±1.20)	(±70)	(±2)		(±0.56)	(±40)	(±2)	
Cylindrical structure (LC microdomain, 2D confined)								
PSLC 85/15	2.88	1600	245	32	1.16	790	271	29
	(±2.03)	(±100)	(±3)		(±0.47)	(±50)	(±2)	

There are different theories in literature about the physical origin of δ- and α- processes [86, 115, 117, 118, 119]. There is not an up-to-date unique understanding of the underlying microscopical dynamics.

The δ- relaxation is mostly described in literature as caused by cooperative rotation of the side-groups around the short side-chain axis (movement around angle β in Figure 4.13) [74, 86, 120]. (Most likely, this motion is moreover a multistep process than a 180° flip-flop jump of the mesogen [86, 120]). This occurs at low frequencies and has large relaxation strength which depends on the longitudinal component of the side-group dipole moment [74]. This corresponds to the $F_{//}^{l}(\omega)$ mode in equation 4.58 (see Figure 4.14). The δ- relaxation displays a narrow relaxation time distribution and non-linear behaviour in Arrhenius coordinates.

The low frequency mode in Figure 5.23 and Figure 5.24 possess the all characteristic features described above. Therefore, it was unambiguously recognized as δ- relaxation. A schematic picture representing the possible relaxation processes in the present LC block is drawn in Figure 5.26. The δ- relaxation (as shown by the dark blue colour) follows the above described model.

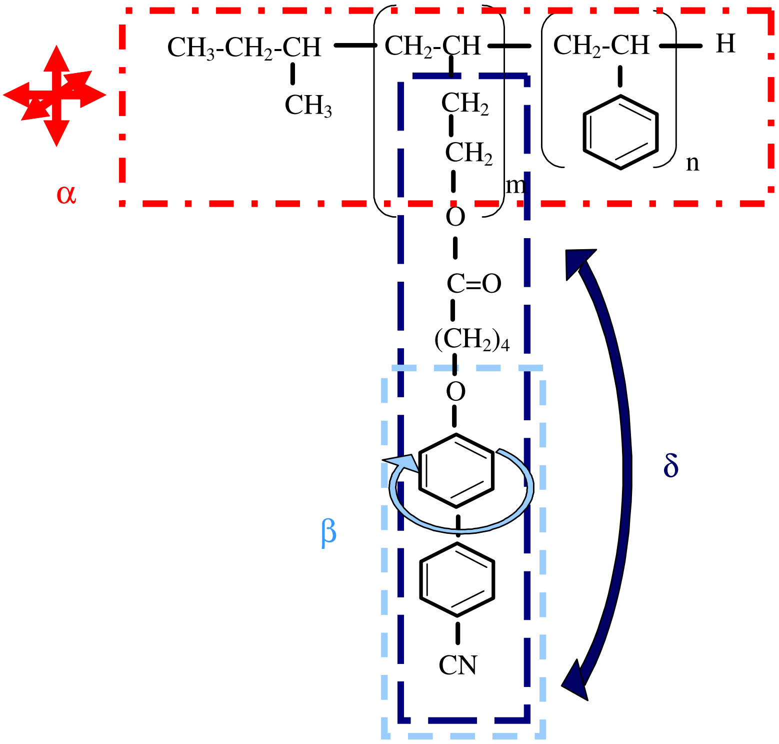

Figure 5.26. The scheme of the relaxation processes in the LC block.

The α-relaxation in side-chain LC polymers appears at higher frequencies than the δ-relaxation. α-relaxation was assigned to the micro-Brownian motions of segments in the polymer main chain (Figure 5.26). The α-relaxation is observed in glass forming systems [86, 116] and is connected with the dynamic glass transition in amorphous polymers. In most cases the appearance of this process coincides with the glass transition temperature of the polymer which is determined by calorimetry. Thermally stimulated discharge currents (TSDC) experiments also confirm its assignment to the segmental motion, especially for LC polymers containing a cyanobiphenyl mesogen [121-123], i.e. systems similar to those investigated in the present work. The dependence of the relaxation time τ_α on the temperature in Arrhenius coordinates is strongly non-linear.

The second relaxation process in Figure 5.23 and Figure 5.24 appears only above the LC glass transition temperature. It has a non-linear behaviour in Arrhenius coordinates (Figure 5.25). Therefore it could be unambiguously distinguished as α-relaxation.

A normal mode relaxation [86] can not be observed in the regarded LC blocks because the end-to-end vector of the main chain does not have a dipole moment.

Let us now regard the molecular dynamics in the LC matrix. As we have already seen in chapter 5.2, the samples PSLC 7/93, PSLC 14/86 and PSLC 19/81 consist of PS cylinders embedded in the LC matrix. Figure 5.27 shows the dielectric spectra for LC homopolymer, PSLC 7/95, PSLC 14/85 and PSLC 19/81 at temperature T=60°C. The dielectric relaxation of the LC blocks of these copolymers is similar to this of the LC homopolymer. In this case, the δ- and α- relaxation peaks are slightly shifted to lower frequencies. This means that both cooperative modes of the LC block become slower, i.e. the glass transition temperature $T_{\mathrm{g\ DIEL}}$ increases in the block copolymer matrix. The VFT parameters for both cooperative modes and the calculated $T_{\mathrm{g\ DIEL}}$ values are given in the Table 5.3.

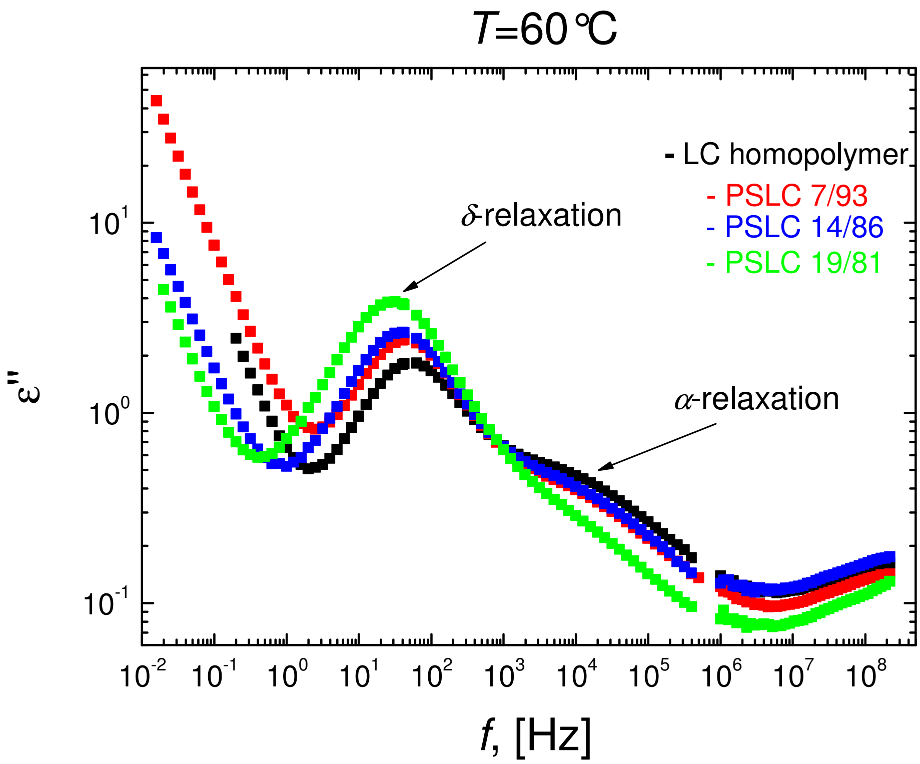

Figure 5.27. The dielectric spectra for the LC homopolymer, PSLC 7/95, PSLC 14/85 and PSLC 19/81 at temperature T=60°C.

Dielectric relaxation of Nano-Scale Confined LC Blocks

In the samples PSLC 39/61, PSLC 59/41, PSLC 77/23, PSLC 85/15 and PSLC 97/3 the LC blocks all form nanodomains embedded in PS matrix (see chapter 5.2). The first three samples have 1D confined layered structure, which could be considered as analogue of thin film [70]. The thicknesses of the LC layer are 21, 11 and 11nm respectively (see chapter 5.2). For PSLC 85/15 the LC blocks are confined in cylindrical domains with diameter of 13.2 nm (2D confinement). The LC block in the sample PSLC 97/3 forms spherical domains (3D confinement). Because of the low LC volume fraction in PSLC 97/3, the dielectric loss function is hardly discernible in the spectra. A very broad relaxation regime is observed and the both α- and δ- processes can not be separated by a fitting procedure. Therefore, this sample will be not regarded further.

Figure 5.28 displays the dielectric spectra for PSLC 59/41 recorded in the temperature range around the nematic-to-isotropic transition. One can see that similar to the LC homopolymer and the LC matrix, the LC domains show clear α- and δ- relaxation. The analysis of these data is done as described above. The results are summarized in Table 5.3

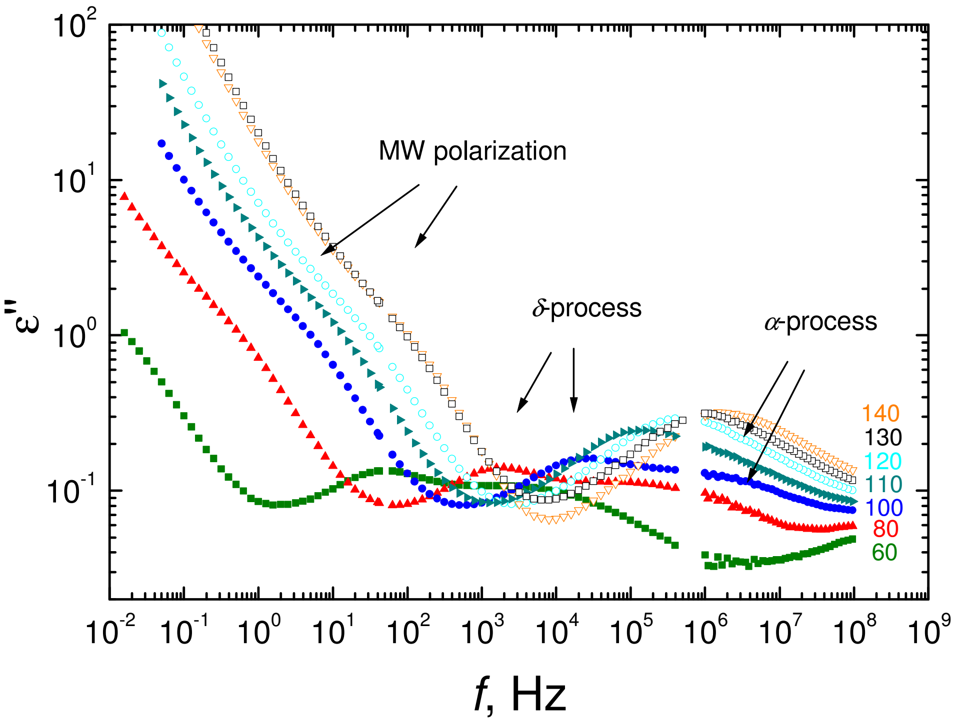

Figure 5.28. Dielectric spectra for the PSLC 59/41 at different temperatures: in LC (solid symbols) and isotropic (open symbols) states.

and Figure 5.29. One can see in Table 5.3 that the confined LC block reveal a faster cooperative motion near the glass transition in comparison to the LC matrix (the glass transition temperature T_{gDIEL} is decreased).

One can see in Figure 5.28 that at low frequencies in addition to the δ- and α- processes a new relaxation process with high relaxation strength is observed. The relaxation time τ_{MW} for this process is by ~4 orders of magnitude larger than the relaxation times of the α- and δ- relaxations. Keeping in mind that the block copolymers are heterogeneous systems, we can assign this process to the Maxwell-Wagner (MW) polarization (see Chapter 4.3, Eq. 4.60-4.64). The Eq. 4.63 can be applied for calculation of τ_{MW} in the samples with lamellae structure (PSLC 59/41 and PSLC 77/23) [70]. In the calculations are used data for PS published earlier (ε'_1(T), σ_1(T) [114]) and the present results for LC homopolymer (ε'_2(T), σ_2(T) and layer thicknesses d_{LC}(T) and d_{PS}(T)). The calculated values of τ_{MW} for PSLC 59/41 [70] are show in Figure 5.29 as a function of the inverse temperature. These deviate slightly from the experimental data. Such deviations between theoretical and experimental values may be caused by the uncertainty in the determination of the conductivity of the PS (σ_1) and LC (σ_2) layers in the copolymers.

For the composition PSLC 39/61, it was impossible to extract clearly MW relaxation due to the high conductivity of the sample.

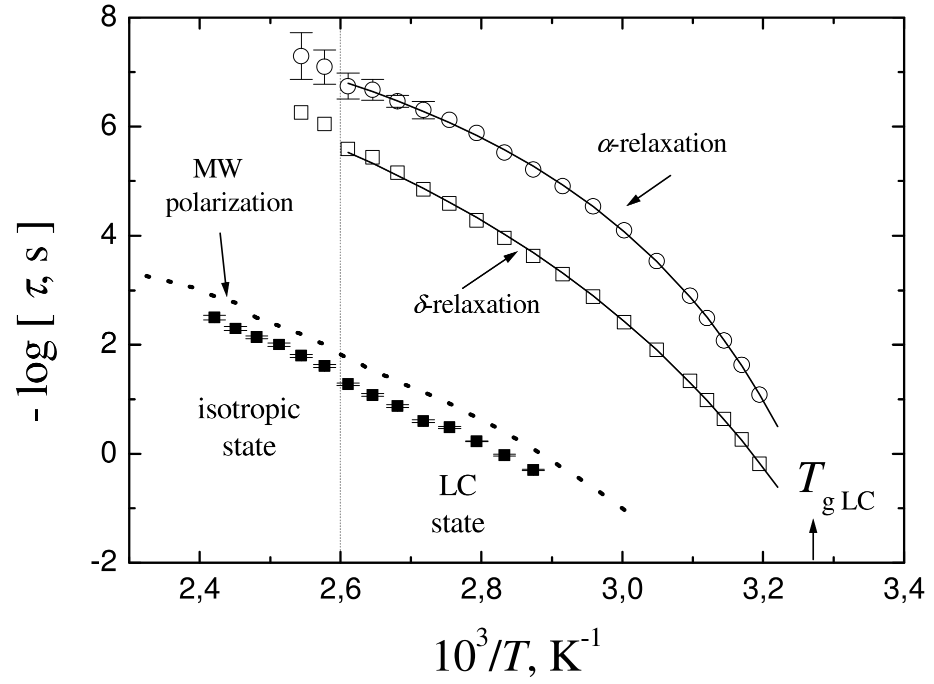

Figure 5.29. The relaxation time of the cooperative and MW processes versus the inverse temperature for the sample PSLC 59/41. The dashed line is calculated according to Eq. (4.63). The vertical line denotes the nematic-to-isotropic transition inside the LC microdomains.

Dependence of segmental dynamic parameters on spatial confinement

In order to investigate the influence of the spatial confinement on the molecular dynamics, we will regard the variation of the relaxation time τ, the dynamic glass temperature T_{gDIEL}, and the shape parameters m and n of the dielectric loss function with temperature.

Figure 5.30 shows the relaxation time τ of the cooperative processes at T=40°C vs. the PS volume fraction ϕ_{PS}. One can see that the α- and δ- relaxations are dynamically coupled [124], i.e. the relaxation times τ_α and τ_δ vary with the composition in the same way. The dynamic glass transition temperature T_{gDIEL} for the both processes is nearly the same [125] (see Table 5.3). The frequency-temperature location of both processes in an Arrhenius plot is influenced by the main chain rigidity of LC macromolecule [70]. Recently Zhukov et al. [124] have shown that the gradual increase of the backbone rigidity of the functionalized LC copolymer causes a parallel slowdown of the reorientation rates of both processes. This means that the change of the backbone rigidity influence not only the dynamic glass transition (α- process) but also the side-chain segmental dynamics (δ- process). Such behaviour could be explained with the fact that the one of the LC side-chain ends is fixed by a covalent bond to the backbone and they cannot move independently of each other. This explains the partial parallelism of the temperature and the pressure dependencies of the α- and δ- process within the LC mesophase [74]. On the other hand, the relaxation time of α- process is also influenced by the δ-relaxation. The relaxation time τ_α decreases with increasing of the main-chain – side-chain separation (increasing the spacer length) [86]. In the present work was found that the relaxation times of the α- and δ- process are related by a factor which changes slightly with the mesostructure variation, although the absolute values of relaxation time can vary considerably.

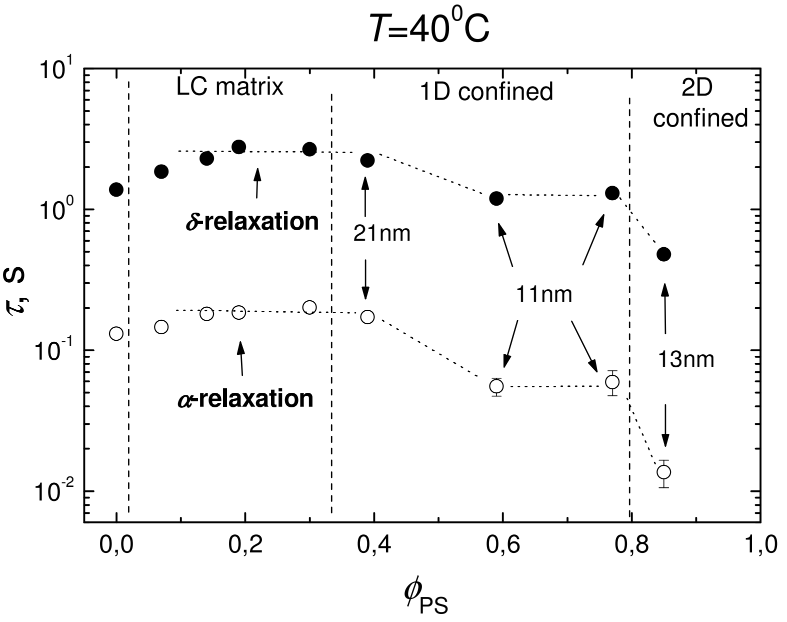

Figure 5.30. The relaxation time of the cooperative processes of the LC block at 40°C as a function of PS volume fraction. The vertical dashed lines separate approximately the different mesophase structures (see table 5.2).

Figure 5.31 shows the relaxation time of the cooperative processes at T=130°C versus the PS volume fraction. This temperature was chosen to be above the PS glass transition It is also above the nematic-to-isotropic transition temperature T_i of the LC block with the highest T_i, in order to be sure that all the samples are regarded in the same state (the T_i varies in the interval 112-127°C). In Figure 5.28 it is evident, that at temperatures above 110°C the peaks corresponding to the δ- and α- processes merge. It is, thus, hard to distinguish between them and they are fitted as one peak using a Fuoss-Kirkwood function (Equation 4.46). The Fuoss-Kirkwood function was chosen as the one which gives the best fitting results among the functions, represented by Equations 4.43-4.46.

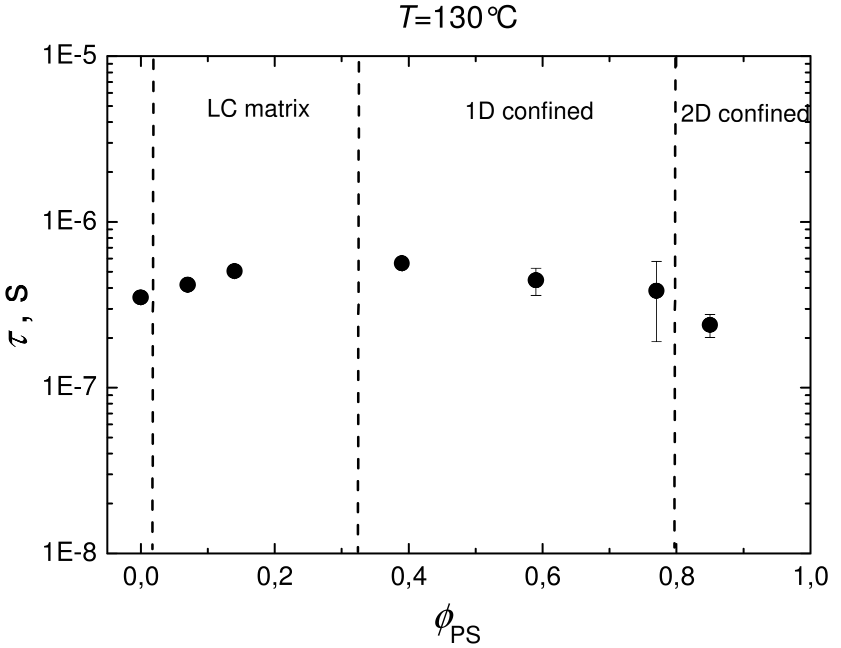

Figure 5.31. The relaxation time of the merged α and δ cooperative processes in LC block at 130°C as function of the PS volume fraction. The vertical dashed lines separate approximately the different mesophase structures (see table 5.2).

Let us first compare the relaxation time in the LC homopolymer with the relaxation time in the LC matrix. One can see in Figure 5.30 that the relaxation time increases up to factor of 2 in the LC matrix relative to the LC homopolymer. This increase of the relaxation time could be explained by the block copolymer structure. Two blocks with different molecular dynamic are connected by a covalent bond. Therefore, one may expect that the relaxation processes, which they show are mutually dependent. At T=40°, the PS block is in glassy state (T_{gPS}~100°C) and it is completely immobile. As a result the segmental dynamics in LC block is partly suppressed. This gives rise to a slowdown of the α- process and consequently to the δ- process due to the strong dynamical coupling between them.

One can see in Figure 5.31 that even above the PS glass transition the relaxation time of the merged $\delta\alpha$-process increases when moving from the LC homopolymer to the matrix. In this case, the factor is slightly lower than 2 (about 1.5), but the effect still exists. It could be explained with the different dynamics of the two blocks, connected by a covalent bond– the relaxation of the PS block is much slower compared to the relaxation of the LC block.

An additional reason for the relaxation time difference between the LC homopolymer and LC matrix may be the different chain conformation in the block copolymer compared with the homopolymer [126]. As explained earlier, the chain conformation in the block copolymer is more stretched in comparison with the homopolymer. This may influence the relaxation time.

The same effect of slowing down the segmental dynamic when moving from homopolymer to block copolymer in microphase separated state was reported in literature. It has been shown that the retardation factor for the polyisoprene to polystyrene-polyisoprene [92, 126, 127] and polyoxybutylene to polyoxyethylene-polyoxybutylene [88] is of the order of 2-4 in a broad range of composition (volume fraction in the interval 0.16-0.65). A similar magnitude of retardation of the segmental mode (1.5-2) is obtained for the "LC matrix" block copolymers studied in the present work: PSLC 14/86 PSLC 19/81 and PSLC 30/70 (see Figure 5.30 and Figure 5.31).

As we have seen in Chapter 5.2 further increasing of the PS volume fraction (ϕ_{PS}>30), leads to the structures in which the LC blocks are confined in the PS matrix. The sample PSLC 39/61 contains LC layers of thickness of 21nm. This sample has the same relaxation times as the LC matrix. As the confinement length decreases further to 11nm (PSLC 59/41 and PSLC 77/23) the relaxation time decreases in comparison with these of the LC matrix and LC homopolymer. The decrease in τ is more pronounced for PSLC 85/15 which exhibits 2D confinement (cylindrical LC domains). The relaxation time at T=40°C (Figure 5.30) varies with more than one order of magnitude for each cooperative mode. The influence of the dimension of the confinement (1D or 2D) may be explained by the different order of the chains within the 1D and 2D domains– nearly parallel in the lamellae and radial in the cylinders. This leads to different steric interactions, which may influence the relaxation time.

The relaxation time above T_i (Figure 5.31) shows similar behaviour. However, the difference in τ, going from 21 nm to 11 nm thick layer is not as high as this at T=40°C, i.e. the critical length d_{cr} may be lower for temperatures above T_i. The eventual decreasing of d_{cr} may be explained with the change of the cooperativity length above the nematic-to-isotropic transition, caused by change of the chain conformation. The deviation of the LC chains from the Gaussian coil is caused by two complementary effects. The chain is stretched due to microphase separation as well as due to the presence of the nematic field. As can be seen from the Figure 5.18, above the T_i the chain stretching slightly decreases as a result of the clearing of the nematic field. If the cooperativity length decreases with decreasing the stretching, it means that it is smaller at T=130°C than at T=40°C. Hence, the influence of the confinement on the relaxation time should be weaker at T=130° C than at T=40°C as it was observed.

Similar results are reported in literature for the cooperative dynamics near the glass transition in restricted geometries for the low molecular weight glass-forming liquids [43-49] and in thin polymer films [50, 51, 55, 58-65]. Recently Fukao and Miyamoto [51] have shown that the dielectric relaxation time of the segmental mode in thin PS films does not change down to one critical length d_{cr}. Below d_{cr} it decreases drastically with decreasing the thickness. Moreover, the d_{cr} increases with the molecular weight and is apparently related to the radius of gyration of the polymer chains (for PS d_{cr}=11nm for $M_{\mathrm{W}}=2{,}8\times10^5$ and d_{cr}=22nm for $M_{\mathrm{W}}=1{,}8\times10^6$).

In the present work, the thickness of the LC layer d_{LC} is directly connected with the molecular weight (see p.88-89), i.e. only one layer thickness corresponds to a certain M_{W}. Hence, it is relevant to consider the variation of the relaxation time with decreasing of M_{W} and correspondingly of the domain dimensions.

The relaxation time decreases with decrease of d_{LC} from 21 nm to 11nm (Figure 5.30). Then, we can assume that the critical length d_{cr} of the LC block is between 21 and 11nm. The 2D confinement in cylindrical domains introduces further decrease of the relaxation time. The diameter of the cylinder is 13 nm– higher than d_{LC} of the 1D confined LC block for PSLC 59/41 and PSLC 77/23. Therefore, the relaxation time is influenced also from the confinement dimension.

Now we will consider the variation in dynamic glass transition temperature of the LC block – $T_{\mathrm{g,DIEL.}}$ As was mentioned above, the α- process is strongly connected to the glass transition and it cannot be detected in the glassy state. The $T_{\mathrm{g,DIEL}}$ values for all samples are presented in Table 5.3. This data does not vary strongly with the confinement. The $T_{g\mathrm{DIEL}}$ for 13 nm 2D confined samples is only 5°C lower than $T_{g\mathrm{DIEL}}$ of the LC matrix and homopolymer. There are some reports in literature about the T_{g} variation in thin PS films with decreasing the film thickness [58, 59]. It was found that the T_g values for the PS thin films on substrate were lower than the bulk values for films with thickness less than 40nm [58]. The total T_{g} reduction for a film of thickness 20 nm was ~10°C, whereas the freely standing PS film with the same thickness exhibited ~70°C reduction of T_{g} [59]. These results reveal that the glass transition temperature T_{g} is strongly influenced by the presence of free surface in the thin polymer film. The LC block studied in this work is connected by a covalent bond to the PS block, which has much higher glass transition temperature.

According to these circumstances, one should expect increasing of T_g, but it decreases. The decreasing could be an effect, caused from the spatial constraint. However the changes are much weaker compared to the data for PS thin films on substrate [58].

The T_g reduction in the thin films was explained in literature by help of a two- or three-layer model [51, 62, 63, 65, 128]. The thin film was suggested to consist of two or three layers with different mobility and corresponding glass transition temperatures. These models suggested that near a free surface there exists a “liquid-like” layer, in which the molecular mobility is much higher than in bulk. Close to the substrate-polymer interface a so-called “bound” or “dead” layer is formed, where the mobility is considerably suppressed. In addition to this the three-layer model assumes the existence of the “bulk-like” phase between “liquid-like” and “dead” layers. This model implies also a broadening of the relaxation time distribution followed by the corresponding change of the shape of the dielectric spectra. The applicability of this model to the PSLC block copolymers, investigated in this thesis will be discussed later. First, we should regard the change of the shape of the dielectric loss function with the confinement.

The shape of the dielectric loss function reflects the relaxation time distribution – a broader peak corresponds to a broader relaxation time distribution. Generally, the shape of the dielectric loss function near a peak at $\omega{=}\omega_{\max}$ is characterized by two parameters m and n:

$$\begin{aligned} \varepsilon''(\omega) &\propto \omega^{m} \qquad (\omega \ll \omega_{\max}) \\ \varepsilon''(\omega) &\propto \omega^{-n} \qquad (\omega \gg \omega_{\max}) \end{aligned} \tag{5.3}$$

They are related to the Havriliak-Negami parameters in equation (4.47) by $m{=}\alpha_k$ and $n{=}(\alpha_k.\gamma_k)$. The parameter m corresponds to the low frequency relaxation time distribution and n– to the high frequency relaxation time distribution [129, 130]. There are contradicting observations on the influence of the spatial confinement on the relaxation time distribution. Some dielectric studies have shown that the α- process becomes broader in the confined state [43-49, 50-53, 65]. The broadening is caused by relatively immobile molecules close to the pore wall [43-49, 52, 53] or to the substrate [50, 51, 65]. In order to reduce the interaction forces between the investigated material and the pore wall the latest was treated chemically. It resulted in a slightly narrow relaxation time distribution [44, 49]. Some studies are done also for microphase separated block copolymers [88, 126, 127]. The segmental mode or α-process does not show any significant broadening in comparison to the homopolymer [88, 126]. However, it was found, that the normal mode of poly(oxybutylene) in poly(oxyethylene)- poly(oxybutylene) block copolymers [88] and the normal mode of polyisoprene in polyisoprene- polystyrene block copolymers broaden compared to the normal mode of the corresponding homopolymers [126, 127]. The broadening was explained as a consequence of the spatial confinement and thermodynamical confinement. Normal mode relaxation is proportional to the fluctuation of the end-to-end vector of the polymer chain and reflects the motion of the whole molecule, therefore is more sensitive to the conformation and the environment of the macromolecule than segmental modes [131]. Studies on free standing PS films by photon correlation spectroscopy have shown that the distribution of relaxation times of segmental mode for a film of thickness ~25 nm is the same as for bulk PS [132]. At the same time, T_g is 70° C lower than the bulk value. The dielectric study on thin films of cis-polyisoprene (thickness down to 22 nm) have shown that the segmental relaxation as well as the shape of relaxation peak are unaffected by the confinement [55]. These results suggest that for the both examples mentioned above the cooperativity length for the segmental motion is smaller than ~20 nm [70].

The values of the shape parameters m and n at 40°C for the α- relaxation are plotted in Figure 5.32. They were obtained from a fit of Eq.(4.47) to the data. Both parameters have values that are typical for the segmental mode of amorphous polymers [86] and do not vary within the experimental uncertainty over the range of composition studied. Hence, the distribution of the relaxation times for the α-relaxation is the same in the bulk and in the nano-confined samples. This means that we can not apply the layered model mentioned above to the here regarded PSLC block copolymers. These results are consistent with those for freely standing polymer films mentioned above [132].

Figure 5.33 represents the shape parameters m and n at 40° C for the δ- relaxation in the PSLC block copolymers and the LC homopolymer. The δ- relaxation shows symmetrical distribution, hence the parameter γ_k=1. This means that the both shape parameters have equal values, i.e. m=n. Compared to the α- relaxation, the shape parameters of the δ- process decrease with the reduction of the confinement length. The different behaviour of the relaxation time distribution for α- and δ-relaxation can be explained with the different cooperativity lengths for the both processes. The cooperativity length for the δ- relaxation is obviously larger than that of the segmental motion.

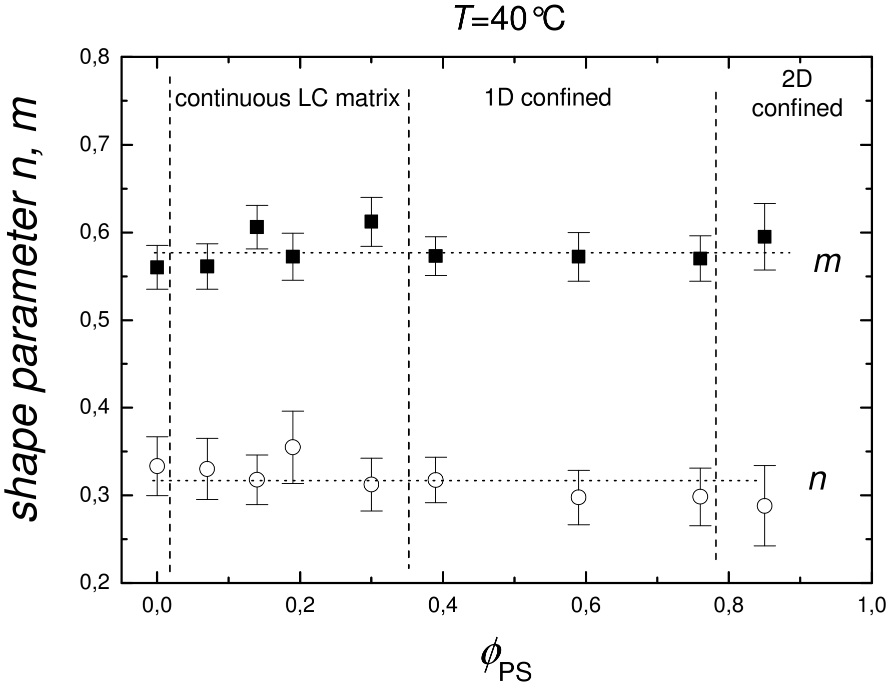

Figure 5.32. The α- relaxation shape parameters *m* and *n* at 40°C for different composition. The vertical dashed lines separate approximately the different mesophase structures (see Table 5.2).

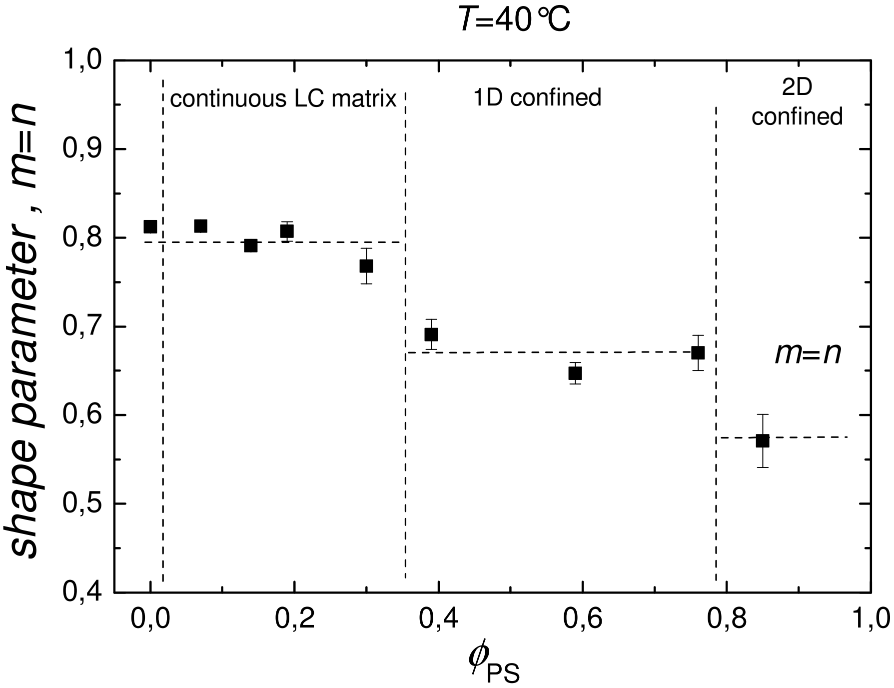

Figure 5.33. The δ- relaxation shape parameters *m* and *n* at 40°C for different composition. The vertical dash lines separate approximately the different mesophase structures (see Table 5.2).

In addition to the confinement effect, the segmental dynamics may be influenced also by several other factors, such as molecular weight, polymer backbone rigidity, spacer length, nature of the bridging group or terminal substitution. Here will be regarded only the molecular weight dependence, since the investigated copolymers have different LC main chain length. The other influencing factors are identical for all samples. According to literature data, the relaxation time of both cooperative modes of side-chain LC crystals increases with the molecular weight up to degree of polymerization 30-40 [133]. At higher degree of polymerization the cooperative dynamics does not depend on the main chain length. The here presented PSLC copolymers have degree of polymerization of the LC block between 42 and 250. Therefore the difference in molecular weights can not cause any significant changes in the relaxation times of both cooperative modes.

In conclusion, one can say that the α- and δ- relaxation parameters (with the exception of shape parameters for α- relaxation) vary with composition of the PSLC block copolymers. This variation is an indication of the confinement effect. The variation is less pronounced above T_i, i.e. it is influenced due to the nematic field.

5.3.2. Local dynamics

Figure 5.34 shows the dielectric spectra of the LC homopolymer at T=-85°C. One can see that in the glassy state two relaxation processes appear. The low frequency process is denoted as β-relaxation and the high frequency process- as γ-relaxation [71]. This behaviour is typical for side-chain liquid crystal polymers with a cyanobiphenyl mesogen connected to the backbone with a methylene spacer [124, 134].

The evaluation of the experimental data was done with the help of Havriliak-Negami equation (Eq. 4.47). The fitting procedure was explained in chapter 5.3.1. It was shown previously that the local modes of the side-chain LC polymers are well described by symmetric distribution of the relaxation times [117, 135]. Assuming a symmetrical shape of the loss curve also for here presented LC block, we performed all fits using fixed shape parameter γ_k=1. After that the fit routine provides stable results for the relaxation times of β- and γ-processes for all copolymers studied. The accuracy in the determination of Havriliak-Negami parameters was better than 10%. It can be seen in Figure 5.34 that at this temperature both relaxations are nicely separated. A good resolution of both processes was possible at temperatures below -50°C. At higher temperature they strongly overlap and their separation is more difficult.

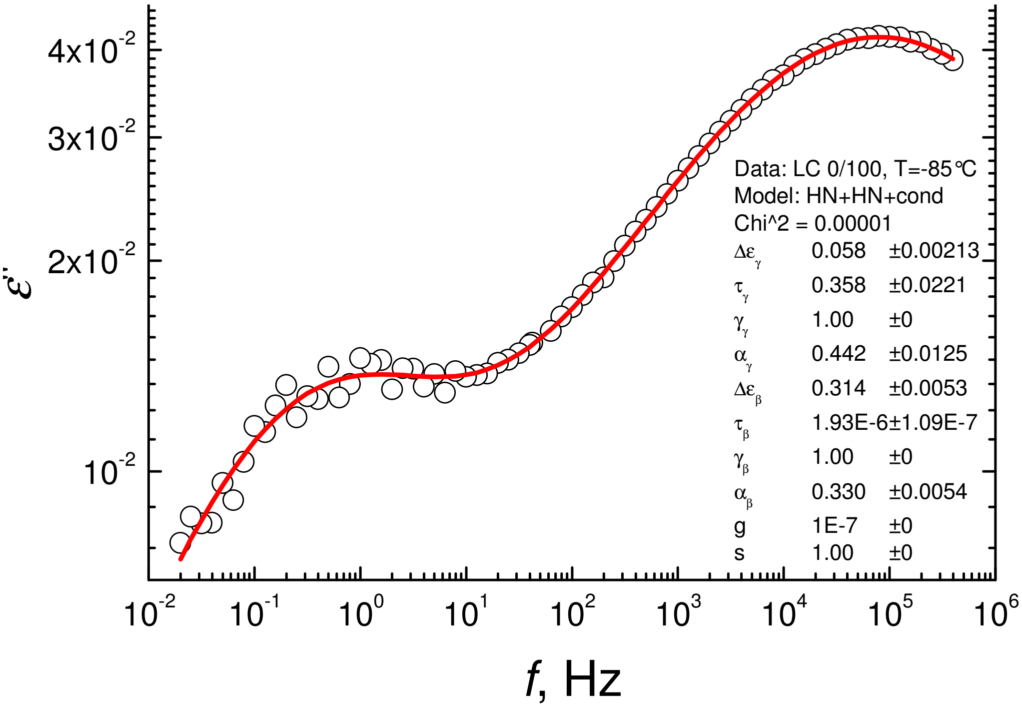

Figure 5.34. An example of fitting results for the LC homopolymer at T = - 85°C.

Figure 5.35 presents the dielectric loss for PSLC 14/86 at various low temperatures. The other PSLC copolymers show similar behaviour in this frequency-temperature window. The relaxation strengths of β- and γ-relaxations are proportional to the LC block content. Only in PSLC 97/3– the block copolymer with the lowest LC content it was impossible to resolve the β-process because of its very low intensity. Since the PS block does not have any relaxation of the dipole polarization at low temperatures, both processes are related to the LC block.

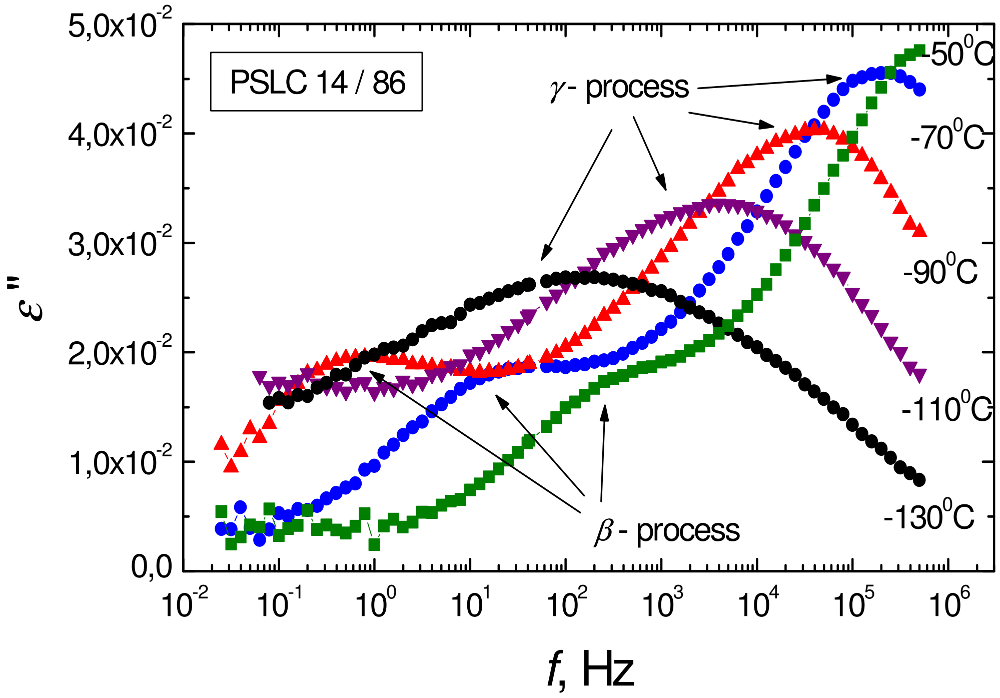

Figure 5.35. The dielectric spectra for PSLC 14 / 86 at different temperatures. The error bars are smaller than the size of the symbols.

Figure 5.36 displays the dependence of the relaxation time on the temperature in Arrhenius coordinates for β- and γ- relaxation processes for all copolymers and for the LC homopolymer. One can see in Figure 5.36 that the dependence of the relaxation time of β- and γ-processes on the temperature differs from these for α and δ- relaxations, shown above. The relaxation time of β- and γ-relaxation shows linear dependence in Arrhenius coordinates. The data are well described by the Arrhenius equation:

$$\tau = \tau_0 \exp(E_a / kT) \tag{5.4}$$

where τ_0 is a preexponential factor and E_a is the activation energy. The activation energies determined from the slopes of the linear fits in Figure 5.36 are $E_{a\beta}$~53 kJ/mol for the β-process and $E_{a\gamma}$~30 kJ/mol for the γ-process.

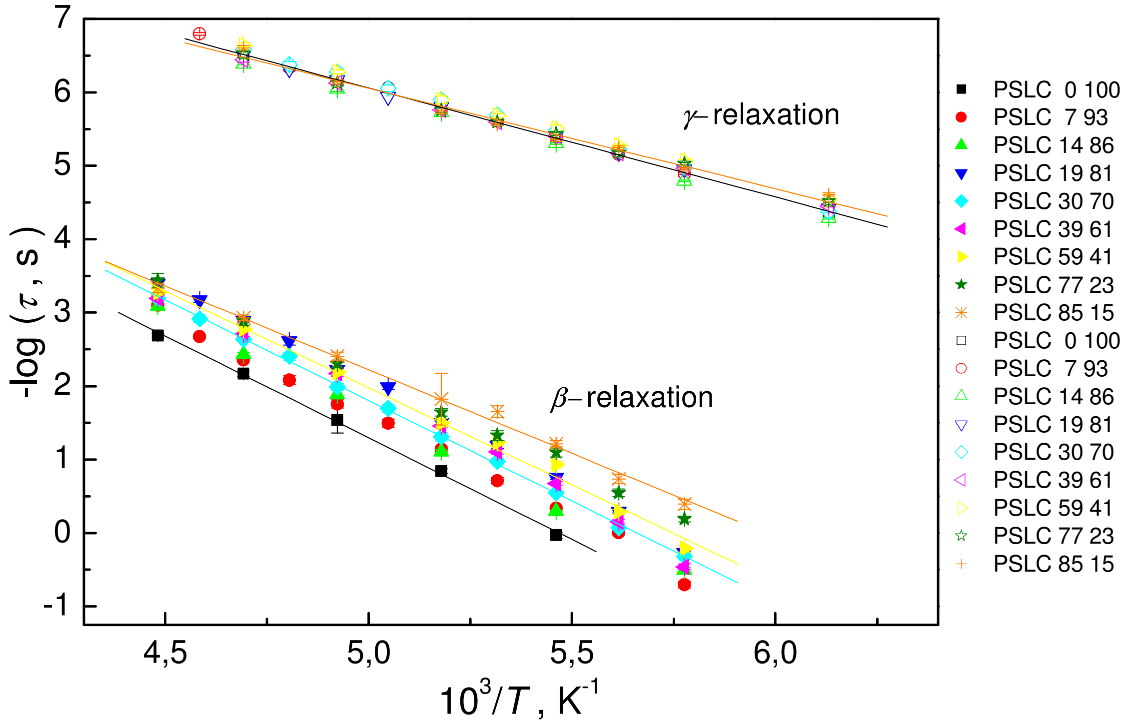

Figure 5.36. The activation diagram for the local relaxation processes (*β* and *γ*) in the copolymers investigated. The errors are smaller than the size of the symbols. The solid lines are the fit of Eq. 5.4 to the data.

The determined parameters for the *β*- and *γ*-processes have typical values of secondary or subglass relaxations. They reflect the reorientation of relatively small portions of the macromolecule [136].

Figure 5.37 shows the very general case of the SCLC polymer. By varying the groups B, X, Y and Z, one can insert various dipole moments and observe different local dielectric relaxations. It is useful to regard the origin and the characteristic features of several local relaxation processes, described in literature and compare them with those observed in the PSLC block copolymers examined in this work.

The microscopic origin of the *γ*- relaxation is the local motion of the alkyl spacer. This relaxation is observed in many side-chain LC polymers [74, 115, 117, 131] and some authors denote it as γ_1–relaxation [115, 131]. The methylene spacer itself is nonpolar, but its motion could be dielectrically active because of the adjacent polar groups [131, 137]. According to literature, *γ*-relaxation should be independent on the terminal substituent or the nature of the main chain [131]. Generally, the spacer length does not strongly influence the parameters of *γ*-relaxation, but in side-chain LC polymer with spacer, consisting of two methylene groups, this process is not observed [115, 131]. The spacer in the here presented

LC block consists of four methylene groups, so the observation of γ-relaxation could be expected. The obtained from Figure 5.36 activation energy $E_{a\gamma}$ is about 30 kJ/mol, which is consistent with literature. G. Simon gives in his review article about DS of side-chain LC polymers $E_{a\gamma}$ values between 26 and 40 kJ/mol [131]. The relaxation time τ_γ lies in the interval $(2.3-1.5)\times10^{-4}$ s (at -120°C). The shape parameter α obtained by the Havriliak-Negami fits has values in the range 0.25-0.27, which is typical for a secondary relaxation.

Some SCLC polymers show an additional relaxation process at high frequency, called γ_2- relaxation [115, 131], which is not observed in the DS spectra of the PSLC, investigated in this thesis. It corresponds to the rotation of the end group Z (Figure 5.37). It is observed only for SCLC polymers with *n*-butoxy end group ($O(CH_2)_3CH_3$), but not with CN or OCH_3. According to the theory of low molecular LC dynamics, the dipole moments parallel to the long molecular axis cannot take place in rotational motion about this axis (Figure 4.13). The dipole moment of the CN end group in the PSLC samples, regarded in this dissertation, is parallel to the long axis. Therefore, the lack of γ_2-relaxation coincides with the theory predictions.

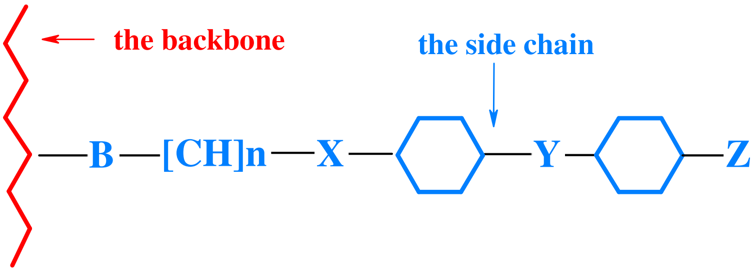

Figure 5.37. An example of a SCLC polymer where the red curve is the polymer backbone.

The β-relaxation corresponds to the rotation of the mesogenic side-group around its long axis. This process has been detected in the glassy state for many side-chain LC polymers [86, 115, 117, 138, 139]. This was also observed in the carbosilane dendrimers with cyanobiphenyl end groups attached to the dendrimer via alkyl spacers [135]. It should also be observed in the frequency interval 10^7–10^9 Hz in the isotropic and the LC phases. Some authors ascribe the β-process to the internal motion of the central ester moiety residing between the aromatic groups (Figure 5.37– in this case the substituent Y is a COO group) [115, 131]. In our case, the two phenyl rings are connected directly; therefore this explanation is not possible. The end nitrile group has very high dipole moment (4.2 D) [140], but as it was already mentioned, it is coaxial to the long axis; hence it can not contribute to the rotational motion (Figure 4.13). The carbonyl group between the cyanobiphenyl mesogen and the spacer has a component of the dipole moment directed normal to the long axis of the mesogenic group. Consequently, the rotation of the mesogen could be related to the transverse component of the carbonyl group dipole moment.

The activation energy $E_{a\beta}$ of the β-process was found to be 53 kJ/mol. This is consistent with the data, collected by Kremer and Schönhals. They give values for $E_{a\beta}$ between 46.5 and 68.9 kJ/mol [86]. The mesogens in their polymers are slightly different, but the principle of motion should be the same. They found that with increasing of the spacer length, $E_{a\beta}$ increases, because of the improved order in the smectic phase. In addition, the parameter $f_\infty \sim 1/\tau_0$ (Eq. 5.4) increases with decreasing the mean lateral distance between the mesogens [86]. Therefore the β-relaxation of a single mesogen depends to some extend on the environment, i.e. it is partially correlated with the dynamics of the surrounding molecules. The relatively bulky phenyl rings can not move independently, because of the steric interactions with the nearest mesogens. Hence, the nature of the β-process is not "purely local" as that of the γ-relaxation. It may be regarded to some extend as a cooperative one. This conclusion is consistent with the results, obtained in this thesis, as we will see in the next section of this chapter.

The effect of the nanoscale confinement on the β- and γ- dynamics

Figure 5.38, Figure 5.39 and Figure 5.40 show the variation of the relaxation time τ, activation energy E_a and the shape parameter $m=n=\alpha_k$ for different morphologies, i.e. for various spatial constrains. The LC block is consequently passing from the unconfined state (LC homopolymer and LC matrix) to the 1D (lamellae), 2D (cylinders) spatial constrains upon moving from left to right. Let us consider the γ-relaxation first. It is clearly seen from Figure 5.38, Figure 5.39 and Figure 5.40 that the relaxation time, the activation energy and the shape parameter do not vary with decreasing the domain dimensions. Hence, the confinement does not have any effect on the local spacer motion.

However, this is not the case for the β-relaxation. As we have already seen, the libration of the mesogen is a partially cooperative process. Hence, one could expect some influence of the constraint on the relaxation parameters. It follows from Figure 5.38 and Figure 5.39 that the relaxation time and the activation energy for β-transition decrease for a confinement length less than 21 nm, whereas the shape parameter $m=n$ (Figure 5.40) do not vary within the experimental error. The overall change in the relaxation time is about a half order of magnitude, which is considerably less than observed for essentially cooperative α- and δ- processes.

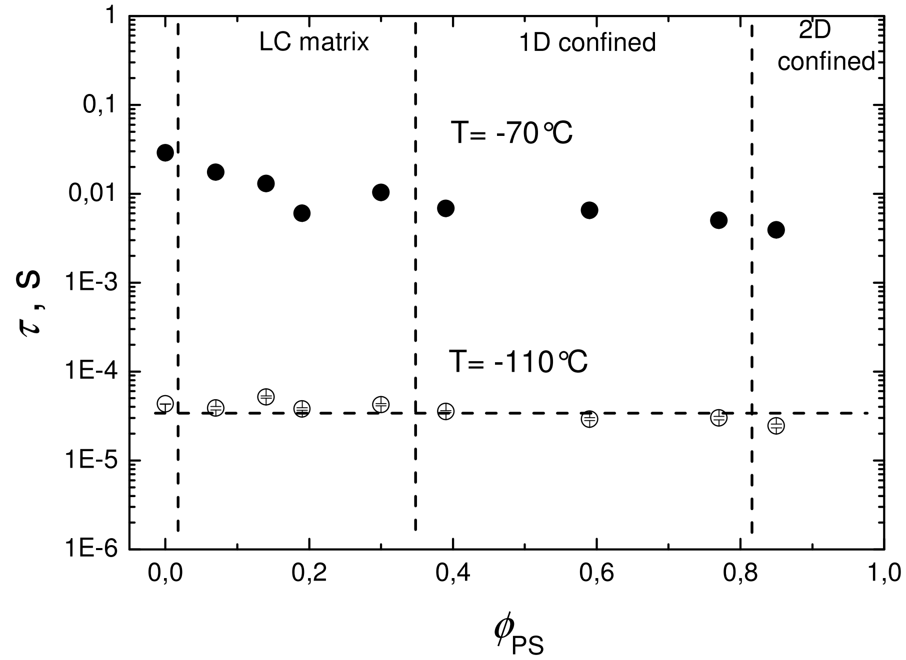

Figure 5.38. The relaxation time τ for the β (•) and γ(o) processes of LC block as a function of PS volume fraction. The vertical dashed lines separate approximately the different mesophase structures.

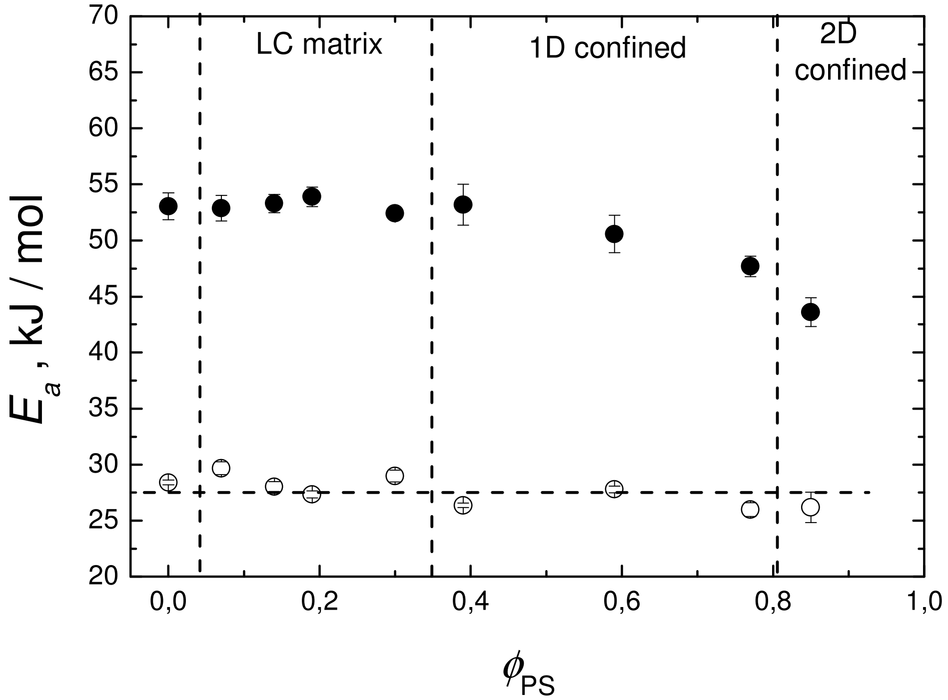

Figure 5.39. The activation energy E_a for the β (•) and γ(o) processes of LC block as a function of PS volume fraction. The vertical dashed lines separate approximately the different mesophase structures.

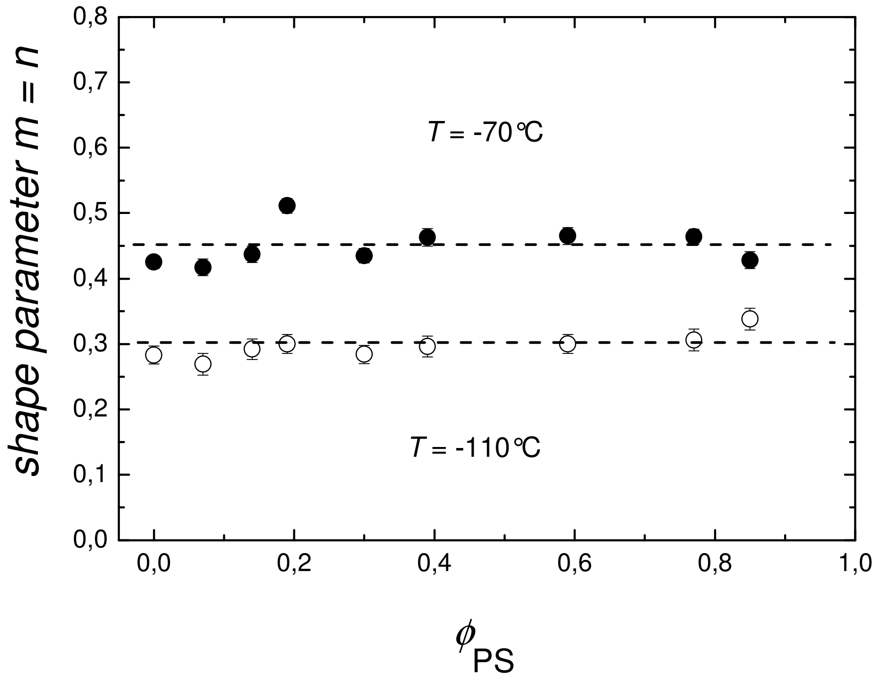

Figure 5.40. The shape parameter $m=n$ for the β (•) and γ(o) processes of LC block as a function of PS volume fraction. The vertical dashed lines separate approximately the different mesophase structures.

Another criterion for ascribing of certain relaxation process as local or cooperative is the value of its activation entropy ΔS. The Eq. 5.4 can be expressed in frequency terms as:

$$f = f_\infty \exp(-E_a / RT), \tag{5.5}$$

where f_∞ is a preexponential factor and R is the gas constant.

An alternative expression derived from the theory of absolute reaction rates, is given by Eyring's activated states equation [136, 141]:

$$f = \frac{1}{2\pi\tau} = \frac{kT}{2\pi h}\exp(-\frac{\Delta H}{RT})\exp(\frac{\Delta S}{R}) \tag{5.6}$$

where k is the Bolzmann constant h– Plank constant, ΔH – the activation enthalpy and ΔS – the activation entropy. T and f are given in Kelvin and Hz respectively. Taking the *ln* from both sides in equation 5.6, one obtains about the activation enthalpy the following expression:

$$\Delta H = T\Delta S - RT\ln\frac{2\pi hf}{kT} \tag{5.7}$$

The activation energy is related to the activation enthalpy by the equation

$$E_a = \Delta H + RT\,. \tag{5.8}$$

Using Eq. 5.7 and 5.8, one can calculate the activation energy at temperature T:

$$E_a = \Delta H + RT = RT\,(1 + \ln\frac{kT}{2\pi h f}) + T\Delta S \tag{5.9}$$

It has been found that for many relaxations, particularly those, involving small, submolecular fragments, moving independently of each other, the activation entropy ΔS is close to zero [136, 141]. If *T'* is the temperature in Kelvin at which the frequency of the relaxation is 1 Hz and ΔS ~0, E_a follows a simple, almost linear dependence on temperature:

$$E_a = RT'(1 + \ln\frac{k}{2\pi h} + \ln T') = RT'(22{,}92 + \ln T') \tag{5.10}$$

Eq. 5.10 defines an effective lower limit for the activation energy. The extend to which E_a exceeds this value is equal to $T'\Delta S$. For essentially cooperative relaxations, such as the dynamic glass transition, it was proven that the data deviate significantly from the zero entropy prediction [136]. This means, that if one process is local, its activation energy E_a has to lie on the line defined by the Eq. 5.10 (the black line in Figure 5.41). With increasing the cooperativity, the activation entropy ΔS increases and the deviation of E_a from this line increases.

The values of E_a vs. *T'* for *β*- and *γ*- processes for all PSLC block copolymer are presented in Figure 5.41. The solid black line was calculated according to Eq. 5.10. The red dashed line and the blue dotted line were calculated according to the Eq. 5.9 using activation entropy values correspondingly ΔS=0,02 kJ / (mol.K) and ΔS=0,04 kJ / (mol.K).

One can see from Figure 5.41 that the *γ*-relaxation is close to the theoretical line, which defines an effective lower limit for the activation energies for non cooperative motions. The activation entropy ΔS_γ for all polymers is less than 0.02 kJ / (mol.K). The *β*-process is above the line with zero entropy providing the more cooperative nature of that motion compared to the *γ*- process. The activation entropy ΔS_β for most of the samples is around 0.04 kJ / (mol.K) or even above this value. It decreases slightly for the sample PSLC 77/23 (1D-confinement with length 11 nm) and more pronounced for the sample PSLC 85/15 (2D-confinement with diameter 13 nm). The value of ΔS_β for sample PSLC 85/15 is smaller than 0.02 kJ / (mol.K). It is similar to ΔS_γ for all PSLC copolymers. The reduction of ΔS_β can be explained by loosing of cooperativity induced by confinement. It means that the kinetic units move more independently from each other in the confinement state in comparison with bulk state.

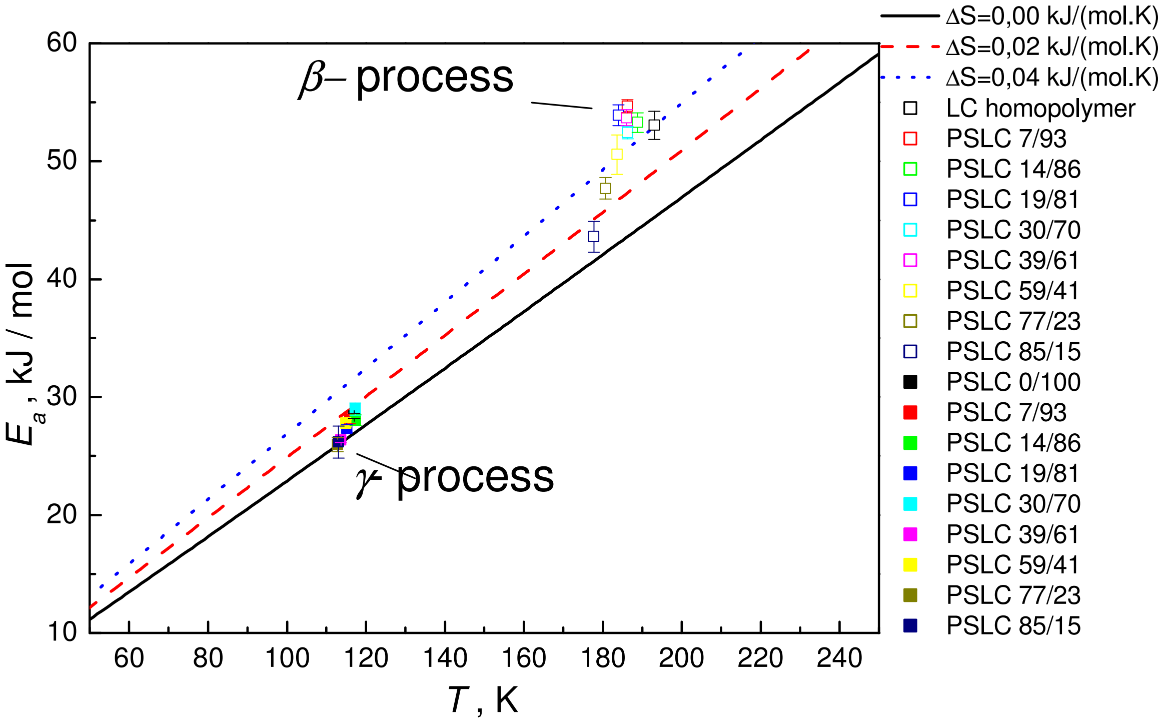

Figure 5.41. The activation energy E_a of *β*- process (open squares) and *γ*- process (full squares) vs T'.

In addition, as we have seen above, the temperature dependence of the relaxation time is different for the cooperative and non-cooperative processes. The temperature dependence for the cooperative motion usually follows the Vogel-Fulcher-Tammann low. The non-cooperative processes have Arrhenius-like temperature dependence. The *β*-relaxation of the studied in this work LC block shows Arrhenius type temperature dependence in both confined and non-confined states. According to this criterion the *β*-relaxation behaves as a non-cooperative process. On the other hand, the parameters of the local processes (E_a, τ, n, m) should be not influenced from the spatial confinement. The activation energy $E_{a\beta}$ and the relaxation time τ_β decrease slightly in the confined state. However, the effect was much less pronounced than for the cooperative *α*- and *δ*- relaxations.

Another criterion to distinguish between cooperative and non-cooperative motion is the temperature dependence of the relaxation strength Δ*ε*. In the case of ideal local motion Δ*ε* should not depend on the temperature. Figure 5.42 displays the relaxation strength Δ*ε*, normalized to the volume fraction of the LC block (ϕ_{LC}), vs the reciprocal temperature for both local modes in LC homopolymer and PSLC 85/15. The $\Delta\varepsilon_\beta$ and $\Delta\varepsilon_\gamma$ values are obtained from fits of the isothermal dielectric loss data to the HN equation (Eq 4.47). It is clearly seen in Figure 5.42 that $\Delta\varepsilon_\gamma$ is approximately constant in a broad temperature range. At the same time $\Delta\varepsilon_\beta$ increases with a decrease of temperature and therefore the effective dipole moment increases. This behaviour is characteristic for cooperative type relaxations. Therefore due to these results the γ process may be considered as non-cooperative, whereas β– as cooperative. It should be noted that in Figure 5.42 we do not see any confinement effect on both processes. According to our previous consideration it should be valid for γ-relaxation but not for β- process. This result can be explained with the higher uncertainty in $\Delta\varepsilon / \phi_{LC}$ determination and the rather weak dependence of $\Delta\varepsilon_\beta$ on confinement. In the case of α- relaxation (segmental motion) in PMMA thin films the confinement effect on $\Delta\varepsilon_\alpha$ is more pronounced [142, 143]. The $\Delta\varepsilon_\alpha$ value decreases with decreasing the film thickness, reflecting a loss of cooperativity.

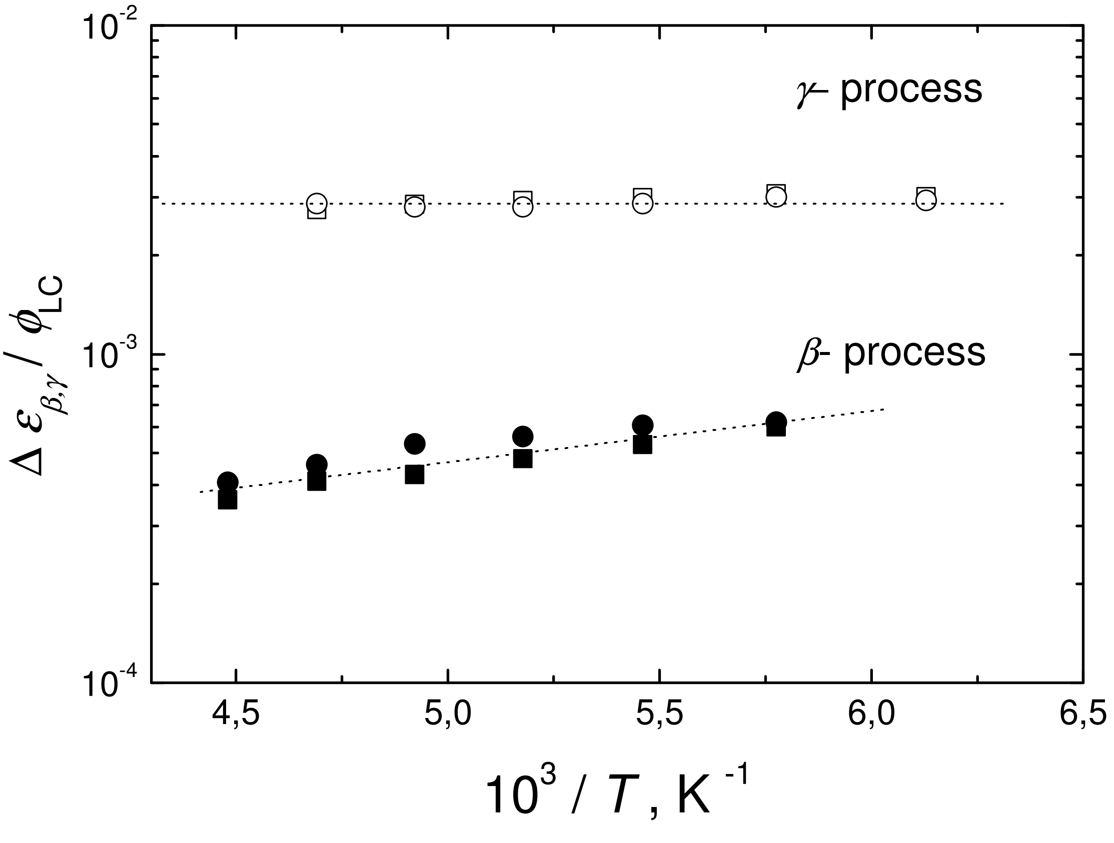

Figure 5.42. Relaxation strength $\Delta\varepsilon$ normalized to the volume fraction of the LC block (ϕ_{LC}) vs reciprocal temperature.

In conclusion, we can say that due to being close to zero entropy, the 'local type' dependence of the relaxation time and relaxation strength on the inverse temperature T and its low $E_{a\gamma}$ value, γ- relaxation is purely a non-cooperative process.

The case for β- relaxation is quite different. The dependence of the relaxation time on the inverse T and the activation energy value Ea_β are typical for local process, whereas the $\Delta\varepsilon_\beta$ (T) already shows cooperative character. Moreover, the activation entropy derived from the plot in Figure 5.41 is higher than that of the *γ*- relaxation. Therefore, the *β*- relaxation is not purely local process. The different character of the both processes can be attributed to different steric interaction of the corresponding part of the molecule with the neighbours. Also, since the bulky mesogen requires more space for its relaxation than the alkyl spacer, it is possibleto include its surrounding in the cooperative motion.

6. Summary and outlook

Block copolymers (BC) are very interesting systems for fundamental studies of the principals of microphase separation, morphology of microphase separated systems and molecular dynamics in a confined geometry. The liquid crystalline / isotropic block (LC/I) copolymers are of special interest due to their structure-within-structure morphologies, i.e. the domain periodicity is combined with the liquid crystalline order within the domains.

The aim of this dissertation is to study the morphology, molecular dynamics and phase transitions of novel side-chain liquid crystal / polystyrene (PSLC) block copolymers with well defined chemical structure and narrow molecular weight distribution by means of small angle X-ray scattering (SAXS), wide angle X-ray diffraction (WAXD), dielectric spectroscopy (DS), polarisation optical microscopy (POM) and differential scanning calorimetry (DSC). The volume fraction of the PS blocks was varied within a broad range (0.07-0.97).

Liquid crystalline order

Measurements using SAXS, WAXD and POM indicate that the liquid crystal phase is nematic. This result is consistent with the expectation for side-chain liquid crystals (SCLC) with a biphenyl mesogen coupled to the main chain by a spacer of four alkyl groups. The mean distance between the mesogens (0.43nm) was obtained by evaluating the WAXD patterns.

The thermotropic behaviour of the liquid crystal (LC) block was probed by DSC and POM. The glass transition was found to be at ~35 °C and the nematic-to-isotropic transition in the range of 112-127 °C. The nematic-to-isotropic transition temperature T_i remains relatively stable with the morphology variation, i.e. does not depend on the domain form. T_i decreases slightly with decreasing of the LC volume fraction.

Domain structure

The domain structure of the microphase separated block copolymers, determined by SAXS, shows no order-to-disorder transition in the range of 25°C-170°C, as is typical for block copolymers in the strong segregation regime. Four types of structures were found –

PS cylinders in LC matrix, alternating lamellae, LC cylinders in PS matrix and LC spheres in PS matrix. The domain dimensions vary between 9 and 26 nm and the lattice constant – between 27 and 47 nm. The phase diagram remained stable in the temperature range of 25 °C - 170 °C, i.e. the morphology of the samples does not change. However, it differs strongly from the phase diagram of isotropic / isotropic (I/I) block copolymers due to the influence of the nematic LC phase. Unlike the phase diagram of I/I block copolymers, the investigated PSLC is strongly asymmetric. The spherical domains embedded within the LC matrix cause distortions in the nematic field. The elastic energy arising from such distortions influence the domain form. Domains with a high interfacial curvature (spheres) are transformed to domains with a low interfacial one (lamellar and hexagonal). The clearing of the nematic field above the nematic-to-isotropic transition temperature T_i is a factor, which may initiate change of the domain form if the sample is near to the border of the phase diagram, i.e. to cause order-to-order transition. In the present study the morphology remains unchanged above T_i, i.e. no order-to-order transition was observed. However, the nematic-to-isotropic transition changed strongly the lattice parameters and domain size of the PSLC 7/93. Evidently, this sample was close to the hexagonal / bcc border of the phase diagram, but still not near enough to undergo an order-to-order transition triggered by the nematic-to-isotropic transition. As mentioned above, the PSLC phase diagram does not get close to the I/I one even above T_i. Hence, there are additional contributing factors to the nematic field, which cause the asymmetry in the phase diagram. One of these factors may be the conformational asymmetry of the samples (the Kuhn length of LC block is bigger than the PS).

In general, the phase diagram of the investigated PSLC block copolymers is in agreement to the theoretical one for planar anchoring calculated by Hammond et al. based on the Wang and Warner theory of nematic SCLC polymers. It is similar as well to the phase diagrams of other liquid crystalline / isotropic (LC/I) block copolymers cited in literature.

Molecular dynamics

The microphase separated PSLC block copolymers were used as an appropriate model system for studying molecular dynamics in confined geometry. The rotational dynamics of the LC block was studied by DS in an unconfined geometry (LC homopolymer and LC matrix) as well under in 1D 2D and 3D confinement (lamellar, cylindrical and spherical domains, correspondingly). The studies were performed over a broad temperature and frequency ranges by means of dielectric spectroscopy.

Four relaxation processes have been detected – two segmental (α- relaxation and δ-relaxation) and two local (β-relaxation and γ-relaxation). The α- relaxation corresponds to the segmental motion of the main chain together with the side chain. The δ-relaxation corresponds to the motion of the side-chain as a whole. The β-relaxation corresponds to the rotation of the biphenyl mesogen around its long axis. The γ-relaxation corresponds to motion of the alkyl spacer in the side-chain of the LC block.

The samples with a confined LC phase show an additional relaxation process at low frequencies, namely the Maxwell-Wagner (MW) polarization. The MW relaxation appears due to the polarization at the interface between the LC and PS block. Here also, the experimental results agree well with the theoretically predicted ones.

The segmental relaxation processes display a non-linear behaviour of the relaxation time τ in Arrhenius coordinates. They are governed by the glass transition of the LC phase. The dynamic glass transition temperature T_{gDIEL} for the both processes is nearly the same.

The local relaxations show a linear behaviour in Arrhenius coordinates. The determined activation energies are typical for sub-glass processes – $E_{a\beta}$ ~ 53 kJ/mol for the β-process and $E_{a\gamma}$ ~ 30 kJ/ mol for the γ-process.

The change of several dielectric parameters with the spatial confinement is regarded- the relaxation time, the shape parameters and the activation energy.

It was found that the relaxation time for δ- and α- relaxation processes decreases significantly when the geometry is restricted. The decrease in τ is more pronounced for the 2D confinement (cylindrical LC domains). The effect is less pronounced for the temperature above T_{i}. These results are in agreement with most reports for thin polymer films. However, the decreasing of the glass transition relaxation time for the latter was explained by the three- layer model, which supposes different mobility for the surface, the bulk and the sample/substrate interface layers. In the case of PSLC, the shape of the dielectric loss curve for the α- relaxation does not change, i.e. the relaxation time distribution remains the same. Therefore applying the three layer model does not seem appropriate here. On the other hand, the δ process broadens with decreasing the domain size. It is apparently governed by a larger characteristic length than this of the α- relaxation.

The dependence of the relaxation time of the β- process on the constraint is similar to that of the α- and δ- relaxations, although the variation is less pronounced. The relaxation time decreases for confinement lengths less than ~20 nm. This dependence shows that the *β*- relaxation is not a pure local process, but has a partially cooperative nature. The dependence of the relaxation time on the inverse temperature in Arrhenius coordinates remains linear for all PSLC block copolymers. This linear dependence is characteristic for local processes. On the other hand, the activation energy decreases with the confinement length and activation entropy is positive, which again is an evidence for a partially cooperative character of the *β*- process. The shape parameters remain constant.

The relaxation time of the *γ*- relaxation is not influenced by the domain shape and dimensions. It shows linear behaviour in Arrhenius coordinates. The activation energy and the shape parameters do not depend on the constraint. The activation entropy is very close to zero. All these results are an evidence for the purely local origin of the *γ*- relaxation.

The influence of the spatial confinement on the relaxation parameters depends on the length scale of the molecular motion. It is more pronounced in the cooperative *α*- and *δ*-relaxation than in the partially cooperative *β*-relaxation. The *γ*- relaxation is independent on the spatial constraint, even for the smallest domain size; hence, it can be regarded as pure local motion.

Outlook

The results of this thesis, while providing information on the morphology, molecular dynamics and phase transitions of novel side-chain liquid crystal / polystyrene (PSLC) block copolymers, also highlight the need of further studies, which address specific issues that were beyond the scope of this work. These are listed below:

- Complementary to the results of this thesis, the morphology and molecular dynamics of oriented samples may be also be studied and compared. The use of oriented samples could provide information about the mesogen anchoring to interface between the domains. The different degrees of ordering – block copolymer domain and nematic order of the mesogen – could be studied separately in oriented samples. Experiments along this line are presently beeing done. The oriented, nanostructured materials will find many applications.
- The morphology and molecular dynamics of thin films of PSLC on various substrates would also be an intesting topic for the future. Especially, the influence of the substrate on the domain order would deliver valuable information. Also, the interaction of

domain confinement with the thin film confinement as well as the influence of the two types of confinement together on the molecular dynamics are topics of great interest.

- It would be valuable to compare the morphology and the dynamics of PSLC diblock copolymers with this in triblock copolymer systems, containing the same LC block in various volume fractions (as it was mentioned in the thesis that interesting data for PS-LC-PS triblock copolymer with PS volume fraction 12% are already published from Sänger *et* al.). It is still an open question, if only the PS-LC-PS triblock copolymer will show an OOT.
- Modification of the chemical structure of the LC block could be conducted to obtain additional physical properties for eventual technological implementation in nanotechnology. For example, one could use different mesogens and arrive at smectic structure

References

1. Hamley, I. W., *Angew. Chem. Int. Ed.* **2003**, *42*, 1692-1712.
2. Hamley, I.W. *Introduction to soft matter*, John Wiley & Sons, LTD, England, **2000.**
3. Hamley, I.W. *The physics of block copolymers*, Oxford University Press, **1998.**
4. Park, C., Yoon, J., Thomas, E. L., *Polymer* **2003,** *44*, 6725-6760.
5. Lodge, T. P., *Macromol. Chem, Phys.* **2003**, *204*, 265-273.
6. Lazzari, M., López-Quintela, M. A., *Adv. Mater.***2003**, *15*, 1583-1594.
7. Spontak, R. J. and Alexandridis, P., *Curr.Opin, in Colloid &Interface Sci.* **1999**, *4*, 140-146.
8. Ruokolainen, J.; Brinke, G. ten; Ikkala, O. *Adv. Mater.*, **1999**, *11*, 777-780.
9. Leibler, L. *Macromolecules*, **1979**, *13*, 6, 1602-1617.
10. Helfand, E. and Wasserman, Z.R., *Macromolecules*, **1976**, *9*, 879-888.
11. Helfand, E. and Wasserman, Z.R. *Microdomain structure and the interface in block copolymers*. In *Developments in block copolymers*, Vol.1, (Ed. I. Goodman), p.99. Applied Science, London.
12. Semenov, A. N., *Soviet Physics JETP*, **1985**, *61*, 733-742.
13. Semenov, A. N, *Macromolecules*, **1989**, *22*, 2849-2851.
14. Matsen, M. W. and Bates, F. S., *Macromolecules*, **1996**, *29*, 1091-1098.
15. Matsen, M. W. and Bates, F. S., *J Polym Sci B: Polym Phys*, **1997**, *35*, 945-952.
16. Matsen, M. W., *J. Phys: Cond Matt*, **2002**, *14*, R21-R47.
17. Matsen, M. W. and Schick, M., *Physical Review Letters*, **1994**, *72*, 2660-2663.
18. Hajduk, D. A., Harper, P. E., Gruner, S. M., Honeker C. C., Kim G., Thomas E. L. *Macromolecules*, **1994**, *27*, 4063-4075.
19. Schulz, M. F., Bates, F. S., Almdal, K., Mortensen, K., *Physical Review Letters*, **1994**, *73*, 86-89.
20. Hamley, I. W.; Koppi, K. A.; Rosedale, J. H.; Bates, F. S.; Almdal, K.; Mortensen, K. *Macromolecules*, **1993**, *26*, 5959-5970.
21. Förster, S., Khandpur, A. K., Zhao, J, Bates, F. S., Hamley, I. W., Ryan A. J., Bras, W. *Macromolecules*, **1994**, *27*, 6922-6935.
22. Khandpur, A. K., Förster, S., Bates, F. S., Hamley, I. W., Ryan, A. J., Bras, W., Almdal, K., Mortensen, K., *Macromolecules*, **1995**, *28*, 8796-8806.
23. Bates, F. S., Schultz, M. F., Khandpur, A.K., Förster, S., Rosedale, J.H., Almdal, K., Mortensen, K., *Faraday Discuss*, **1994**, *98*, 7-18.

24. Hamley, I. W.; Gehlsen, M. D.; Khandpur, A. K.; Koppi, K. A.; Rosedale, J. H.; Schulz, M. F.; Bates, F. S.; Almdal, K.; Mortensen, K. *J.Phys. II France*, **1994**, *4*, 2161-2186.
25. Vavasour, J. D., Whitmore, M. D., *Macromolecules*, **1993**, *26*, 7070-7075.
26. Stühn, B.; Mutter R.; Albrecht, T. *Europhys. Lett.*, **1992**, *18*, 427-432.
27. Heck, B.; Arends, P.; Ganter, M.; Kressler, J.; Stühn, B. *Macromolecules* **1997**, *30*, 4559-4566.
28. Schwab, M.; Stühn, B. *Colloid Polym. Sci.* **1997**, *275*, 341-351.
29. Schwab, M.; Stühn, B. *J. Chem. Phys.* **2000**, *112*, 6461-6471.
30. Schwab, M.; Stühn, B. *Physical Review Letters*, **1996**, *76*, 924-927.
31. Hajduk, D.; Gruner, S. M.; Rangarajan, P.; Register, R.A.; Fetters, L.J.; Honeker, C.; Albalak, R. J.; Thomas, E. L. *Macromolecules* **1994**, *27*, 490-501.
32. Mao, G.; Ober, C. K. *Acta Polymer.* **1997**, *48*, 405-422.
33. Fischer, H.; Poser, S. *Acta Polymer.* **1996**, *47*, 413-428.
34. Zheng, W.Y. and Hammond, P.T., *Macromolecules*, **1998**, *31*, 711-721.
35. Anthamatten M., Hammond P. T. *J. Polymer Sci: Part B: Polym Phys* **2001**, *39*, 2671-2691.
36. Anthamatten M., Hammond P. T. *Macromolecules* **1999**, *32,* 8066-8076.
37. Osuji, C. O.; Chen, J. T.; Mao, G.; Ober, C. K.; Thomas, E. L. *Polymer* **2000**, *41*, 8897-8907.
38. Mao, G.; Wang, J.; Clingman, S. R.; Ober, C. K.; Chen, J. T.; Thomas, E. L. *Macromolecules* **1997**, *30*, 2556-2567.
39. Mao, G., Wang, J., Ober, C., Brehmer, M., O'Rourke, M., Thomas, E., *Chem. Matter.* **1998**, *10*, 1538-1545.
40. Fischer, H.; Poser, S.; Arnold, M. *Liquid Crystals* **1995**, *18*, 503-509.
41. Sänger, J.; Gronski, W.; Maas, S.; Stühn, B.; Heck, B. *Macromolecules* **1997**, *30*, 6783-6787.
42. Schneider, A.; Zanna, J.-J.; Yamada, M.; Finkelmann, H.; Thomann, R. *Macromolecules* **2000**, *33*, 649-651.
43. Schüller, J.; Richert, R.; Fischer, E.W. *Phys. Rev. B* **1995**, *52*, 15232-15238.
44. Gorbatschow, W.; Arndt, M.; Stannarius, R.; Kremer, F. *Europhys. Lett.* **1996**, *35*, 719-724.
45. Huwe, A.; Kremer, F.; Behrens, P.; Schwieger, W. *Phys. Rev. Lett.* **1999**, *82*, 2338-2341.

46. Arndt M.; Stannarius, R.; Groothues, H.; Hempel, E.; Kremer, F.; *Phys. Rev. Lett.* **1997**, *79*, 2077-2080.
47. Pissis, P.; Kyritsis, A.; Daoukaki, D; Barut, G.; Pelster R.; Nimtz, G. *J. Phys.: Condens. Matter* **1998**, *10*, 6205-6227.
48. Daoukaki, D; Barut, G.; Pelster R.; Nimtz, G.; Kyritsis, A.; G. Pissis, P. *Phys. Rev. B* **1998**, *58*, 5336-5345.
49. Kremer, F.; Huwe, A.; Arndt, M.; Behrens, P.; Schwieger, W. *J. Phys.: Condens. Matter* **1999**, *11*, A175-A188.
50. Fukao, K., Miyamoto, Y. *Europhys. Lett.* **1999**, *46*, 649-654.
51. Fukao, K., Miyamoto, Y. *Phys. Rev. E* **2000**, *61*, 1743-1754.
52. Schüller, J.; Melnichenko, Y.B.; Richert, R.; Fischer, E.W. *Phys. Rev. Lett.* **1994**, *73*, 2224-2227.
53. Huwe, A.; Arndt, M.; Kremer, F.; Haggenmüller, C.; Behrens, P. *J. Chem. Phys.* **1997**, *107*, 9699-9701.
54. Petychakis, L.; Floudas, G.; Fleischer, G. *Europhys. Lett.* **1997**, *40*, 685-690.
55. Jeon, S.; Granick, S. *Macromolecules* **2001**, *34*, 8490-8495.
56. Wendt, H.; Richert, R. *J. Phys.: Condens. Matter* **1999**, *11*, A199-A206.
57. Park ,J.-Y.; McKenna, G.B. *Phys. Rev. B* **2000**, *61*, 6667-6676.
58. Keddie, J.L.; Jones, R.A.L.; Cory, R.A. *Europhys. Lett.* **1994**, *27*, 59-64.
59. Forrest, J.A.; Dalnoki-Veress, K.; Stevens, J.R.; Dutcher, J.R. *Phys. Rev. Lett.* **1996**, *77*, 2002-2005.
60. Forrest, J.A.; Dalnoki-Veress, K.; Stevens, J.R.; Dutcher, J.R. *Phys. Rev. E* **1997**, *56*, 5705-5716.
61. Forrest, J.A.; Dalnoki-Veress, K.; Stevens, J.R.; Dutcher, J.R. *Phys. Rev. E* **1998**, *58*, 6109-6114.
62. Mattsson, J.; Forrest, J.A.; Börjesson, L. *Phys. Rev. E* **2000**, *62*, 5187-5200.
63. Tseng, K.C.; Turro, N.J.; Durning, C.J. *Phys. Rev. E* **2000**, *61*, 1800-1811.
64. Grohens, Y.; Sacristan, J.; Hamon, L.; Reinecke, H.; Mijangos, C.; Guenet, J.M. *Polymer* **2001**, *42*, 6419-6423.
65. Kremer. F.; Hartmann, L. *Dielectric Newsletter* September **2001**, 4-6.
66. Floudas, G.; Paraskeva, S.; Hadjichristidis, N.; Fytas, G.; Chu, B.; Semenov, A.N. *J. Chem. Phys.* **1997**, *107*, 5502-5509.
67. Floudas, G.; Hadjichristidis, N.; Iatrou, H.; Pakula, T. *Macromolecules* **1996**, *29*, 3139-3146.

68. Floudas, G.; Meramveliotaki, K.; Hadjichristidis, N. *Macromolecules* **1999**, *32*, 7496-7503.
69. Floudas, G., Antonietti, M., Förster, S., *J. Chem. Phys.*, **2000**, *113*, 3447-3451.
70. Zhukov, S., Geppert, S., Stühn, B., Staneva, R., Ivanova, R., Gronski, W., *Macromolecules* **2002**, *35*, 8521-8530.
71. Zhukov, S., Geppert, S., Stühn, B., Staneva, R., Gronski, W., *Macromolecules* **2003**, *36*, 3635-3645.
72. Tang, B. Z.; Kong, X.; Wan, X.; Peng, H; Lam, W. Y.; Feng, X.-D.; Kwok, H. S. *Macromolecules,* **1998**, *31*, 2419-2432.
73. de Gennes, P.-G., Prost, J. *The physics of Liquid Crystals*, Clarendon Press, Oxford, **1993**.
74. Moscicki, J.K., Dielectric relaxation in macromolecular liquid crystals. In *Liquid crystal polymers - from structures to applications*; Collyer, A. A., Ed.: Elsevier: Amsterdam, The Netherlands, **1992**.
75. de Gennes, P.-G. *Scaling concepts in polymer physics*, Cornell Univ. Press, Ithaca, NY [u.a.], **2004**.
76. de Gennes, P G. *J. Phys.* (*Paris*) **1970**, *31*, 235.
77. Wang, X. J.; Warner, M. *J. Phys. A: Math. Gen.* **1987**, *20*, 713-731.
78. Roe, R.-J.; *Methods of X-Ray and Neutron Scattering in Polymer Science,* Oxford University Press, **2000**.
79. Strobl, G. *The Physics of Polymers*, Springer – Verlag Berlin Heidelberg, **1996** and **1997**.
80. Ivanova, R., Staneva, R., Geppert, S., Heck, B., Walter, B., Gronski, W., Stühn, B., *Colloid Polym. Sci.*, **2004**, *282*, 810-824.
81. Mittelbach, P. and Porod, G., *Acta Physica Austriaca* **1961**, *14*, 405-439.
82. Guinier, A. *X-ray Diffraction*, Freeman, San Francisco, **1963**.
83. Warren, B. E., *X-ray Diffraction*, Dover Publications, **1990**.
84. Strobl, G. *Acta Crystallogr.* **1970**, *A26*, 367-375.
85. Havriliak, S.; Hegami, S. *J. Polym. Sci. Part C* **1966**, *14*, 99.
86. Kremer, F., Schönhals, A., *Broadband Dielectric Spectroscopy*; Springer Verlag: Berlin, **2003**.
87. Rose, M. E., *Elementary Theory of Angular Momentum.* Willey, New York, **1957**.
88. Kyritsis, A.; Pissis, P., Mai, S.-M.; Booth, C. *Macromolecules* **2000**, *33*, 4581-4595.
89. Hedvig, P., *Dielectric Spectroscopy of Polymers*, Academiai Kiado, Budapest, **1977**.

90. Van Beek, L.K.H. Dielectric behaviour of heterogeneous systems. In *Progress in Dielectrics*; Birks, J.B. Ed.: Heywood, London, **1967**, *7*, pp. 69-114.
91. Britta Trahasch, *Thesis*, **December 1997**, Albert-Ludwigs-Universität, Freiburg in Breisgau.
92. Franz Stickel, *Thesis*, **December 1991**, Albert-Ludwigs-Universität, Freiburg in Breisgau.
93. Böttcher, C. J. F. and Bordewijk, P., *Theory of Electric Polarization, Vol II*, Elsevier Scientific Publishing Company, Amsterdam, **1978**.
94. Sänger, J.; Gronski, W. *Macromol. Chem. Phys.* **1998**, *199*, 555-561.
95. Dierking, I.; *Textures of Liquid Crystals*, Wiley-VCH Verlag, Weinheim, **2003**.
96. Schnurpfeil, G., Harder, A., Schröder, H., Wöhrle, D., Hartwig, A., Hennemann, O.-D., *Macromol. Chem. Phys.* **2001**, *202*, 180-187.
97. Sawyer, L. C. and Grubb, D. T. *Polymer Microscopy*, Chapman&Hall, London, **1996**, p. 275-280.
98. Maughon, B. R.; Weck, M; Mohr, B.; Grubbs, R. H. *Macromolecules* **1997**, *30*, 257-265.
99. Yamada, M.; Iguchi, T.; Hirao, A.; Nakahama, S.; Watanabe, J. *Macromolecules* **1995**, *28*, 50-58.
100. Shibaev, V.P.; Konstromin, S. G.; Plate, N. A., *Eur.Polym. J.* **1982** *18*, 651-659.
101. Dubois, J.C.; Decobert, G.; LeBarny, P.; Essenin, S.; Friedrich, C.; Nöel, C, *Mol. Cryst. Liq. Cryst.* **1986**, *137*, 349.
102. Zaschke, B.; Frank, W.; Fisher, H.; Arnold, M. *Polym. Bull.* **1991**, *27*, 1-8.
103. Bohnert, R.; Finkelmann, H; *Macromol. Chem. Phys.* 1994, 195, 689-700.
104. Yamada, M.; Itoh, T.; Nakagawa, R.; Hirao, A.; Nakahama, S.; Watanabe, J. *Macromolecules*, **1999**, *32*, 282-289.
105. Laus, M; Bignozzi, M. C.; Fagnani, M.; Angeloni, A. S.; *Macromolecules* **1996**, *29*, 5111-5118.
106. Mitchell, G.R. and Windle, A.H.; *Polymer*, **1984**, *25,* 906-920.
107. Yamaoka, K.; Kaneko, T.; Gong, J. P.; Osada, Y. *Macromolecules* **2001**, *34*, 1470-1476.
108. Kaneko, T.; Yamaoka, K.; Gong, J. P.; Osada, Y. *Macromolecules* **2000**, *33*, 4422-4426.
109. Almdal, K.; Rosedale, J. H.; Bates, F. S.; Wignall, G. D.; Fredrickson, G. H. *Phys. Rev. Lett.* **1990**, *65,* 1112-1115.

110. Hadziioannou, G., Skoulios, A., *Macromolecules*, **1982**, *15*, 258-262.
111. Terentjev, E. M. *Phys. Rew. E* **1995**, *51*, 1330-1337.
112. Anthamatten, M.; Zheng. W. Y.; Hammond, P. T.; *Macromolecules*, **1999**, *32*, 4838-4848.
113. Fischer,H.; Poser,S.; Arnold,M., Frank, W., *Macromolecules* **1994**, *27*, 7133-7138.
114. Perrier, G.; Bergeret, A.; *J. Appl. Phys.* **1995**, *77*, 2651-2658.
115. Zentel, R.; Strobl, G.; Ringsdorf, H. . *Macromolecules* **1985**, *18*, 960.
116. Schönhals, A.., *Dielectric properties of amorphous polymers*. In: Runt, J.P., Fitzgerald, J.J. (eds) *Dielectric spectroscopy of polymeric materials*. ACS-Books, Washington, DC, **1997.**
117. Gedde, U.W.; Liu, F.; Hult, A.; Sahlen, F.; Boyd, H. *Polymer* **1994**, *35*, 2056-2062.
118. Haase, W.; Bormuth, F.J.; Pfeiffer, M.; Jakob, E. *Ber. Bunsenges. Phys. Chem.* **1991**, *95*, 1050-1054.
119. Attard, G.; Williams, G. *Liq. Cryst.* **1986**, *1*, 253-269.
120. Baehr, C., Glüsen, B., Wendorff, J. H., *Macromol. Chem. Rapid. Commun.*, **1994**, *15*, 327-333.
121. Mano, F.J.; Correia, N.T.; Ramos, J.M. *Polymer* **1994**, *35*, 3561-3564.
122. Mano, F.J.; Ramos, J.M.; Fernandes, A.; Williams, G. *Polymer* **1994**, *35*, 5170-5178.
123. Mano, F.J.; Correia, N.T.; Williams, G. *Liq. Cryst.* **1996**, *20*, 201-218.
124. Zhukov, S.; Stühn, B.; Borisova, T.; Barmatov, E.; Barmatova, M.; Shibaev, V.; Kremer, F.; Pissis, P. *Macromolecules* **2001**, *34*, 3615-3625.
125. Schönhals, A.; Wolff, D.; Springer. J. *Macromolecules* **1998**, *31*, 9019-9025.
126. Yao, M.-L.; Wanatabe, H., Adachi, K.; Kotaka, T. *Macromolecules* **1991**, *24*, 2955-2962.
127. Stühn, B.; Stickel, F. *Macromolecules* **1992**, *25*, 5306-5312.
128. DeMaggio, G.B.; Frieze, W.E.; Gidley, D.W.; Zhu, M.; Hristov, H.A.; Yee, A.F. *Phys. Rev. Lett.* **1997**, *78*, 1524-1527.
129. Schönhals, A.; Schlosser, E. *Colloid Polym. Sci.* **1989**, *267*, 125-132.
130. Schiener, B.; Böhmer, B.; Loidl, A.; Chamberlin, R.V. *Science* **1996**, *274*, 752-754.
131. Simon G. P., *Dielectric properties of polymeric liquid crystals*. In: Runt, J.P., Fitzgerald, J.J. (eds) *Dielectric spectroscopy of polymeric materials*. ACS-Books, Washington, DC, **1997.**
132. Forrest, J.A.; Svanberg, C.; Revesz, K.; Rodahl, M.; Torell, L.M.; Kasemo, B. *Phys. Rev. E* **1998**, *58*, R1226-R1229.

133. Novotna, E.; Kostromin. S.; Kresse, H. *Liq. Cryst.* **1995**, *18*, 73-80.

134. Zhong, Z., Schuele, D., Gordon, W. *Liq. Cryst.*, **1994**, *17*, 199-209.

135. Trahasch, B.; Frey, H.; Lorenz, K.; Stühn, B. *Colloid Polym. Sci.* **1999**, *277*, 1186-1192.

136. Starkweather, Jr., H. W. *Macromolecules*, **1988**, *21*, 1798-1802.

137. Wetton, R. E., Williams, G. *Trans. Faraday Soc.*, **1965**, *61*, 2132-2139.

138. Schönhals, A., Wolff, D., Springer, J. *Macromolecules*, **1995**, *28*, 6254-6257.

139. Schönfeld, A., Kremer, F., Hofmann, A., Kühnpast, K., Springer, J., Scherowsky, G. *Makromol. Chem.* **1993**, *194*, 1149-1155.

140. Klinbiel, R.T., Genova, D. J., Criswell, T. L., Meter, J. P. *J. Am. Chem. Soc.*, **1974**, 7651-7655.

141. Starkweather, Jr., H. W. *Polymer*, **1991**, *32*, 2443-2448.

142. Fukao, K., Uno, S., Miyamoto, Y., Hoshino, A., Miyaji, H., *Phys. Rev. E*, **2001**, *64*, 051807-(1-11).

143. Hartmann, L., Gorbatschow, W., Hauwede, J., Kremer, F. *Eur. Phys. J. E*, **2002**, *8*, 145-154.

Glossary

1(2,3)D	one (two, three) dimensional
DS	Dielectric Spectroscopy
DSC	Differential Scanning Calorimetry
I/I diblock copolymer	isotropic / isotropic diblock copolymer
LC	liquid crystal
LC/I diblock copolymer	liquid crystal / isotropic diblock copolymer
MW	Maxwell-Wagner polarization
ODT	order-to-disorder transition
OOT	order-to-order transition
POM	Polarized Optical Microscopy
PSLC block copolymers	polystyrene- block- side-chain LC block copolymers
RPA	random-phase approximation
SAXS	Small Angle X-ray Scattering
SCLC	side chain liquid crystal
SCMFT	the self consistent mean field theory
WAXD	Wide Angle X-ray Diffraction

Erklärung

Hiermit erkläre ich, dass ich die vorliegende Arbeit selbstständig und nur unter Verwendung der angegebenen Literatur und Hilfsmittel angefertigt habe.

Ein Teil der hier präsentierten Daten wurde in folgenden Artikeln veröffentlicht:

- Zhukov, S., Geppert, S., Stühn, B., Staneva, R., Ivanova, R., Gronski, W., *Macromolecules* **2002**, *35*, 8521-8530.
- Zhukov, S., Geppert, S., Stühn, B., Staneva, R., Gronski, W., *Macromolecules* **2003**, *36*, 3635-3645.
- Ivanova, R., Staneva, R., Geppert, S., Heck, B., Walter, B., Gronski, W., Stühn, B., *Colloid Polym. Sci.*, **2004**, *282*, 810-824.
- B. Stühn, S. Joukov, R. Staneva, R. Ivanova, W.Gronski, S. Geppert, *Chin. J. Polym. Sci.***, 2003,** *21***,** 153-158.

Ilmenau, den 20. Juni 2006

Acknowledgements

First of all, I would like to thank my supervisor Prof. Dr. Bernd Stühn for supervising my dissertation. I greatly appreciate his solid support, scientific guidance, inspiration and motivation. I am especially grateful to him for continuing his strong support after moving from TU Ilmenau to TU Darmstadt.

I thank PD Dr. Paul Denner for accepting official supervision of my dissertation after Prof. Dr. Stühn moved to the TU Darmstadt. I also thank him and Prof. Dr. Jürgen A. Schäfer for their encouragement and support, in particular for providing me a position and the opportunity of working on an interesting project, which also gave me the possibility to complete my dissertation.

Throughout the period of working on my dissertation I have had the pleasure of coming into contact and working with many interesting colleagues and friends who have helped, inspired and encouraged me. Without them my work would have been so much more difficult. First and foremost, I would like to express my acknowledgement to my colleague and friend, Dr. Rouja Ivanova for introducing me into the world of small angle scattering and for the very helpful discussions right from our first meeting. She has been an invaluable source of help during the preparation and writing of this dissertation. I also thank Dr. Sergei Zhukov for sharing with me his expertise and insights in dielectric spectroscopy and for many useful discussions. I am grateful to Dr. Bernd Walter and Dr. Lutz Deutschbein for performing the NMR measurements and Dipl.-Lehrerin Brigitte Seidler for carrying out the DSC measurements. I thank Dr. Ahmed Sayeed for his part in reviewing my dissertation. It was a pleasure to have worked with M.Sc. Sofiya Raleva, Dipl.-Ing. Rainer Sattler and Silke Syptroth as well as all the other colleagues from the Institut für Physik at the TU Ilmenau. The help and assistance of colleagues from the University of Freiburg: Dipl. Chem. Steffen Geppert, Prof. Dr. Wolfram Gronski and Barbara Heck are gratefully acknowledged for the synthesis and the basic characterisation of the PSLC polymers.

Special thanks go to my colleague Dr. Imad Ahmed for critically reviewing this dissertation and for making useful comments. I thank Dr. Rolf Öttking for his help with the formalities of submitting this dissertation.

Many thanks to Prof. Dr. Roland Resel, who gave me the possibility to work in TU Graz and for providing me financial support through the EUROFET-Project. I am especially grateful to him for his interest in seeing me complete my dissertation although it was not the central part of my duties at the TU Graz.

Financial support provided by the German Science Foundation (Deutsche Forschungs Gemeinschaft – DFG) in form of a research position and a stipend from the Gleichstellungsrat at the TU Ilmenau is greatly acknowledged.

Very special thanks go to my parents, who supported me throughout my whole life, loved me more than themselves and believed in me, even during very hard moments. I also thank my friend Stephan for the love and support, which he gave me and the useful discussions on my thesis.

I thank the rest of my family, my aunts Nadejda and Stoyanka, my cousins Margarita, Georgi, Denitza, Krasimir and Marta, and my best friends Lyubov, Lilia, Denka, Christina, Gloria and Petar, Penka and Robert, Donka, Iskra, Petia and Jorg, Carsten, Daniele, Ruska, Svetla and Konstantin for their help, for their psychological support and the nice moments, which we have shared.

I also want to thank my school physics teacher Ruska Dragneva. She opened my eyes into the world of physics and deeply inspired me. She was not only one of the best physics teachers I have ever had, but also a very strong person. She continued her teaching work until her death at the age of 84. Additonally, she was also a friend to us, always ready to help and to motivate. I also thank my cousin, Dobrin Bossev, who helped me during my student years.

And last but not least, my acknowledgements go to Mr Vaklush Tolev, for his inspiring ideas that I came to learn about during the course of his lectures on History and the Theory of Religions, which I attended since my third year at the University. He gave me a new way of thinking and provided me with a new knowledge about God and mankind.